Ferroic Materials: Synthesis, Structure and Properties

A Thesis

Submitted for the Degree of

DOCTOR OF PHILOSOPHY

by

R. VENGADESH KUMARA MANGALAM

CHEMISTRY AND PHYSICS OF MATERIALS UNIT
JAWAHARLAL NEHRU CENTRE FOR ADVANCED SCIENTIFIC RESEARCH
(A Deemed University)
Bangalore – 560 064

JULY 2009

DECLARATION

I hereby declare that the matter embodied in the thesis entitled "**Ferroic Materials: Synthesis, Structure and Properties**" is the result of investigations carried out by me at the Chemistry and Physics of Materials Unit, Jawaharlal Nehru Centre for Advanced Scientific Research, Bangalore, India under the supervision of Prof. A. Sundaresan and it has not been submitted elsewhere for the award of any degree or diploma.

In keeping with the general practice in reporting scientific observations, due acknowledgment has been made whenever the work described is based on the findings of other investigators.

R. Vengadesh Kumara Mangalam

CERTIFICATE

I hereby certify that the matter embodied in this thesis entitled "**Ferroic Materials: Synthesis, Structure and Properties**" has been carried out by Mr. R. Vengadesh Kumara Mangalam at the Chemistry and Physics of Materials Unit, Jawaharlal Nehru Centre for Advanced Scientific Research, Bangalore, India under my supervision and it has not been submitted elsewhere for the award of any degree or diploma.

Prof. A. Sundaresan
(Research Supervisor)

Acknowledgments

First and foremost I should thank Prof. A. Sundaresan for introducing me to the area of solid state chemistry. His patience and guidance throughout the last four years made me to reach this current position. The time he has spend during initial stage of my research and also during the setting up of the lab are some of the best moments of my academic career. I take this opportunity to once again thank him for all his help and guidance throughout my academic career.

I am extremely thankful to Prof. C. N. R. Rao, FRS for his valuable suggestions and discussions during my research work. He has been a constant source of inspiration for me. I greatly admire his enthusiasm towards science.

I thank the past and present chairmen of CPMU, Prof. C. N. R. Rao, FRS and Prof. G. U. Kulkarni, for providing me the various facilities to carry out my research work.

I thank, Dr. Y. Tanaka and Dr. A. Iyo (AIST) for high pressure synthesis, Dr. E. Suard (ILL) for neutron data, Prof. C. Narayana and G. K. Pradhan for IR analysis and high pressure studies, Prof. U. Waghmare and Nirath Ray for theoretical calculations, Prof. B. Raveau and Dr. S. Malo (CRISMAT) for electron diffraction analysis, Prof. J. Gopalakrishnan, Rohini mani and Tiwari (IISc) for thermogravimetric analysis, Prof. S. B. Kirupanidhi and Dr. R. Ranjith (IISc) for early help in ferroelectric measurements, Prof. T. N. Guru Row and Dr. Shivaku-

mara (IISc) for early help in collecting x-ray diffraction data, Dr. A. Govindaraj for helping me in using furnace facility and high vacuum synthesis, Dr. D. Sanyal, Dr. A. Chakrabati and M. Chakrabrati (VECC) for positron annihilation studies and V. P. Bhat for Raman analysis. I thank Prof. G. U. Kulkarni, Vijaykumar, Radha and Bhuvana for training me in atomic force microscopy especially for doing EFM studies.

I am thankful to AIST, Tsukuba, Japan for providing the facilities to do high pressure and high temperature synthesis and for the financial support. I also thank Dr. D. Shivagan, Dr. P. Shiragae and their family for their hospitality during my stay in Tsukuba.

I thank all my course teachers in JNCASR, IISc and The American college, Madurai. I also thank JNCASR staff for various help. I am extremely thankful to JNCASR for providing good facilities.

A special note of thanks is due to Dr. Angappane, Dr. Thirumurugan and Dr. Asish Kundu for their constant help and kindness. I thank past and present labmates, Yasar, Shipra, Madhu and Pranab for their cooperation and for maintaining a cheery atmosphere in the lab. I thank all my friends and family for their support.

It has been a steep learning curve for me in the last four years. I should be thankful and grateful to many people who have contributed to my growth and helped me in one or the other way. So I take this opportunity to thank them all.

Preface

This thesis presents the synthesis and investigation of structure and physical properties of ferroic materials. Ferroic materials encompass ferromagnets, ferroelectrics, ferroelastics and multiferroics. This thesis work is focused on search for materials which may have ferromagnetism/ferroelectricity or multiferroicity and to understand structure - property relationship.

Chapter 1 gives an overview of ferroic and multiferroic materials.

Chapter 2 describes the experimental details involved in the synthesis of the compounds under study and their structural analysis and physical property measurements.

Chapter 3 deals with the structural and dielectric studies on $Bi(Al/Ga)O_3$ synthesized at high pressures and high temperatures. $BiAlO_3$, a new lead free ferroelectric, shows ferroelectric polarization of 16 $\mu C/cm^2$. Contrary to theoretical prediction, $BiGaO_3$ is not a ferroelectric in agreement with its centrosymmetric structure.

In Chapter 4, the effects of oxygen non-stoichiomety in $BiMnO_{3-\delta}$ is discussed. The near stoichiometry phase is shown to form a new phase with lattice parameters, $\sqrt{2}a_p \times 2a_p \times \sqrt{2}a_p$, rather than the monoclinic phase reported in the literature. However, the phase formed with more oxygen deficiency is similar to that reported in the literature.

Chapter 5 details the multiferroic properties observed in nanocrystalline BaTi

O_3. Nanocrystalline $BaTiO_3$ shows ferromagnetism due to defects on the surface of the particles. Further, the hitherto system shows large magnetodielectric effect near room temperature. For comparison, the results obtained for bulk $BaTiO_3$ are also discussed. Positron annihilation spectroscopic studies on these nanoparticles reveal that the defects are oxygen vacancy which is responsible for the observed magnetism.

Chapter 6 reports the structural and dielectric properties of ordered perovskites, $Ba_{2-x}Sr_xBiSbO_6$ ($0 \leq x \leq 2$) and $BaBi_{0.7}Nb_{0.3}O_3$. Structural analyzes were carried out using neutron diffraction data. These systems are interesting because of the presence of Bi:6s lone pair and their semiconducting nature.

Chapter 7 presents the investigations carried out on the three different ferromagnetic perovskite oxides, manganate, Cobaltate and Ruthenate. This chapter deals with preparation, structure, magnetic and other physical properties of these oxides.

Publications

1. Structural, magnetic and magnetotransport properties of $La_{0.7-x}Ce_xBa_{0.3}MnO_3$ ($x = 0.0$ - 0.4), **R. V. K. Mangalam** and A. Sundaresan, *J. Chem. Sci.*, **118**, 99 (2006).

2. Ferroelectricity in ordered perovskite $BaBi^{3+}_{0.5}Bi^{5+}_{0.2}Nb^{5+}_{0.3}O_3$ with Bi^{3+}:$6s^2$ lone pair at the B-site, **R. V. K. Mangalam**, P. Mandal, E. Suard and A. Sundaresan, *Chem. Mater.*, **19**, 4114 (2007).

3. Spin state transition in the ferromagnet $Sr_{0.9}Ce_{0.1}CoO_{2.85}$, **R. V. K. Mangalam**, G. K. Pradhan, Chandrabhas Narayana and A. Sundaresan, *Solid State Commun.*, **146**, 110 (2008).

4. Crucial role of oxygen stoichiometry in determining the structure and properties of $BiMnO_3$, A. Sundaresan, **R. V. K. Mangalam**, A. Iyo, Y. Tanaka and C. N. R. Rao, *J. Mater. Chem.*, **18**, 2191 (2008).

5. Dielectric properties, thermal decomposition and related aspects of $BiAlO_3$, **R. V. K. Mangalam**, S. V. Bhat, A. Iyo, Y. Tanaka, A. Sundaresan and C. N. R. Rao, *Solid State Commun.*, **146**, 435 (2008).

6. Crystal structure and dielectric properties of ordered perovskites Ba_2BiSbO_6

and $BaSrBiSbO_6$, **R. V. K. Mangalam**, E. Suard and A. Sundaresan, *Physica B*, **404**, 154 (2009).

7. Multiferroic properties of $BaTiO_3$ nanoparticles, **R. V. K. Mangalam**, Nirat Ray, Umesh V. Waghmare, A. Sundaresan and C. N. R. Rao, *Solid State Commun.*, **149**, 1 (2009).

8. Itinerant ferromagnetism to insulating spin glass in $SrRu_{1-x}Cu_xO_3$ ($0 \leq x \leq 0.3$), **R. V. K. Mangalam** and A. Sundaresan, *Mater. Res. Bull.* (2008) **In Press**.

9. Pressure-dependent phase transition in the ordered $BaBi_{0.7}Nb_{0.3}O_3$ perovskite, **R. V. K. Mangalam**, C. Narayana and A. Sundaresan, *communicated*.

10. Identifying defects in multiferroic nanocrystalline $BaTiO_3$ by positron annihilation techniques, **R. V. K. Mangalam**, Mahuya Chakrabrati, D. Sanyal, A. Chakrabati and A. Sundaresan, *communicated*.

11. Unusual structure and dielectric properties of a new ordered pervoskite Sr_2Bi SbO_6, **R. V. K. Mangalam**, S. Malo, C. Lepoittevin, G. Van Tendeloo, A. Sundaresan and B. Raveau, *communicated*.

Other miscellaneous publications:

1. Ferroelectricity in $Bi_{26-x}M_xO_{40-\delta}$ (M = Al and Ga) with the γ-Bi_2O_3 structure, **R. V. K. Mangalam**, R. Ranjith, A. Iyo, A. Sundaresan, S. B. Krupanidhi and C. N. R. Rao, *Solid State Commun.*, **140**, 42 (2006).

2. Interface dominated biferroic $La_{0.6}Sr_{0.4}MnO_3$/0.7Pb($Mg_{1/3}$ $Nb_{2/3}$)O_3 - 0.3 ($PbTiO_3$) epitaxial superlattices, A. R. Chaudhuri, R. Ranjith, S. B. Krupanidhi, **R. V. K. Mangalam** and A. Sundaresan, *Appl. Phys. Lett.*, **90**, 122902 (2007).

3. Realization of biferroic properties in $La_{0.6}Sr_{0.4}MnO_3$/0.7Pb($Mg_{1/3}$ $Nb_{2/3}$)O_3 - 0.3 ($PbTiO_3$) epitaxial superlattices, A. R. Chaudhuri, R. Ranjith, S. B. Krupanidhi, **R. V. K. Mangalam**, A. Sundaresan, S. Majumdar and S. K. Ray, *J. Appl. Phys.*, **101**, 114104 (2007).

Contents

CHAPTER 1

Overview of ferroics and multiferroics

1.1 Introduction

A ferroic material is one which can, or can be conceived to, undergo one or more ferroic phase transitions. A phase transition is called a ferroic phase transition if: (a) it can be viewed as a nondisruptive modification of a certain "prototypic phase", and (b) it involves a loss of one or more point-symmetry operators present in the prototype. By "nondisruptive modification" it means that the new phase can be described by it's symmetry elements, Wyckoff positions, atomic parameters, etc., in the frame of reference of the other phase, after making continuous distortions that do not themselves entail any additional change of symmetry [1]. Ferroic materials are being used in many technological applications. Ferroics is the generic name given to the study of ferromagnets, ferroelectrics, and ferroelastics. This chapter deals the main aspects of ferromagnets, ferroelectrics and multiferroics.

1.2 Ferromagnets

Around 600 B.C., magnetism was observed in loadstone or magnetite by its power to attract iron [2]. It has been claimed that sometimes before 2500 B.C. Chinese used magnetic compass. Socrates mentioned that magnetite was used to induce iron to get the attractive power (magnetism). Thus permanent and induced magnetism were human's earliest scientific discoveries. The science behind operation

of magnetic compass enlightened only after the realization of the fact that the earth itself was a huge magnet by Gilbert. Later, Coulomb's investigations in 16^{th} century form the starting point in the research to understand magnetism.

The magnetic effects, except diamagnetism, observed in inorganic materials are due to the presence of unpaired electrons. Thus magnetism is mainly observed in compounds having transition metals and lanthanides due to the presence of unpaired d and f electrons respectively. The random orientations of unpaired electrons on the different atoms lead the material to be paramagnetic. Parallel alignment of these unpaired electrons makes the material as ferromagnetic. If they align in antiparallel, then the material becomes antiferromagnetic. In case of unequal magnetic moment of the spins in antiparallel alignment will lead to ferrimagnetic behavior. However among the different magnetic behaviors, materials having ferromagnetism are widely used in application.

Most of the ferromagnetic materials known are metallic and there are considerable number of insulating ferromagnetic compounds. The ferromagnetism observed in those insulating compounds are explained on the basis of superexchange interaction. Even though superexchange interaction has been explained earlier, a considerably more satisfactory system of semi-empirical rules was developed over a period of years by Goodenough [3] and Kanamori [4]. These rules have the important features of the occupation of various d levels as dictated by ligand field theory. They are related to the prescriptions of Andersons work about the sign of superexchange [5]. The exchange interaction in magnetic insulators is predominantly caused by the so-called superexchange which is due to the overlap of the localized orbitals of the magnetic electrons with those of intermediate ligands. The main features of the superexchange interactions are usually explained in terms of the so-called Goodenough- Kanamori-Anderson rules [4, 6, 7]. According to these

rules, a 180^o superexchange (the magnetic ion-ligand-magnetic ion angle is 180^o) of two magnetic ions with partially filled d shells is strongly antiferromagnetic, whereas a 90^o superexchange interaction is ferromagnetic and much weaker.

1.3 Ferroelectrics

In 1921, Valasek first observed the phenomena, ferroelectricity, in the Rochelle salt ($KNaC_4H_4O_64H_2O$). However, it took many years to unveil its importance in technological applications, especially in memory devices [8].

Ferroelectricity is a physical property of a material whereby it exhibits a spontaneous electric polarization, the direction of which can be switched between equivalent states by the application of an external electric field. The term 'ferroelectricity' is a misnomer referred in analogous to ferromagnetism. Similar to ferromagnetic materials in which the system show a magnetic hysteresis by an applied magnetic field, the ferroelectric materials show the ferroelectric hysteresis by an applied electric field. Thus, the prefix "ferro", meaning iron, is used to describe the property despite the fact that most ferroelectric materials do not have iron in their lattice.

To know the importance of the ferroelectric materials, let's go back to 20^{th} century and think that you are in the last minute of typing your project report. Suddenly the power goes, your computer shuts down. Your final changes are lost. Then you wish to have a memory system in the computer which immediately and automatically stores everything that you write even if the power goes off. Then the memory system, you need is a fast and random-access solid state memory which is cheap, reliable and most importantly it is intrinsically nonvolatile. Now come back to 21^{st} century what we have now is the non-volatile ferroelectric random-access memories (NVFRAMs) which are realizable using the ferroelectric materials.

A colossal increase in the research on ferroelectric materials came in 1950s, leading to the widespread use of barium titanate ($BaTiO_3$) based ceramics in capacitor applications and piezoelectric transducer devices. Since then, many other ferroelectric materials including lead titanate ($PbTiO_3$), lead zirconate titanate (PZT), lead lanthanum zirconate titanate (PLZT), and relaxor ferroelectrics like lead magnesium niobate (PMN) have been developed and utilized for various of applications. Later many new applications have emerged with the development of ceramic processing and thin film technology. Ferroelectrics are key materials in microelectronics. Their excellent dielectric properties make them viable candidate for electronic components such as tunable capacitors, non volatile memories, piezoelectric materials for medical ultrasound imaging and actuators, and electro-optic materials for data storage and displays.

1.3.1 Symmetry

Absence of inversion symmetry and polar nature of ferroelectric crystals cause a spontaneous polarization along one or more crystal axes. Thus the symmetry plays a key role in these materials.

The symmetry of the crystals is governed by their lattice structure. Though there are thousands of crystals in nature, they all can be grouped together into 230 space groups based on the symmetry elements. The space groups in three dimensions are made from combinations of 32 crystallographic point groups with 14 Bravais lattices which belong to one of 7 crystal systems. The 32 point groups can be further classified into (a) crystals having center of symmetry and (b) crystals which do not possess center of symmetry. Crystals with center of symmetry include 11 point groups are labeled as centrosymmetric and they do not show

polarity. The remaining 21 point groups do not have center of symmetry (i.e. non-centrosymmetric). All non-centrosymmetric point groups, except the point group 432, show piezoelectric effect along the unique directional axes. A crystal having no center of symmetry possesses one or more crystallographically unique directional axes. Space groups lacking an inversion center (non-centrosymmetric) are further divided into polar and chiral types. A chiral space group is one without any rotoinversion symmetry elements. Rotoinversion (also called an 'inversion axis') is rotation followed by inversion; for example, a mirror reflection corresponds to a two-fold rotoinversion. Chiral space groups must therefore only contain (purely) rotational and translational symmetry. These arise from the crystal point groups 1, 2, 3, 4, 6, 222, 422, 622, 32, 23, and 432. Chiral molecules such as proteins crystallize in chiral space groups. The term 'polar' is often used for those space groups which are neither centrosymmetric nor chiral. However the term 'polar' is more correctly used for any space group containing a unique anisotropic axis. These occur in point groups 1, 2, 3, 4, 6, m, $mm2$, $3m$, $4mm$, and $6mm$. Thus some chiral space groups are also polar. Out of the twenty point groups which show the piezoelectric effect, the ten polar point groups have only one unique direction axis and such crystals show spontaneous polarization.

Thus considering symmetry restrictions, all ferroelectric materials are pyroelectric, however not all pyroelectric materials are ferroelectric. Since all pyroelectric materials are piezoelectric, this means ferroelectric materials are inherently piezoelectric.

1.3.2 Origin of ferroelectricity in perovskite oxides

In the ferroelectric perovskites like $BaTiO_3$ and $PbTiO_3$, the hybridization between Ti $3d$ states and O $2p$ states is responsible for polarization [9]. In both $PbTiO_3$ and $BaTiO_3$, Ti strongly distorted. Further in $PbTiO_3$, Pb $6s$ and O $2p$ states are strongly hybridized, but Ba $5p$ does not hybridize with the valence band. The Pb-O bonding interaction, the smaller ionic radius of Pb^{2+} compared to Ba^{2+}, leads to a larger strain in $PbTiO_3$ that reduces some Pb-O distances; the Ti-O repulsion prevents the volume shrinking enough to stabilize the cubic phase. There is also an indirect effect on the Ti-O interaction through the Pb-O hybridization. Cohen *et al.*, based on theoretical calculations, has shown dipolar electron density around Pb (Pb-O states) with increasing ferroelectric distortions. In contrast, Ba does not polarize with ferroelectric distortion. Further Cohen *et al.* described that the inhibition of Ti-O hybridization makes the ferroelectric instability to disappear and the cubic phase becomes more stable based on non-empirical model calculations using the potential induced breathing model which assumes spherical ions and no covalency.

1.4 Multiferroics

Multiferroics are the materials that exhibit more than one primary ferroic order parameter simultaneously as defined by H. Schmid in 1994 [10]. Ferromagnetism, ferroelectricity, ferroelasticity and ferrotoroidicity form the four basic primary ferroic order parameters and ferrotoroidicity is still being under debate. However recently, the definition of multiferroics has been expanded to include non-primary order parameters, such as antiferromagnetism or ferrimagnetism. It would appear as contradiction to have a material which is ferroelectric and also ferromagnetic

or antiferromagnetic, since the former requires empty d-orbitals while the latter requires d-electrons and therefore, multiferroics are rare in nature. Multiferroic properties in most materials are actually attained through novel mechanisms, such as frustrated magnetism, lone-pair effects, charge-ordering and local noncentrosymmetry.

Most multiferroic materials belong to the group of perovskite transition metal oxides which includes rare earth manganates ($TbMnO_3$ and $HoMn_2O_5$) and ferrites ($LuFe_2O_4$). Other examples are $BiMnO_3$, $BiFeO_3$ and non-oxides such as $BaNiF_4$ and spinel chalcogenides, $ZnCr_2Se_4$. Apart from single phase multiferroics, composites and heterostructures exhibiting more than one ferroic order parameter are studied extensively. Some examples include magnetic thin films on piezoelectric PMN-PT substrates and Metglass/PVDF/Metglass trilayer structures. Besides scientific interest in their physical properties, multiferroics have potential for applications in actuators, switches, magnetic field sensors and new types of electronic memory devices.

Research on multiferroic materials started since 1960s [11]. In most general sense the field of multiferroics was born from studies of magnetoelectric systems. Even though the field is known from 1960, a huge leap in the multiferroic research occurred only after 2000. Recent discovery of large ferroelectric polarization in epitaxially grown $BiFeO_3$ thin films [12] and strong magnetodielectric observed in orthorhombic $TbMnO_3$ [13] and $TbMn_2O_5$ [14] re-stimulated activity in the field of multiferroics.

1.4.1 Symmetry

As the crystal symmetry plays a key role in ferroelectric properties, it is well clear that multiferroic property is closely linked to symmetry. The primary ferroic properties (Table 1.1) can be characterized by their behavior under space and time inversion. Space inversion, for example, will reverse the direction of polarization (P), while leaving the magnetization (M) invariant. Time reversal, in turn, will change the sign of M, while the sign of P remains invariant. Magnetoelectric multiferroics require simultaneous violation of space and time inversion symmetry.

Table 1.1: Ferroics - symmetry

Symmetry	**Space Invariant**	**Space Variant**
Time Invariant	Ferroelastic	Ferroelectric
Time Variant	Ferromagnetic	Ferrotoroidic

1.4.2 Types of multiferroics

1.4.2.1 Lone pair multiferroics

In usual perovskite-based ferroelectrics like $BaTiO_3$, the ferroelectric distortion occurs due to the displacement of B-site cation (Ti) with respect to the oxygen octahedral cage. Here the transition metal ion (Ti in $BaTiO_3$) requires an empty d shell since the ferroelectric displacement occurs due to the hybridization between Ti $3d$ states and O $2p$ states. This normally excludes any net magnetic moment because magnetism requires partially filled d shells. However the partially filled d shell on the B-site reduces the tendency of perovskites to display ferroelectricity.

In order for the coexistence of magnetism and ferroelectricity (multiferroic), one possible mechanism is lone-pair driven [15] where the A-site cation drives the

displacement and partially filled d shell on the B-site contributes to the magnetism. Examples include $BiFeO_3$ [16], $BiMnO_3$ [17], $PbVO_3$. In the above materials, the A-site cation (Bi^{3+} and Pb^{2+}) has $6s^2$ lone-pair which causes the Bi $6p$ (empty) orbital to come closer in energy to the O $2p$ orbitals. This leads to hybridization between the Bi $6p$ and O $2p$ orbitals and drives the off-centering of cation towards the neighboring anion resulting in ferroelectricity.

1.4.2.2 Charge ordered multiferroics

In manganates, that are less than half doped, there is a type of charge ordering that is intermediate between site-centred and bond-centered. Such a state breaks inversion symmetry and is predicted to be magnetic and ferroelectric [18]. Charge ordering in the manganates is interesting because charge-ordering is resulting due to localization of charges therefore it is associated with insulating and antiferromagnetic (or paramagnetic) behavior. But double-exchange gives rise to metallicity along with ferromagnetism. Therefore a competition arises between ferromagnetic metallic and charge ordered antiferromagnetic insulating states [19]. charge ordering can occur in compounds containing ions of mixed valence with geometrical or magnetic frustration. These ions form a polar arrangement causing improper ferroelectricity (i.e. no ionic displacement). If magnetic ions are present, a coexisting magnetic order can be established and coupled to ferroelectricity. Charge ordered ferroelectricity is suggested in Fe_3O_4 and (Pr,Ca)MnO_3 [20]. Another prominent example for a charge ordered multiferroic is $LuFe_2O_4$, which shows improper ferroelectricity below 330 K and ferrimagnetic behavior occurs below 240 K [21]. The arrangement of electrons arises from the charge frustration in a triangular lattice, with the mixed valence state of Fe^{2+} and Fe^{3+} ions.

1.4.2.3 Geometrically frustrated multiferroics

Geometric frustrated multiferroicity is related to a structural phase transition at high temperature. Compounds belong to this important class of multiferroics are K_2SeO_4, Cs_2CdI_4 and hexagonal $RMnO_3$. These systems are prototypical multiferroics which can be understood by competition between local interactions in several ion sites. For example, in hexagonal manganates, h-$RMnO_3$ (R=Ho-Lu, Y) the ferroelectric polarization at high temperature is correlated to lattice distortions through off-centering of ions [22–24]. Geometric frustration gives rise to novel spin arrangements at low temperature: the spins order in a variety of non-collinear, e.g. (in-plane) triangular or Kagomé structures in order to relieve the geometric frustration. The coexistence of ferroelectric and magnetic order occurs together with a strong coupling between two disparate order parameters. The mechanism of the ferroelectric ordering in hexagonal $RMnO_3$ is still questionable in scientific community and must be understood before a comprehensive picture of multiferroic phenomena in spin frustrated systems can be built. It is still a matter of debate whether the geometric distortion is the origin of electric polarization or the off-centering of Mn ions also contributes to the polarization.

Physical properties of geometric multiferroics are dominated by the behavior of d-shell electrons (e_g-orbitals) of the transition metal ions and unfilled f-shell of the rare earth ions. Hexagonal manganates show the largest deviation from perovskite structure due to the small size of rare-earth ions. Although geometrically frustrated multiferroics exhibit a simple chemistry, they provide a unique set of physical properties, such as rich phase diagrams and multiple frustrations. The strong coupling between ferroelectric and magnetic orders is represented by an anomaly in the static dielectric constant at magnetic phase transitions.

1.4.2.4 Magnetically driven ferroelectricity

Magnetically driven multiferroics are insulating materials, mostly oxides, in which macroscopic electric polarization is induced by magnetic long-range order. A necessary but not sufficient condition for the appearance of spontaneous electric polarization is the absence of inversion symmetry. In these materials inversion symmetry is broken by magnetic ordering. Such a symmetry breaking often occurs in so-called frustrated magnets, where competing interactions between spins favor unconventional magnetic orders. The microscopic mechanisms of magnetically induced ferroelectricity involve the polarization of electronic orbitals and relative displacement of ions in response to the magnetic ordering.

Many multiferroics show the cycloidal spiral ordering, in which spins rotate around an axis perpendicular to the propagation vector of the spiral. The induced electric polarization is orthogonal to the propagation vector and lies in the spiral plane. An abrupt change of the spiral plane induced by magnetic field results in the corresponding rotation of the polarization vector. In $DyMnO_3$, this transition is accompanied by the 600 % increase of dielectric constant (the giant magnetocapacitance effect) [25]. The microscopic mechanism of magnetodielectric in spiral multiferroics involves spin-orbit coupling.

E-type antiferromagnet (ortho-$HoMnO_3$): In the presence of strong uniaxial anisotropy, as in the antiferromagnetic next-nearest neighbor interactions model, competing interaction can stabilize a periodic collinear spin arrangement of the up-up-down-down type. Such a spin modulation commensurate with structural or charge modulation can induce electric polarization via exchange striction mechanism that does not require spin-orbit coupling [26].

1.4.3 Magnetoelectric effect

The magnetoelectric (ME) effect is a phenomenon of inducing magnetic polarization by applying an electric field and vice versa. The effects can be linear or/and non-linear with respect to the applied fields. In general, this effect depends on temperature. The effect can be expressed in the following form

$$P_i = \alpha_{ij}\Sigma H_j + \Sigma\beta_{ijk}H_jH_k + ...$$
$$M_i = \alpha_{ij}\Sigma E_j + \Sigma\beta_{ijk}E_jE_k + ...$$

where P is the electric polarization, M, the magnetization, E and H, the electric and magnetic fields, and α and β are the linear and nonlinear ME susceptibilities. The effect can be observed in single phase and composite materials. Some examples of single phase magnetoelectrics are Cr_2O_3 [27], and multiferroic materials which show a coupling between magnetic and electric order parameters. Composite magnetoelectrics are combinations of magnetostrictive and electrostrictive materials, such as ferromagnetic and piezoelectric materials. The size of the effect depends on the microscopic mechanism. In single phase magnetoelectrics, the effect can be due to the coupling of magnetic and electric orders as observed in some multiferroics. In composite materials the effect originates from interface coupling effects, such as strain. Some of the promising applications of ME effect are sensitive detection of magnetic fields, advanced logic devices and tunable microwave filters [27].

CHAPTER 2

Experimental details: synthesis, structure and properties

This chapter describes various methods of synthesis, structural characterization and details of the various physical property measurements studied in this work.

2.1 Material synthesis

2.1.1 Solid state reaction

The most widely used method for the preparation of polycrystalline solids is the direct heating of a mixture of powder starting materials, referred as solid state reaction method [28]. The reaction temperatures are usually high, often 1000 to 1500 ^{o}C, in order for the reaction to occur at appreciable rate. Both thermodynamic and kinetics factors are important in solid state reaction. Thermodynamic factors determine whether or not a particular reaction should occur by considering the change in free energy that are involved, whereas kinetic factors decide the rate of reaction. In solid state reaction between two solids (powder), the actual reaction to form the product occurs at the interface. Hence the possible rate controlling steps in the reaction are transport of matter to the reaction interface, reaction at the interface and transfer of matter away from the reaction interface.

2.1.2 High pressure and high temperature technique

High pressure and high temperature technique varies from simple opposed anvil arrangement to more complex designs involving three or four anvils. In this technique, the sample is effectively squeezed between pistons. Phases synthesized at high pressures tend to have higher densities than those synthesized at ambient pressure and thus sometimes give rise to unusually high coordination numbers. It is also possible to stabilize ions in unusual oxidation states, such as Cr^{4+}, Cr^{5+}, Cu^{3+}, Ni^{3+} and Fe^{4+}. Hence this technique is used to prepare unusual crystal structures. Cubic anvil and belt apparatus, discussed below, are used for the high pressure and high temperature synthesis of some of the compounds that are reported in this thesis. The cubic anvil and belt apparatus facilities available at National Institute of Advanced Industrial Science and Technology (AIST), Tsukuba, Japan has been utilized for the sample synthesis.

2.1.2.1 Cubic anvil apparatus

Cubic anvil high pressure apparatus has six pistons arranged in a cubic fashion (RIKEN CAP 07) as shown in figure 2.1. A homogeneous pressure is achieved for the sample by using this technique when the equal pressures applied in six directions. The specifications of the instrument used are as follows. The maximum pressure that can be applied using this instrument is 5.5 GPa (450 tonnes). The sample can be treated with a maximum temperature of 1350 ^{o}C. Figure 2.2 shows the schematic diagram of the sample preparation procedure using this technique. The precursor, starting oxide powders mixture, is pelletized and capsulated with gold. The gold capsule will be covered with a cylinder made using NaCl with 20 % ZrO_2. This cylinder will be again covered with a graphite cylinder and kept inside

a Pyrophyllite ($Al_2Si_4O_{10}(OH)_2$) cell through the cylindrical hole. After placing the graphite cylinder at the centre, both sides of the hole will be covered with molybdenum plate and stainless ring with pyrophyllite at the centre (Fig. 2.2). The pyrophyllite cell will be kept in the high pressure apparatus. The desired pressure for the formation of phase will be applied to the cell. Then follows the heat treatment for 2 hours. After 2 hours, the heater was switched off and the cell was allowed to cool to room temperature and the pressure was reduced slowly. The solid sample was removed from the Au capsule.

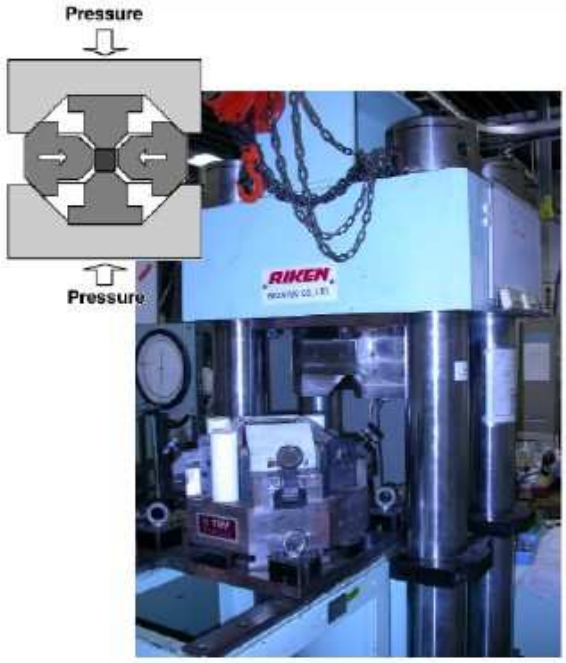

Figure 2.1: Cubic anvil apparatus

Using cubic anvil, approximately 0.4 g of sample can be prepared in a single attempt. In the cell, Pyrophyllite acts as a gasket, graphite is used as heater and NaCl is a good thermal conductor and at same time provides electrical insulation. The gold capsule is provided to avoid the reaction of the sample with the cell materials

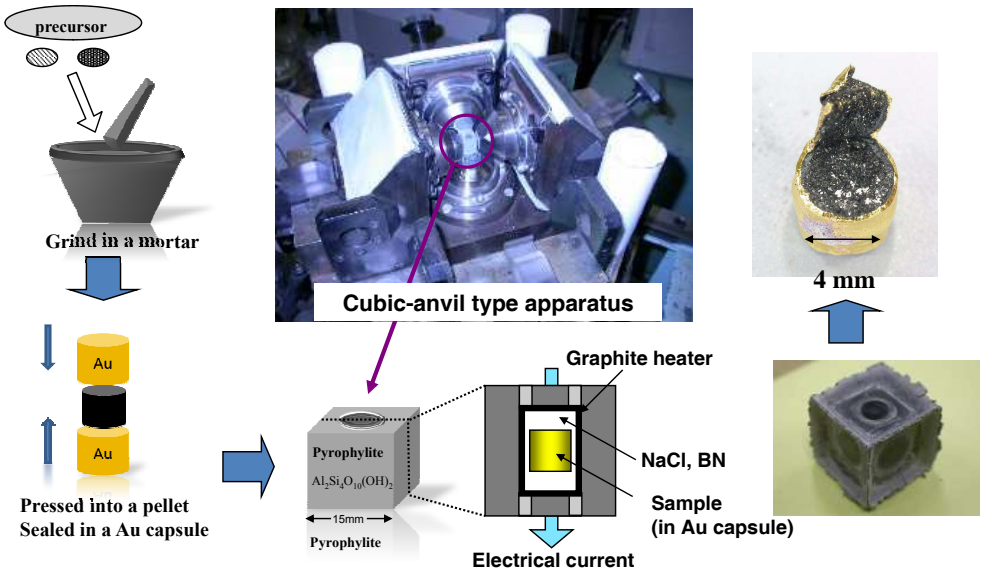

Figure 2.2: Procedure for sample preparation in cubic anvil apparatus

2.1.2.2 Belt apparatus

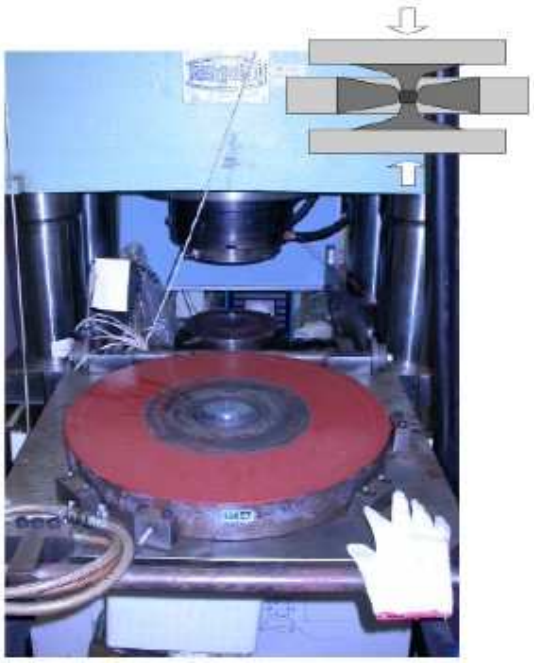

Figure 2.3: Belt apparatus

Belt apparatus is usually used for large scale synthesis at high pressure and high

temperature in comparison with cubic anvil. A sample amount of approximately 3 g can be prepared in a single reaction. However the pressure applied to the sample is only from two sides rather than six sides as in cubic anvil and hence the pressure homogeneity is difficult to achieve in this technique. The belt apparatus used for our sample preparation is shown in figure 2.3. The cell preparation for the high pressure treatment is also similar to that of cubic anvil. With this belt apparatus a maximum pressure of 7.5 GPa (600 tonnes) and temperature of 1500 ^{o}C can be achieved.

2.1.3 Wet chemical synthesis

Even though solid state reaction is a solvent-less reaction, atomic scale mixing of reactants is a major drawback of this method and thus sometimes leads to inhomogeneity in the reaction product. There are various wet chemical methods in which the mixing of reactants at the atomic scale can be achieved and their reaction temperatures are low compare to that of solid state reaction method [28].

The sol-gel process is a wet-chemical technique for the synthesis of materials (typically metal oxides) starting either from a chemical solution (*sol* short for solution) or colloidal particles (*sol* for nanoscale particle) to produce an integrated network (*gel*). Sol-gel method is probably the oldest soft chemistry route that enables the synthesis of several oxide materials which is being used even today. Typical precursors are metal alkoxides and metal chlorides, which undergo hydrolysis and polycondensation reactions to form a colloid; a system composed of solid particles (size ranging from 1 nm to 1 μm) dispersed in a solvent. The *sol* evolves and then follows the formation of an inorganic continuous network containing a liquid phase (*gel*). Formation of a metal oxide involves connecting the metal cen-

ters with oxo (M-O-M) or hydroxo (M-OH-M) bridges and therefore generating metal-oxo or metal-hydroxo polymers in solution. The drying process serves to remove the liquid phase from the gel thus forming a porous material, then a thermal treatment (firing) may be performed in order to favor further polycondensation and to obtain metal oxide powders.

2.2 Structure and morphology

2.2.1 Structural analysis: Diffraction techniques

Diffraction techniques, such as x-ray, electron and neutron diffraction are a family of non-destructive analytical techniques which reveal information about the crystallographic structure, chemical composition and physical properties of materials.

2.2.1.1 Powder x-ray diffraction

In powder x-ray diffraction (XRD) technique, the polycrystalline or powdered solid samples are analyzed to find the crystallographic structure, crystallite size (grain size) and preferred orientation [28]. This technique is used to identify unknown substances, by comparing diffraction data against the database maintained by the International Centre for Diffraction Data (ICDD).

2.2.1.1.1 Bragg's law

Generally diffraction occurs when x-rays encounter obstacles whose size is comparable with the wavelength of x-ray. If the wavelength is short enough, atoms can serve as diffraction obstacle. Crystals are regular arrays of atoms. Since x-rays are waves of electromagnetic radiation, atoms can scatter x-ray waves, primarily through the atom's electrons. An x-ray striking an electron produces secondary

spherical waves emanating from the electron. This phenomenon is known as scattering, and the electron is known as the scatterer. A regular array of scatterers produces a regular array of spherical waves. Although these waves cancel out one another in most directions (destructive interference), they add constructively in a few specific directions determined by Bragg's law

$$2d \sin\theta = n\lambda \tag{2.1}$$

where d is an interplanar distance, θ, Bragg angle, λ, wavelength of the x-ray used and n is an integer. These specific directions appear as spots on the diffraction pattern, often called reflections. Thus x-ray diffraction results from an electromagnetic wave (x-ray) impinging on a regular array of scatterers (the repeating arrangement of atoms within the crystal). X-rays are used to produce the diffraction pattern because their wavelength λ is typically the same order of magnitude (1-100 Å) as the spacing d between planes in the crystal. X-rays interact primarily with the electron cloud surrounding each atom. The contribution to the diffracted x-ray intensity is therefore larger for atoms with a large atomic number (Z) than it is for atoms with a small Z.

2.2.1.1.2 Phase identification

Powder x-ray diffraction is widely used in the identification and characterization of crystalline solids as each of which produces a distinctive diffraction pattern. Thus provides a fingerprint for comparison as the positions corresponding to lattice spacing and the relative intensity of the line are indicative of a particular phase and material. Hence a multi-phase mixture will show more than one pattern superposed allowing for determination of relative concentration. J.D. Hanawalt, an analytical chemist who worked for Dow Chemical in 1930s, was the first to realize

the analytical potential of creating a database for x-ray diffraction. Today it is represented by the Powder Diffraction File (PDF) of the International Centre for Diffraction Data. These databases are interfaced to a wide variety of diffraction analysis software and distributed globally.

2.2.1.1.3 Crystallinity

X-ray diffraction produces pattern consist of series of sharp peaks due to the crystalline nature of the materials. In the case of amorphous materials (liquids, glasses, etc.), it produces a broad background signal. Many polymers show semicrystalline behavior, i.e. a part of the material forms an ordered crystallite by folding of the molecules. The crystallinity percent in such compounds can be determined using powder XRD by comparing the integrated intensity of the background pattern to that of the sharp peaks.

2.2.1.1.4 Lattice parameters

The size and shape of the unit cell of crystalline phase determines the position of a diffraction peak. Each peak is characteristic of a certain lattice plane and therefore corresponds to a Miller index. Indexing the peaks for a high symmetry material, e.g. cubic or hexagonal, is quite easy even for an unknown phase. Complex cases can be dealt with the indexing programs available, but if the unit cell is very large and the symmetry is low (triclinic), success is not always guaranteed.

2.2.1.1.5 Phase transitions

Powder x-ray diffraction gives a pattern characteristic of a phase of the material and hence the transformation of one phase to another of the same material can be differentiated. Thus the technique can be used to analyze the phase transitions

of the materials as a function of temperature or pressure. Near the phase transition, new diffraction peaks will appear or old ones will disappear according to the symmetry of the new phase. The transition will be sharp and discontinuous for a first order phase transition, whereas it will be broad and continuous for second order. If the material melts, all sharp lines will disappear and replaced by a broad amorphous pattern. In some cases there will be split or coalesce of peaks, e.g. if the material undergoes a continuous second order phase transition. In such cases the symmetry may change, because the existing structure is distorted rather than replaced by a completely different one. For example the diffraction peaks for the lattice planes (100) and (001) can be found at two different values of θ for a tetragonal phase, but if the symmetry becomes cubic the two peaks will coincide.

2.2.1.1.6 Crystal structure

Crystal structure determination from powder diffraction data is extremely challenging due to the overlap of reflections in a powder experiment, while comparing to that of single crystal analysis. Rietveld refinement can be carried out on the powder XRD data to obtain the refined crystal structural parameters of the material by using a initial structural model that is similar to the material under investigation. Section 2.3.1.3 discusses more about the Rietveld refinement

2.2.1.2 Powder neutron diffraction

Neutron diffraction, similar to x-ray diffraction, is a crystallographic method for the determination of atomic structure of a material. However neutron diffraction is a very expensive technique as it requires a neutron source. A sample to be examined is placed in a beam of thermal or cold neutrons and the diffraction intensity pattern of the sample gives information of the structure of the material. Upon impinging

on a crystalline sample, neutrons will scatter under a limited number of well-defined angles according to the Bragg law that describes x-ray diffraction. Neutron diffraction is a more powerful technique to the solve structure of materials having light atoms especially hydrogen in hydrides, hydrates and organic moieties and oxides materials.

The interaction of neutrons with matter is different than x-rays. Neutrons interact directly with the nucleus of the atom rather than the electron cloud surrounding each atom which happens as in case of x-ray. Hence the contribution of each isotope to the diffraction intensity is different; for example, hydrogen and deuterium contribute differently. The scattering length varies from isotope to isotope rather than linearly with atomic number. Thus even in the presence of large Z atoms, the light (low Z) atoms contribute strongly to the diffraction intensity. The high resolution data of neutron diffraction helps to obtain very precise values for the atomic positions in the structure. Although neutrons are uncharged, they carry a spin and therefore interact with magnetic moments, including those arising from the electron cloud around an atom. Therefore neutron diffraction can reveal the magnetic structure of a material. As magnetic scattering is caused by the much larger electron cloud around the tiny nucleus, it does require an atomic form factor. Therefore towards higher angles, the intensity of the magnetic contribution to the diffraction peaks will dwindle.

2.2.1.2.1 Instrumental requirements

For performing a neutron diffraction measurement, a neutron source (nuclear reactor or spallation source) and a neutron detector are required. Normally the sample quantity used in this technique is relatively large compared to those used in x-ray diffraction and hence single crystal analysis is less common using this technique.

The desired neutron wavelength for a measurement can be obtained using crystal monochromators or filters. At a spallation source the time of flight technique is used to sort the energies of the incident neutrons and in that case no need of monochromator. A 64 ^{3}He counting tubes are used as a neutron detectors.

2.2.1.2.2 High-resolution two-axis diffractometer D2B

The Neutron diffraction data used in this thesis work were collected using D2B diffractometer at Institut Laue-Langevin in Grenoble, France. D2B is a very high-resolution powder diffractometer designed to achieve the ultimate resolution, limited only by powder particle size, but it was built so that an alternative high flux option, with resolution comparable to that of D1A (old diffractometer), but much higher intensity, could be chosen at the touch of a button.

The diffractometer D2B is characterized by the very high take-off angle (135^o) for the monochromator, which has a relatively large mosaic spread of $20'$ to compensate for the corresponding intensity (Dl/l) loss. It is 300 mm high, focusing vertically onto about 50 mm; this large incident vertical divergence is matched by 200 mm high detectors and collimators. A complete diffraction pattern is obtained after about 100 steps of 0.025^o in 2θ, since the 64 detectors are spaced at 2.5^o intervals. Such scans take typically 30 minutes; they are repeated to improve statistics.

D2B is well suited for the Rietveld refinement of relatively large structures, such as zeolites with absorbed molecules. It has as well proved successful for the solution of some of the new 'quasi-crystalline' materials. It was also designed for work on magnetism and high resolution of very large d-spacings using wavelengths of between 2.4 and 6 Å. Wavelengths can easily be changed under computer control, since they are all obtained by a simple rotation within the Ge[hhl] plane. A large

graphite filter can be switched to provide a very clean beam at 2.4 Å and a cold Be-filter can be used for longer wavelengths.

Table 2.1: D2B diffractometer details

Monochromator	
28 Ge[115] crystals of 1 x 5 x 1 cm^3	
take-off-angle	135^o
Germanium [hkl]	wavelengths λ/Å
557	1.051
337	1.277
551	1.464
335	1.594(optimum λ)
331	2.398
113	3.152
flux at sample $\lambda = 1.594$ Å	Å 10^6 high resolution Å 10^7 high intensity
Sample	
beam size at sample	2 x 5 cm^2
angular range	$5^o < 2\theta < 165^o$ $0^o < \omega < 360^o$
Detectors	
64 ^{3}He counting tubes	
background without sample	0.1 Hz
Sample environment	
cryostat	1.5 - 300 K
cryofurnace	1.5 - 525 K
furnace	200 - 1000 K
dilution cryostat	50 - 4000 mK
pressure cell	2 GPa and 4 - 300 K

2.2.1.3 Rietveld refinement

Rietveld refinement is a technique devised by Hugo Rietveld for use in the characterization of crystalline materials [29]. The neutron and x-ray diffraction of powder samples results in a pattern characterized by peaks in intensity at certain angles, 2θ. The height, width and position of these peaks can be used to determine many aspects of the materials structure. The Rietveld method uses a least squares approach to refine a theoretical line profile until it matches the measured profile. The introduction of this technique was a significant step forward in the diffraction analysis of powder samples as, unlike other techniques at that time, it was able to deal reliably with strongly overlapping reflections. The method was first reported for the diffraction of monochromatic neutrons where the peak position is reported in terms of the Bragg angle, 2θ. This terminology will be used here, although the technique is equally applicable to alternative scales such as x-ray energy or neutron time-of-flight.

2.2.1.3.1 Peak shape

The shape of a powder diffraction peak is influenced by the characteristics of the beam, experimental arrangement and the sample size and shape. In the case of monochromatic neutron sources, the convolution of the various effects has been found to result in a peak almost exactly Gaussian in shape. If this distribution is assumed then the contribution of a given peak to the profile y_i at position $2\theta_i$ is:

$$y = I_k \left\{ -4ln \left(\frac{2}{H_k^2} \right) (2\theta_i - 2\theta_k)^2 \right\} \tag{2.2}$$

where H_k is the full width at half-maximum, $2\theta_k$, the centre of the peak and I_k is the calculated intensity of the peak (determined from the structure factor, Lorentz

factor and multiplicity of the reflection). At very low diffraction angles the peaks may acquire an asymmetry due to the vertical divergence of the beam. Rietveld used a semi-empirical correction factor to account for this asymmetry

$$A_s = 1 - \left[\frac{sP(2\theta_i - 2\theta_k)^2}{\tan\theta_k}\right] \tag{2.3}$$

where P is the asymmetry factor and s is +1,0 and -1 depending on the difference, $2\theta_i$-$2\theta_k$ being positive, zero and negative respectively. At a given position more than one diffraction peak may contribute to the profile. The intensity is simply the sum of all peaks contributing at $2\theta_i$.

2.2.1.3.2 Peak width

The width of the diffraction peaks are found to broaden at higher Bragg angles. This angular dependency is represented by

$$H_k^2 = U\tan^2\theta_k + V\tan\theta_k + W \tag{2.4}$$

where U, V and W are the halfwidth parameters and can be refined during the fit.

2.2.1.3.3 Refinement

In Rietveld method, the atomic positions, isothermal parameters and preferred orientation parameter can be refined. The principle of Rietveld method is to minimize a function M which represents the difference between a calculated profile y(calc) and the observed data y(obs). Rietveld defined such an equation as:

$$M = \sum_i W_i \left\{ y_i^{obs} - \frac{1}{c} y_i^{cal} \right\}^2 \tag{2.5}$$

where W_i is the statistical weight and c is an overall scale factor such that $y^{calc} = cy^{obs}$

2.2.2 Morphology: Scanning electron microscopy

Scanning electron microscope (SEM) is one of the most versatile and widely used tools of modern science as it allows the study of morphology and composition of the materials. By scanning an electron probe across a specimen, high resolution images of the morphology or topography of a specimen, with great depth of field, at very low or very high magnifications can be obtained. SEM uses a focussed electron beam to scan small areas of solid samples. Secondary electrons emitted from the sample are collected to create an area map of the secondary emissions. Since the intensity of secondary emission is very dependent on local morphology, the area map is a magnified image of the sample. The SEM also produces images of high resolution, which means that closely spaced features can be examined at a high magnification.

SEM consists of an electron gun, electron lenses, a scanning system and an electron detector [30]. The electron gun provides a source of electrons. In a typical SEM, an electron beam is thermionically emitted from an electron gun fitted with a tungsten filament cathode. Tungsten is normally used in thermionic electron guns because it has the highest melting point and lowest vapour pressure of all metals, thereby allowing it to be heated for electron emission. Other types of electron emitters include are lanthanum hexaboride (LaB_6) cathodes and field emission guns (FEG). FEG may be a cold-cathode type using tungsten single crystal emitters or a thermally-assisted Schottky type using emitters of zirconium oxide.

Back-scattered electrons (BSE) are the electrons that are reflected from the

sample by elastic scattering. BSE are often used in analytical SEM along with the spectra made from the characteristic x-rays. Because the intensity of the BSE signal is strongly related to the atomic number (Z) of the specimen, BSE images can provide information about the distribution of different elements in the sample. Characteristic x-rays are emitted when the electron beam removes an inner shell electron from the sample, causing a higher energy electron to fill the shell and release energy. These characteristic x-rays are used to identify the composition and measure the abundance of elements in the sample.

For imaging in the conventional SEM, specimens must be electrically conductive, at least at the surface, and electrically grounded to prevent the accumulation of electrostatic charge at the surface. Nonconductive specimens tend to charge when scanned by the electron beam and especially in secondary electron imaging mode, this causes scanning faults and other image artifacts. They are therefore usually coated with an ultrathin electrically-conducting material, commonly gold, deposited on the sample. Coating prevents the accumulation of static electric charge on the specimen during electron irradiation.

A field-emission cathode in the electron gun of a SEM provides narrower probing beams at low as well as high electron energy, resulting in both improved spatial resolution and minimized sample charging and damage. Field-emission scanning electron microscope (FESEM) produces clearer, less electrostatically distorted images with spatial resolution down to 1½ nm which is 3 to 6 times better than conventional SEM. Smaller-area contamination spots can be examined at electron accelerating voltages compatible with energy dispersive x-ray spectroscopy. Reduced penetration of low kinetic energy electrons probes closer to the immediate material surface. High quality and low voltage images are obtained with negligible electrical charging of samples (accelerating voltages range from 0.5 to 30 kV)

and the need for placing conducting coatings on insulating materials is virtually eliminated.

2.3 Physical property measurements

2.3.1 Dielectric measurements

A material is classified as "dielectric" if it has the ability to store energy when an external electric field is applied [31]. The dielectric material increases the storage capacity of the capacitor by neutralizing charges at the electrodes, which ordinarily would contribute to the external field. The capacitance with the dielectric material is related to dielectric constant. If a DC voltage source V is placed across a parallel plate capacitor (Fig. 2.4), more charge is stored when a dielectric material is between the plates than if no material (a vacuum) is between the plates.

C and C_0 are capacitance with and without dielectric. $\kappa' = \varepsilon'_r$ is the real dielectric

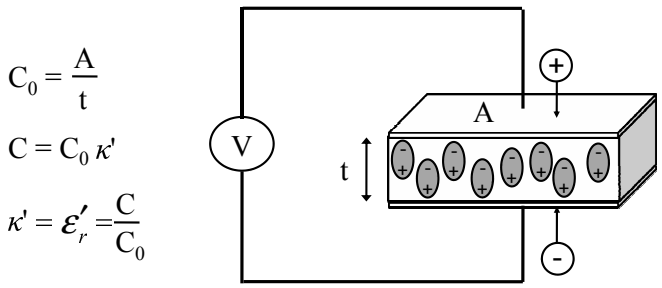

Figure 2.4: Parallel plate capacitor, DC case

constant or permittivity and A and t are the area of the capacitor plates and the distance between them (Fig. 2.4). The dielectric material increases the storage capacity of the capacitor by neutralizing charges at the electrodes, which ordinarily

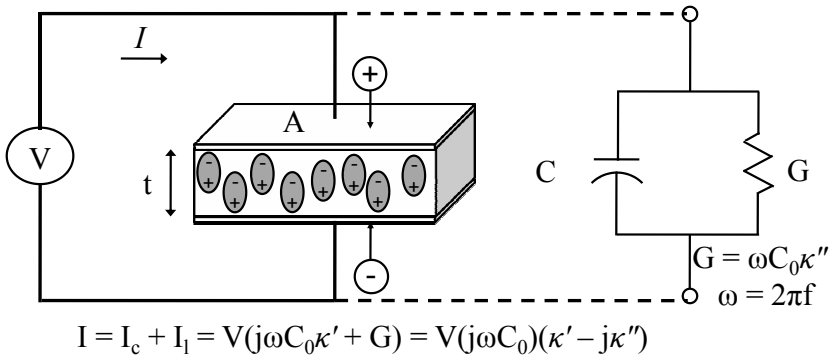

Figure 2.5: Parallel plate capacitor, AC case

would contribute to the external field. The capacitance of the dielectric material is related to the dielectric constant as indicated in the above equations. If an AC sinusoidal voltage source V is placed across the same capacitor (Fig. 2.5), the resulting current will be made up of a charging current I_c and a loss current I_l that is related to the dielectric constant. The losses in the material can be represented as a conductance (G) in parallel with a capacitor (C).

The complex dielectric constant κ consists of a real part κ' which represents the storage and an imaginary part κ'' which represents the loss. The following notations are used for the complex dielectric constant interchangeably:

$$\kappa = \kappa^* = \varepsilon_r = \varepsilon_r^*. \tag{2.6}$$

From the point of view of electromagnetic theory, the definition of electric displacement (electric flux density) D_f is:

$$D_f = \varepsilon E \tag{2.7}$$

where $\varepsilon = \varepsilon^* = \varepsilon_0 \varepsilon_r$ is the absolute permittivity (or permittivity), ε_r is the relative permittivity, $\varepsilon_0 = (1/36\pi) \times 10^{-9}$ F/m is the free space permittivity and E is the

electric field. Permittivity describes the interaction of a material with an electric field, E and is a complex quantity.

$$\kappa = \frac{\varepsilon}{\varepsilon_0} = \varepsilon_r = \varepsilon_r' - j\varepsilon_r'' \tag{2.8}$$

Dielectric constant (κ) is equivalent to relative permittivity (ε_r) or the absolute permittivity (ε) relative to the permittivity of free space (ε_0). The real part of permittivity (ε_r') is a measure of how much energy from an external electric field is stored in a material. The imaginary part of permittivity (ε_r'') is called the loss factor and is a measure of how dissipative or lossy a material is to an external electric field. The imaginary part of permittivity (ε_r'') is always greater than zero and is usually much smaller than (ε_r'). The loss factor includes the effects of both dielectric loss and conductivity. When complex permittivity is drawn as a simple vector diagram (Fig. 2.6), the real and imaginary components are 90^o out of phase. The vector sum forms an angle δ with the real axis (ε_r'). The relative "lossiness" of a material is the ratio of the energy lost to the energy stored.

$$\tan\delta = \frac{\varepsilon_r''}{\varepsilon_r'} = \mathrm{D} = \frac{1}{\mathrm{Q}}$$

$$= \frac{\text{Energy Lost per Cycle}}{\text{Energy Stored per Cycle}}$$

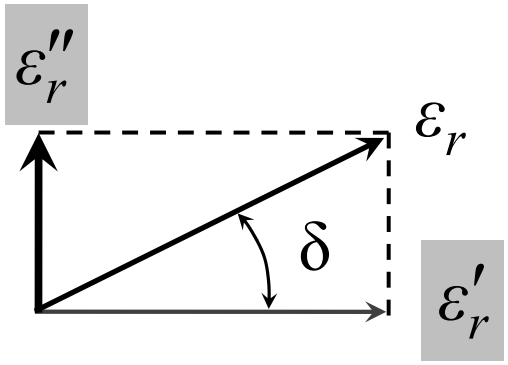

Figure 2.6: Loss tangent vector diagram

The loss tangent or tanδ is defined as the ratio of the imaginary part of the dielectric constant to the real part. D denotes dissipation factor and Q is quality

factor. The loss tangent tanδ is tangent loss or dissipation factor. Sometimes the term "quality factor or Q-factor" is used with respect to an electronic microwave material, which is the reciprocal of the loss tangent. For very low loss materials, since tan$\delta = \delta$, the loss tangent can be expressed in angle units, milliradians or microradians.

A material may have several dielectric mechanisms or polarization effects that contribute to its overall permittivity (Fig. 2.7). A dielectric material has an arrangement of electric charge carriers that can be displaced by an electric field. The charges become polarized to compensate for the electric field such that the positive and negative charges move in opposite directions.

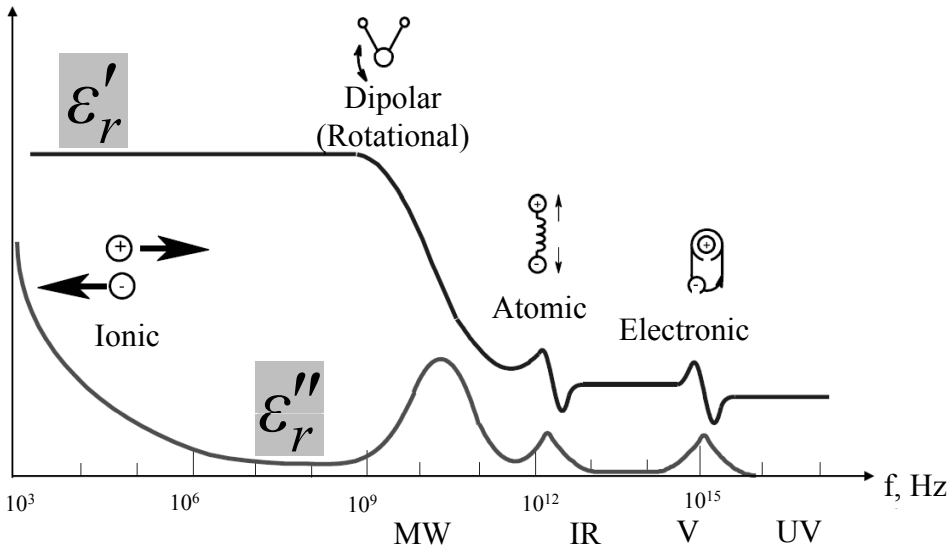

Figure 2.7: Frequency response of dielectric mechanisms

At the microscopic level, several dielectric mechanisms can contribute to dielectric behavior. Dipole orientation and ionic conduction interact strongly at microwave frequencies. Water molecules, for example, are permanent dipoles, which rotate to follow an alternating electric field. These mechanisms are quite lossy which explains why food heats in a microwave oven. Atomic and electronic mecha-

nisms are relatively weak and usually constant over the microwave region. Each dielectric mechanism has a characteristic "cutoff frequency". As frequency increases, the slow mechanisms drop out in turn, leaving the faster ones to contribute to ε'. The loss factor (ε''_r) will correspondingly peak at each critical frequency. The magnitude and "cutoff frequency" of each mechanism is unique for different materials. Water has a strong dipolar effect at low frequencies but its dielectric constant rolls off dramatically around 22 GHz. Teflon, on the other hand, has no dipolar mechanisms and its permittivity is remarkably constant well into the millimeter-wave region. A resonant effect is usually associated with electronic or atomic polarization. A relaxation effect is usually associated with orientation polarization.

2.3.2 Ferroelectric hysteresis

Ferroelectric hysteresis is a measure of polarization induced due to the applied electric field. The hysteresis measurement is the most general and common tool for characterizing a ferroelectric sample [32].

The ferroelectric measurements of this thesis work has been carried out using Radiant Technologies Precision Workstation In this measurement, a voltage waveform is applied to the sample in a series of voltage steps. At each voltage step, the current induced in the sample by the voltage step is integrated and the integral value is captured and converted into polarization (μC/cm^2)

$$\frac{\mu C}{cm^2} = \frac{Q}{Area} = \frac{CV}{Area} = \frac{Integrator\ Volts \times Sense\ Capacitor}{Sample\ Area} \tag{2.9}$$

The voltage waveform is normally a standard bipolar triangular waveform that can be simply defined by providing the maximum voltage and the entire duration of the waveform in milliseconds. The sign of the voltage indicates the direction of the first

leg of the waveform. The number of points is controlled primarily by the duration of the waveform, though it may also be adjusted by the voltage. The software automatically computes the number of points and provides the maximum number possible for the conditions specified. The waveform begins at 0 V and steps to a maximum value of the assigned voltage. It then proceeds to step to the negative of the assigned maximum. Finally it steps back to 0 V. A DC bias level may be assigned that will allow the entire waveform to be shifted from 0 V symmetry without losing the waveform symmetry. Note that care must be taken that at no time do the combination of the DC bias level and the step voltage exceed the capabilities of the Precision hardware configuration. The entire Standard Bipolar waveform structure is shown in figure 2.8.

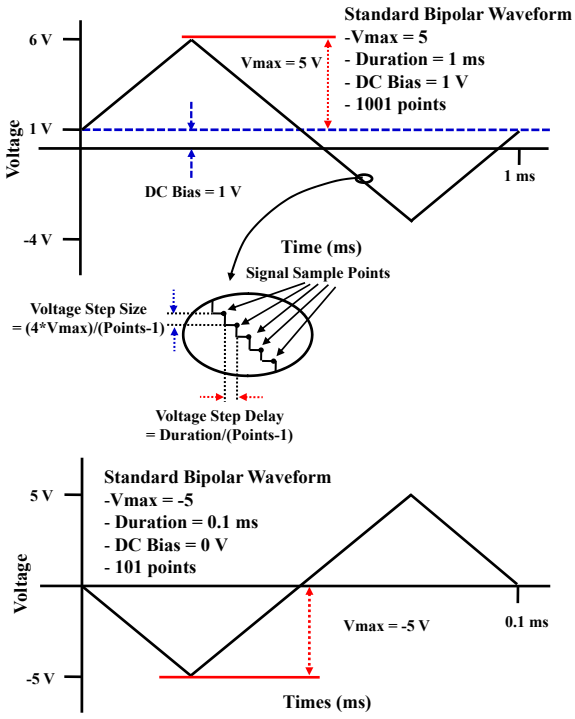

Figure 2.8: Standard Bipolar waveform

In these examples, the number of points is first set to the maximum of 1001. Then, if the duration is too short, the number is reduced to the point where the

minimum step delay times the number of points is near the duration. A low voltage may also influence the number of points downward as the minimum voltage step must be observed. Finally, the duration itself will be adjusted so that it can accommodate an exact integer number of minimum step delays. The step delay is consistent between points and is the duration of the waveform divided over the number of steps (Points - 1). The voltage step is equal to four times the maximum voltage divided over the number of steps. The integrated value is sampled at the end of the step delay, just before the next voltage step is taken.

The standard bipolar waveform produces five derived parameters of interest. These are:

$\mathbf{P}_{Max}$: Polarization at the maximum applied voltage. Note that this will be the polarization at +5 V in both the examples.

$+\mathbf{P}_r$: Polarization at zero volts when voltage is moving from positive to negative. If V_{Max} is negative, this will be the polarization at the final sample point.

$-\mathbf{P}_r$: Polarization at zero volts when voltage is moving from negative to positive. If V_{Max} is positive, this will be the polarization at the final sample points.

$+\mathbf{V}_c$: Voltage at which polarization is zero when switching from negative to positive.

$-\mathbf{V}_c$: Voltage at which polarization is zero when switching from positive to negative.

2.3.3 DC Magnetic Measurements

Various magnetometers have been devised to study magnetic materials. Vibrating sample magnetometer (VSM) is one among the instruments that are used relatively

widespread for magnetic measurements. Since its invention forty years ago, it has become the workhorse in both laboratory and production environments for measuring the basic magnetic properties of materials as a function of magnetic field and temperature. Computer control and automation was introduced to the VSM two decades ago, but otherwise there have been no major advancements in performance until quite recently.

The VSM employs an electromagnet which provides the magnetizing field (DC), a vibrator mechanism to vibrate the sample in the magnetic field and detection coils which generate the signal voltage due to the changing flux emanating from the vibrating sample. The output measurement displays the magnetic moment M as a function of the field H. The magnetic field is usually generated by an electromagnet driven by a DC bipolar power supply. If extremely high magnetic fields are required ($>$ 3 T), the electromagnet is replaced by a superconducting solenoid [33].

The voltage V measured across the sensing coils in a VSM can be expressed as the product of four contributing sources:

$$V = M \times A \times F \times S \tag{2.10}$$

where,

M = magnetic moment of the sample,

A = amplitude of vibration,

F = frequency of vibration and

S = sensitivity function of the sensing coils.

2.3.4 AC Magnetic Measurements

AC magnetic measurements, in which an AC field is applied to a sample and the resulting AC moment is measured, are an important tool for characterizing magnetic materials [33]. Since the induced sample moment is time-dependent, AC measurements yield information about magnetization dynamics which are not obtained in DC measurements, where the sample moment is constant during the measurement time. AC magnetic measurements of this thesis work were carried out using Physical Property Measurement System (PPMS) of Quantum Design, USA.

In AC magnetic measurements, a small AC drive magnetic field is superimposed on the DC field, causing a time-dependent moment in the sample. The field of the time-dependent moment induces a current in the pickup coils, allowing measurement without sample motion. The detection circuitry is configured to detect only in a narrow frequency band, normally at the fundamental frequency of the AC drive field.

In order to understand what is measured in AC magnetometry, first consider very low frequencies where the measurement is most similar to DC magnetometry. In this case the magnetic moment of the sample follows the M(H) curve that would be measured in a DC experiment. As long as the AC field is small, the induced AC moment is $M_{AC} = (dM/dH) \cdot H_{AC} \sin(\omega t)$, where H_{AC} is the amplitude of the driving field, ω, the driving frequency and $\chi = dM/dH$ is the slope of M(H) curve, called susceptibility. The susceptibility is the quantity of interest in AC magnetometry.

As the DC applied magnetic field is changed, different parts of the M(H) curve are accessed, giving a different susceptibility. One advantage of the AC measure-

ment is already evident: the measurement is very sensitive to small changes in M(H). Since the AC measurement is sensitive to the slope of M(H) and not to the absolute value, small magnetic shifts can be detected even when the absolute moment is large.

At higher frequencies than those considered above, the AC moment of the sample does not follow along the DC magnetization curve due to dynamic effects in the sample. For this reason, the AC susceptibility is often known as the dynamic susceptibility. In higher frequency case the magnetization of the sample may lag behind the drive field, an effect that is detected by the magnetometer circuitry. Thus the AC magnetic susceptibility measurement yields two quantities: the magnitude of the susceptibility, χ and the phase shift, φ (relative to the drive signal). Alternately one can think of the susceptibility as having an in-phase or real component χ' and an out-of-phase or imaginary component χ''. The two representations are related by

$$\begin{aligned} \chi' &= \chi \cos\varphi \\ \chi'' &= \chi \sin\varphi \end{aligned} \qquad \Longleftrightarrow \qquad \begin{aligned} \chi &= \sqrt{\chi'^2 + \chi''^2} \\ \varphi &= \arctan(\chi''/\chi') \end{aligned} \tag{2.11}$$

In the limit of low frequency, where AC measurement is most similar to a DC measurement, the real component χ' is just the slope of the M(H) curve discussed above. The imaginary component, χ'' indicates dissipative processes in the sample. In conductive samples the dissipation is due to eddy currents. Relaxation and irreversibility in spin-glasses give rise to a nonzero χ''. In ferromagnets a nonzero imaginary susceptibility can indicate irreversible domain wall movement or absorption due to a permanent moment. Also both χ' and χ'' are very sensitive to thermodynamic phase changes and are often used to measure transition temper-

atures. AC magnetometry allows one to probe all of these interesting phenomena. Typical measurements to access this information are χ vs. temperature, χ vs. driving frequency, χ vs. DC field bias, χ vs. AC field amplitude and harmonic measurements.

2.3.5 Heat capacity

Heat capacity (C_p) is the measure of heat energy required to increase the temperature of an object by a certain temperature interval [33]. Heat capacity is an extensive property because its value is proportional to the amount of material in the object; for example a bathtub of water has a greater heat capacity than a cup of water. Heat capacity is usually expressed in units of J/K. Heat capacity measurements of this thesis work were carried out using Physical Property Measurement System (Quantum Design, USA). The Quantum Design Heat Capacity measures the heat capacity at constant pressure,

$$C_p = \left(\frac{dQ}{dT}\right)_p \tag{2.12}$$

As with other techniques for measuring heat capacity, the Quantum Design Heat capacity option controls the heat added to and removed from a sample while monitoring the resultant change in temperature. During a measurement, a known amount of heat is applied at constant power for a fixed time and then this heating period is followed by a cooling period of the same duration.

In the heat capacity measurement puck a platform heater and platform thermometer are attached to the bottom side of the sample platform (Fig. 2.9). Small wires provide the electrical connection to the platform heater and platform thermometer and also provide the thermal connection and structural support for the

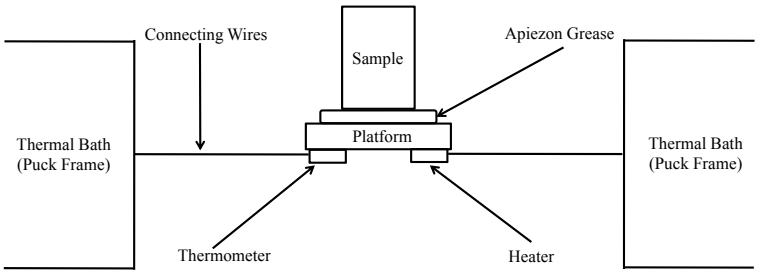

Figure 2.9: Thermal connections to sample and sample platform in the heat capacity measurement

platform. The sample is mounted to the platform by using a thin layer of apiezon grease, which provides the required thermal contact to the platform. Sufficient vacuum is created so that thermal conductance between the sample platform and the thermal bath is totally dominated by the conductance of the wires. This gives a reproducible heat link to the bath with a corresponding time constant large enough to allow both the platform and sample to achieve sufficient thermal equilibrium during the measurement.

Different measurement techniques [34] are optimized for different sample sizes and accuracy requirements. The Quantum Design Heat Capacity option uses a relaxation technique that combines the best measurement accuracy with robust analysis techniques. After each measurement cycle (which is a heating period followed by a cooling period), the heat capacity option fits the entire temperature response of the sample platform to a model that accounts for both the thermal relaxation of the sample platform to the bath temperature and the relaxation between the platform and the sample itself [35]. The effect of the relaxation between the sample platform and sample must be considered when the thermal connection shared by the sample and platform is poor. By modeling this effect, the software

can report the correct heat capacity values despite such poor contact.

2.3.6 Vibrational spectroscopy: Infrared and Raman

Infrared (IR) and Raman spectroscopy are spectroscopic tools used in identifying the characteristic vibrational modes of the samples. In general atoms are known to vibrate in solids at frequencies of approximately 10^{12} to 10^{13} Hz. The vibrational modes, involving pairs or groups of bonded atoms, can be excited to higher energy states by absorption of radiation of appropriate frequency.

2.3.6.1 Infrared spectroscopy

The infrared portion of the electromagnetic spectrum is divided into three regions; the near-, mid- and far- infrared, named for their relation to the visible spectrum. The far-infrared, approximately 400-10 cm^{-1} (30-1000 μm), lying adjacent to the microwave region, has low energy and may be used for rotational spectroscopy. The mid-infrared, approximately 4000-400 cm^{-1} (1.4-30 μm), may be used to study the fundamental vibrations and associated rotational-vibrational structure. The higher energy near-IR, approximately 14000-4000 cm^{-1} (0.8-1.4 μm), can excite overtone or harmonic vibrations. The names and classifications of these subregions are merely conventions. They are neither strict divisions nor based on exact molecular or electromagnetic properties.

Infrared spectroscopy exploits the fact that molecules have specific frequencies at which they rotate or vibrate corresponding to discrete energy levels (vibrational modes). These resonant frequencies are determined by the shape of the molecular potential energy surfaces, the masses of the atoms and by the associated vibronic coupling. In order for a vibrational mode in a molecule to be IR active, it must

be associated with changes in the permanent dipole. In particular, in the Born-Oppenheimer and harmonic approximations, i.e. when the molecular Hamiltonian corresponding to the electronic ground state can be approximated by a harmonic oscillator in the neighborhood of the equilibrium molecular geometry, the resonant frequencies are determined by the normal modes corresponding to the molecular electronic ground state potential energy surface. Nevertheless, the resonant frequencies can be in a first approach related to the strength of the bond and the mass of the atoms at either end of it. Thus the frequency of the vibrations can be associated with a particular bond type.

2.3.6.2 Raman spectroscopy

Raman spectroscopy is a spectroscopic technique used in condensed matter physics and chemistry to study vibrational, rotational and other low-frequency modes in a system. It relies on inelastic scattering or Raman scattering of monochromatic light, usually from a laser in the visible, near infrared or near ultraviolet range. The laser light interacts with phonons or other excitations in the system, resulting in the energy of the laser photons being shifted up or down. The shift in energy gives information about the phonon modes in the system. Infrared spectroscopy yields similar, but complementary information.

Typically a sample is illuminated with a laser beam and the light from the illuminated spot is collected with a lens and sent through a monochromator. Wavelengths close to the laser line, due to elastic Rayleigh scattering, are filtered out while the rest of the collected light is dispersed onto a detector.

The Raman effect occurs when light impinges upon a molecule and interacts with the electron cloud of the bonds of that molecule. The incident photon excites one of the electrons into a virtual state. For the spontaneous Raman effect, the

molecule will be excited from the ground state to a virtual energy state and relax into a vibrational excited state, which generates Stokes Raman scattering. If the molecule was already in an elevated vibrational energy state, the Raman scattering is then called anti-Stokes Raman scattering. A molecular polarizability change or amount of deformation of the electron cloud with respect to the vibrational coordinate is required for the molecule to exhibit the Raman effect. The amount of the polarizability change will determine the Raman scattering intensity, whereas the Raman shift is equal to the vibrational level that is involved.

CHAPTER 3

Structural and dielectric studies on Bi(Al/Ga)O_3 **

3.1 Introduction

Ferroelectric materials have been the subject of intensive research owing to their technological applications. These materials are widely being used in devices such as, storage capacitors, smart structures in microelectromechanical systems, pyroelectric detectors and microwave resonators. The well known ferroelectric material used in many applications is the distorted perovskite (Fig. 3.1), $PbZr_{1-x}Ti_xO_3$ (PZT). It has a high Curie temperature ($T_C \sim 360\ ^oC$) and exhibits a large electric polarization due to the influence of the stereochemical activity of Pb: $6s^2$ lone pair electrons [36]. During the last two decades, the impact of our modern lifestyle on the environment has moved from debates on local environment to global environment issues. The word "recycling" is popping up in almost any industry niche and the electronic industry is no exception. At present the EU-parliament is about to accept a proposal of completely removing lead from all industries due to the toxicity of lead, which has adverse effects on the nervous and reproductive systems of mammals and birds [37]. This decision's major impact on the electronic industries is focused on the use of lead-containing solders in their products. But the law might be formed in a way that will force companies using Pb or other heavy metals to show that there exists no better material choice than Pb. Thereby, companies can get a licence to continue the use of Pb in their products. It might be difficult

Paper based on this work has been published in *Solid state commun.* **146 (2008) 435.

though for a company to defend its device, if any other company is manufacturing the same device with other more environmentally friendly material choices. For example: PZT which contains 60 weight percent Pb versus $SrBi_2Ta_2O_9$ (SBT) which does not contain Pb. PZT might be affected by these kinds of environmental laws while SBT may not. However SBT does not have as good polarizability characteristics as PZT. Concerning the environmental issues, may be it is about time that the new lead-free material has to be discovered with equivalent or superior properties [36, 38].

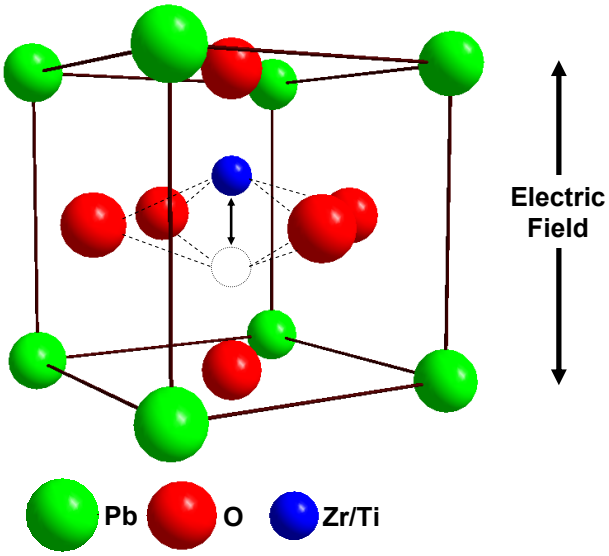

Figure 3.1: Lead zirconate titanate

Figure 3.2 shows the comparison of the piezoelectric charge constants d_{33} at 25 ^{o}C among lead free ceramics and conventional PZT ceramics as a function of Curie temperature [38]. To date, the lead-free piezoelectric ceramics that have been extensively studied belong to the perovskite (e.g. $BaTiO_3$ and $(NaBi)TiO_3$) and bismuth-layered (e.g. $Bi_4Ti_3O_{12}$) structures. Besides these two families, piezoelectricity has also been identified in the ferroelectric tungsten bronze family. Neurgaonkar *et al.* have systematically investigated tungsten bronze ferroelectric

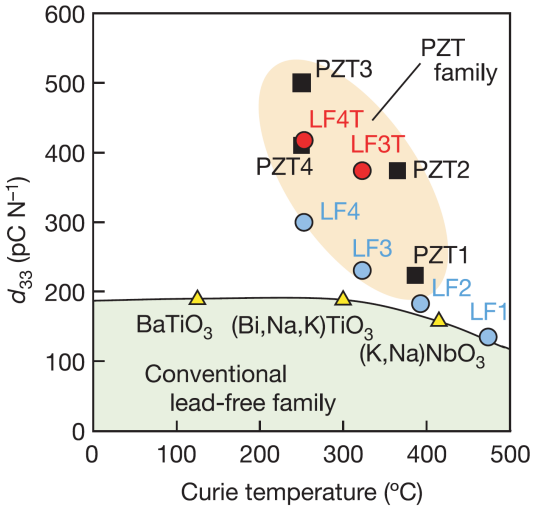

Figure 3.2: Comparison of the piezoelectric charge constants d_{33} at 25 ^{o}C among lead free (LF) ceramics and conventional PZT ceramics as a function of Curie temperature. Recently reported LF series:$[(K_{0.5}Na_{0.5})_{1-x}Li_x](Nb_{1-y}Ta_y)O_3$; LF1, LF2 and LF3 are (x,y) = (0.06,0), (x,y) = (0.04,0.10), (x,y) = (0.03,0.20). LF4: $(K_{0.44}Na_{0.52}Li_{0.04})(Nb_{0.86}Ta_{0.10}Sb_{0.04})O_3$. LF3T and LF4T: textured ceramics with the same compositions as LF3 and LF4, respectively. PZT1: $Pb(Zr_{0.52}Ti_{0.48})O_3$. PZT2: $Pb_{0.988}(Zr_{0.48}Ti_{0.52})_{0.976}Nb_{0.024}O_3$. PZT3: commercially available PZT. PZT4: $[(Pb_{0.85}Ba_{0.15})_{0.9925}La_{0.005}](Zr_{0.52}Ti_{0.48})O_3$. Reproduced from [38].

crystals and demonstrated encouraging piezoelectric properties in such compounds [39, 40]. According to Neurgaonkar *et al.*, calcium-modified strontium sodium niobates, ($Sr_{2-x}Ca_xNaNb_5O_{15}$, $0.05 \leq x \leq 0.35$), are thought to be potential lead-free piezoelectric materials, which exhibit a large piezoelectric constant of $d_{33} \sim 270$ pC N^{-1} [41].

The polarization in $PbTiO_3$ compound is due to the hybridization between the titanium $3d$ states and the oxygen $2p$ states [9]. There is also a strong hybridization between lead $6s$ and O $2p$ states in this material which has an an indirect effect on the Ti-O interaction [9]. Similarly in the multiferroic compounds such as $BiMnO_3$ and $BiFeO_3$, ferroelectricity originates from the presence of Bi: $6s^2$ lone pair electrons [17, 20]. A large ferroelectric polarization ($\sim$ 90 μC/cm^2) was re-

ported [12] in thin films of $BiFeO_3$ and substantiated on the basis of first-principles calculations [16]. These facts demonstrate that the Bi^{3+} ion with $6s^2$ lone pair would be an alternate candidate to replace the toxic Pb^{2+}:$6s^2$ ion in ferroelectric materials.

However Eerenstein *et al.* [42] recently described the experimental difficulties and associated artefacts that arose during the study of thin epitaxial films of the proposed multiferroic materials $BiFeO_3$ and $BiMnO_3$. The problems experienced include large leakage currents and charge injection from Nb-doped $SrTiO_3$ substrates which are used as bottom electrodes. Charge injection prevents ferroelectric hysteresis loop closure and contributes to the apparent polarization. Leakage currents also contribute to the apparent polarization, and may help explain the large range of polarization values reported in the literature. They also show that magnetoelectric measurements are easily corrupted in the presence of large leakage currents. It's very important that the materials also should have low leakage current to replace PZT.

Recent theoretical calculations using density functional theory within the local density approximation predicted that perovskite-like $BiAlO_3$ (BAO) and $BiGaO_3$ (BGO) with Bi^{3+} ions at the A-site will have large ferroelectric polarization and piezoelectricity [43]. The theoretical calculations shown that BGO will have a similar structure to $PbTiO_3$, although with much stronger tetragonal distortion and therefore improved ferroelectric properties. BAO shares structural characteristics with antiferrodistortive $PbZrO_3$, but it is also a ferroelectric with large polarization. These compounds will likely be an excellent ferroelectric materials with the largest polarizations known; high Curie temperatures and significant piezoelectric response. In addition, since the structures of the two end-point compounds are distinctly different, it is anticipated that a $Bi(Ga,Al)O_3$ solid solution could show

even higher response properties in the region of the phase boundary between the two ground-state structures. Therefore it is proposed that the Bi(Al,Ga)O_3 system as a replacement for the widely used piezoelectric material, PZT, that will avoid the environmental toxicity problems of lead-based compounds. Finally, in both BAO and BGO, the large distortions from the prototypical cubic structure are driven by the stereochemical activity of the Bi:$6s^2$ lone pair. Since these compounds are lead-free, it is of importance to verify this prediction experimentally. Here we report the synthesis, structure and physical properties of BAO and BGO samples prepared at high pressure and high temperature.

3.2 Experimental

A 1:1 ratio of Bi_2O_3 and Al_2O_3/Ga_2O_3 were used as starting materials to prepare BAO and BGO. The preparation carried out at ambient pressure and 750 ^{o}C was not resulted in perovskite BAO and BGO phases. Then the samples were prepared using belt-type high pressure apparatus at 4 GPa and 950 ^{o}C. However we found that still we did get the pure BAO and BGO phases, the details of which discussed later. Finally we prepared this sample using cubic anvil high pressure apparatus at 4.5 GPa and 800 ^{o}C. Prior to this synthesis Bi_2O_3 was preheat at 700 ^{o}C in oxygen atmosphere in order to remove $Bi_2O_2CO_3$, which was found to be crucial in the formation of pure phase. Thermogravimetric analysis (TGA) of the commercially available bismuth oxide indicates that the $Bi_2O_2CO_3$ converts into Bi_2O_3 at 700 ^{o}C (Fig. 3.3) that was confirmed by XRD analysis of the heated sample. Preheated Bi_2O_3 was kept in a dry box to avoid reformation of oxycarbonate impurities. The powders of Bi_2O_3 and Al_2O_3/Ga_2O_3 were mixed in the glove box, pelletized and packed inside a gold capsule for cubic anvil high pressure synthesis.

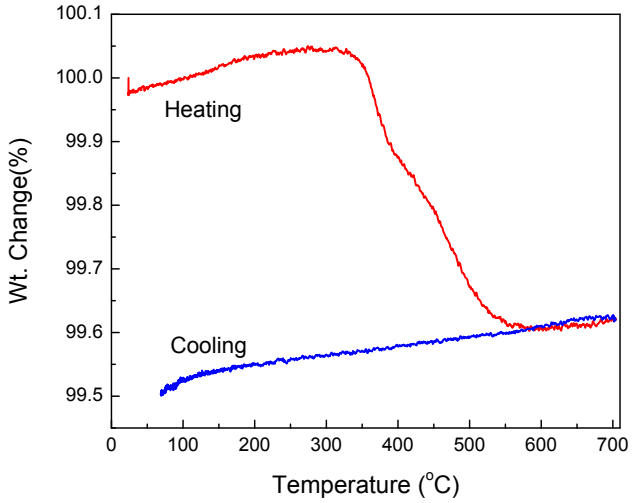

Figure 3.3: Thermogravimetric analysis of the commercially available bismuth oxide

Phase purity of samples was verified with Rigaku x-ray diffractometer using Cu Kα radiation. High temperature XRD data of BAO were collected with Bruker D8 Discover diffractometer using Cu Kα radiation in the temperature range of 30 ^{o}C to 800 ^{o}C in vacuum. Rietveld refinement was carried out on the x-ray data using Fullprof software [44]. Capacitors were prepared by depositing gold on both sides of the pellets using DC sputtering on which the ferroelectric measurements were carried out using Radiant Technologies Precision workstation. Capacitance and dielectric measurements were carried out using Agilent 4294A Impedance analyzer from 100 Hz to 1 MHz in the temperature range of 30 - 500 ^{o}C. Temperature-dependent Raman spectra of BAO were recorded using LabRAM HR800 Raman spectrometer with an Ar laser (514.5 nm) as the excitation source. Thermogravimetric and differential thermal analysis (TG-DTA) was carried out (Mettler Toledo, TG-850) on BAO between room temperature and 700 ^{o}C (heating rate = 10 ^{o}C/min) in oxygen atmosphere.

3.3 Results and discussion

3.3.1 Structural analysis

Our initial attempt to prepare both BAO and BGO at ambient-pressure and 750 ^{o}C resulted in $Bi_{26-x}(Al/Ga)_xO_{40-y}$ (Fig. 3.4) with the γ-Bi_2O_3 structure (Fig. 3.5), having space group I*23*, rather than the predicted perovskite structure [45]. In $Bi_{26-x}M_xO_{40-\delta}$ with γ-Bi_2O_3 structure, Bi^{3+} ion occupies the 24 f site in an unusual heptahedral coordination and M ions occupy the 2a tetrahedral site or both 2a and 24f site depending upon the composition and the valence state of M ions [45, 46]. The oxygen ions are distributed over 24 f site and two sets of 8c sites. Even though the compounds with γ-Bi_2O_3 structure belongs to the non-centrosymmteric space group I*23*, they are non-polar and hence the compounds will be piezoelectric and not ferroelectric.

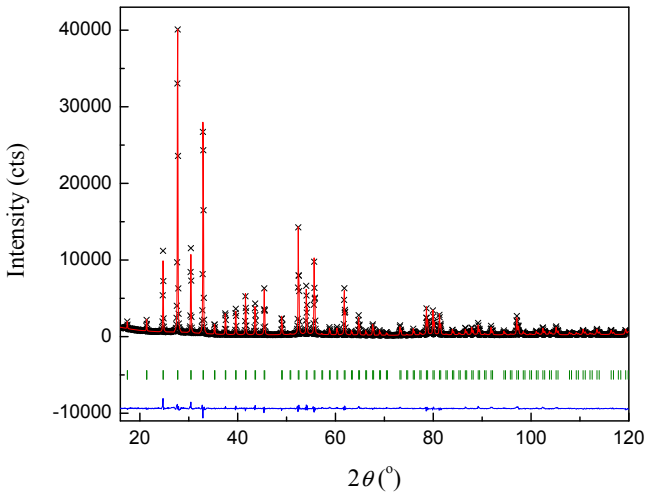

Figure 3.4: Observed, calculated and difference x-ray diffraction pattern of $Bi_{24}Al_2O_{40-\delta}$ phase.

It has been reported that to prepare perovskite structure with Bi^{3+}:6s^2 lone

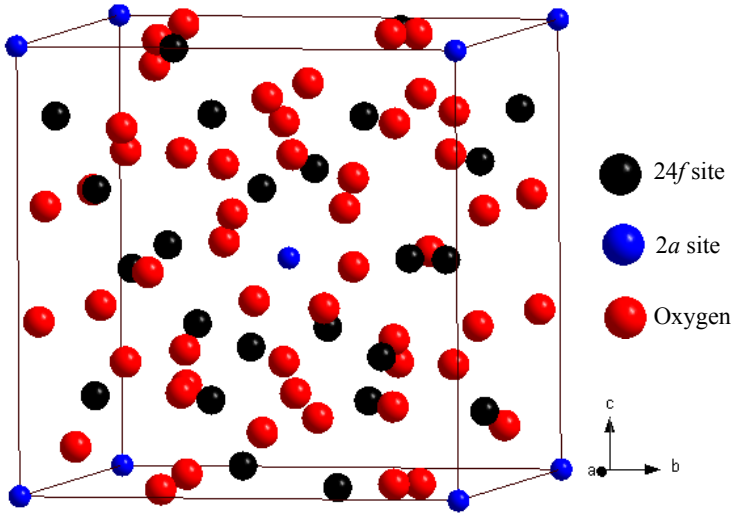

Figure 3.5: $Bi_{24}Al_2O_{40-\delta}$ Structure

pair at A-site needs high pressure and high temperature treatment except $BiFeO_3$. Hence we made an attempt to prepare BAO and BGO at high pressure (4 GPa) and high temperature (950 ^{o}C) using belt-type high pressure apparatus. The product formed with a new phase along with $Bi_{26-x}(Al/Ga)_xO_{40-y}$ and $Bi_2O_2CO_3$.

Meanwhile Belik *et al.* [47] have reported that the compound BAO prepared under 6 GPa and at 1000 ^{o}C has a distorted perovskite structure while the structure of BGO, prepared at 1200 ^{o}C under 6 GPa, is closely related to pyroxene-like KVO_3 structure. BAO is isotypic with multiferroic perovskite-like $BiFeO_3$ and has octahedrally coordinated Al^{3+} ions. BGO has the structure closely related to pyroxene-like KVO_3 with a centrosymmetric orthorhombic symmetry (P*cca*). The GaO_4 tetrahedra in BGO are joined by corners forming infinite $(GaO_3)^{3-}$ chains along the *a* axis. Bi^{3+} ions in BGO have 6-fold coordination. The solid solutions of $BiAl_{1-x}Ga_xO_3$ are found to have a C-centered monoclinic phase structurally related to $PbTiO_3$. However the dielectric properties of these samples have not been reported.

In order to identify the source of $Bi_2O_2CO_3$ impurity in our samples, we analyzed the commercially available bismuth oxide using powder x-ray diffraction. This analysis revealed the presence $Bi_2O_2CO_3$ secondary phase. Thus the source of impurity phase in the final products BAO and BGO is the starting material. Hence commercial Bi_2O_3 was preheated at 700 ^oC in order to remove $Bi_2O_2CO_3$ impurity as shown in TGA in figure 3.3. Finally we prepared the pure phase of BAO successfully, however BGO could not be prepared as a pure phase using cubic anvil high pressure apparatus. These samples were further studied.

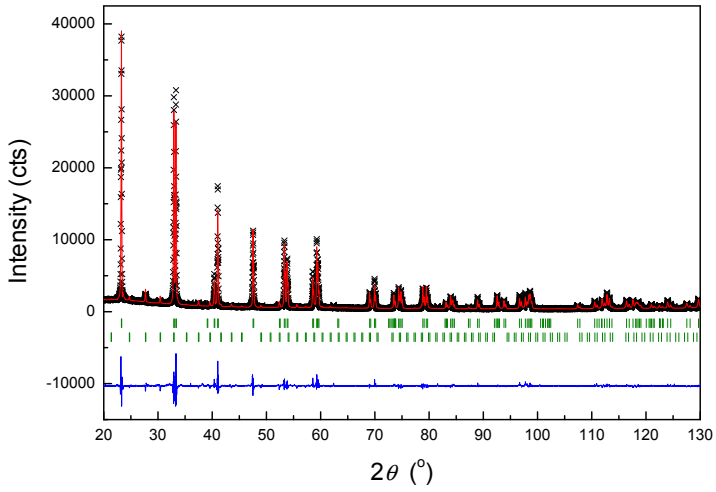

Figure 3.6: Observed, calculated and difference x-ray diffraction patterns of $BiAlO_3$ prepared using cubic anvil high pressure apparatus. Vertical tick marks are symmetry-allowed reflections and the second row corresponds to the $Bi_{24}Al_2O_{40-\delta}$ secondary phase.

Rietveld refinement of the XRD data of BAO gave a structure with rhombohedral symmetry (space group R$3c$) with lattice parameters, $a = 5.3747(4)$ Å and $c = 13.391(1)$ Å in agreement with the literature [43, 47]. The XRD pattern obtained from the final Rietveld refinement is shown in figure 3.6. A small amount (5 %) of $Bi_{26-x}Al_xO_{40-\delta}$ phase is present as a secondary phase. The structural

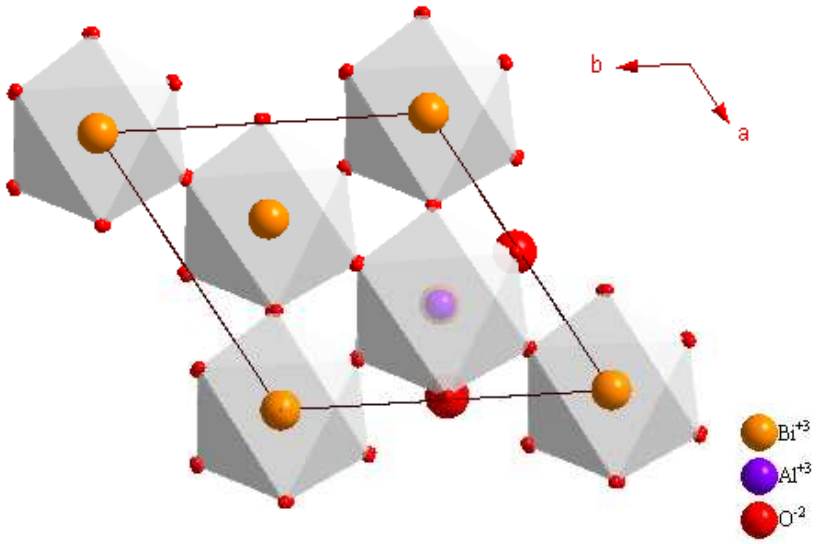

Figure 3.7: $BiAlO_3$ structure

Table 3.1: Structural parameters of $BiAlO_3$ obtained from the Rietveld refinement of XRD data with the space group R*3c*. *Fixed parameters

R*3c*					
a = 5.3763(1)Å and c = 13.3959(1) Å					
Atoms	x	y	z	B	Occupancy
Bi	0	0	0	0.11(1)	1*
Al	0	0	0.2236(3)	0.11(1)	1*
O	0.5(2)	0.013(2)	0.9571(5)	1.5*	3*
R_{Bragg} = 4.53 % and χ^2 = 8.98					

parameters obtained after refinement are shown in table 3.1. Figure 3.7 shows the $BiAlO_3$ structure built from the structural parameters obtained from refinement. The structure shows that Al^{3+} forms octahedral coordination with oxygen and Bi^{3+} ions are coordinated by twelve neighboring oxygen ions.

It is important to note that we are able to prepare $BiAlO_3$ at lower pressures and temperatures comparing to literature work [47] which might have been aided by the removal of CO_2 from bismuthoxycarbonate present in bismuth oxide by

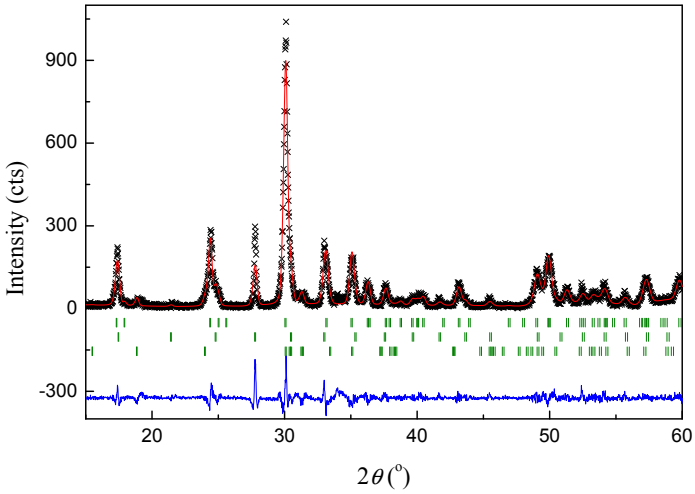

Figure 3.8: Observed, calculated and difference x-ray diffraction patterns of $BiGaO_3$. Vertical tick marks are symmetry-allowed reflections and the second row corresponds to the $Bi_{26-x}Ga_xO_{40-\delta}$ and Ga_2O_3 secondary phase.

preheating.

Profile matching of the XRD data of BGO fit well with space group P*cca* with lattice parameters, $a = 5.4162(2)$ Å, $b = 5.1335(3)$ Å and $c = 9.9369(5)$ Å) in agreement with the literature report [47] rather than predicted distorted perovskite structure similar to $PbTiO_3$. The sample also has an impurity phase of $Bi_{26-x}Ga_xO_{40-\delta}$ of about 20%. The XRD pattern obtained from the profile matching is shown in figure 3.8. The attempt to prepare the solid solution resulted in the mixture of impurity phases as reported in the literature.

3.3.2 Thermal analysis

Differential thermal analysis (DTA) carried out by heating in the temperature range 30 - 700 ^{o}C is shown in figure 3.9. As noted in DTA, there are two peaks, an endothermic one at 550 ^{o}C and an exothermic one at 580 ^{o}C. The cooling curve did

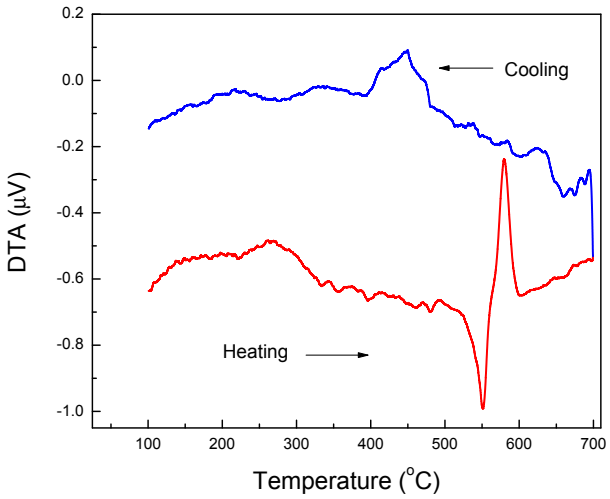

Figure 3.9: DTA curve of $BiAlO_3$ showing endothermic and exothermic peaks at 550 and 580 ^{o}C, respectively. The endothermic peak corresponds to the decomposition of the high-pressure rhombohedral structure while the exothermic peak indicates the formation of γ-Bi_2O_3 structure.

not show any anomaly, suggesting that the process associated with the exothermic peak is irreversible. One can easily miss the endothermic peak unless the DTA curve is recorded slowly. In the earlier study [47] only an irreversible exothermic peak was found around 580 ^{o}C and was attributed to the decomposition of BAO into $Bi_2Al_4O_9$, $Bi_{26-x}Al_xO_{40-\delta}$ and Al_2O_3 phases based on the XRD patterns obtained after heating the sample above 580 ^{o}C. Thermal decomposition is an endothermic process while a phase formation can be exothermic. In order to confirm that the endothermic peak was irreversible, the sample was heated up to 570 ^{o}C and then cooled to room temperature. The XRD patterns of BAO heated at 570 and 600 ^{o}C were characteristic of a mixture of $Bi_2Al_4O_9$, $Bi_{26-x}Al_xO_{40-\delta}$ and Al_2O_3 confirming that both the DTA peaks are irreversible. The material heated to 750 ^{o}C, however, showed only the latter phases, suggesting that the thermodynamically stable phase is the $Bi_{26-x}Al_xO_{40-\delta}$, while $Bi_2Al_4O_9$ may be an intermediate

one. From these results, we suggest the origin of the endothermic peak to be the decomposition of the metastable high pressure rhombohedral phase and the subsequent formation of the intermediate $Bi_2Al_4O_9$. The exothermic peak is associated with the formation of $Bi_{26-x}Al_xO_{40-\delta}$ which has a large number of atoms per unit cell than the orthorhombic $Bi_2Al_4O_9$. It is noteworthy that we do not observe a structural transformation of rhombohedral BAO till it decomposes at 570 ^{o}C, All our measurements have been carried out in air or in an oxygen atmosphere. High temperature XRD data recorded in vacuum (10^{-5} bar) indeed show that there was no structural transformation or decomposition up to 700 ^{o}C (Fig. 3.10).

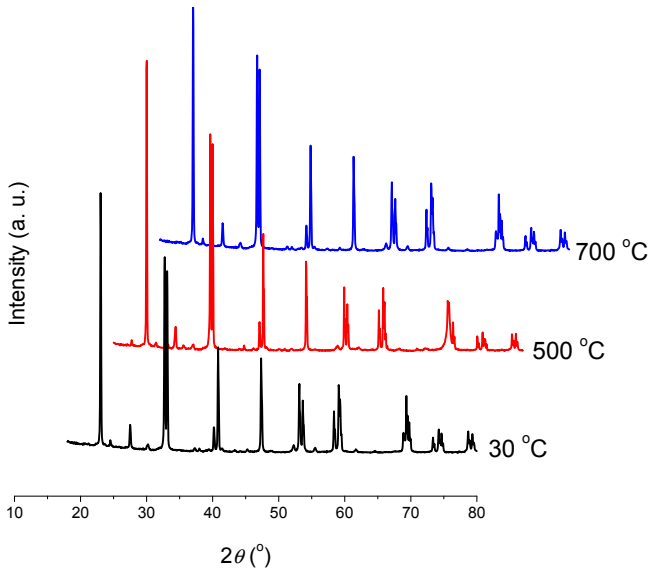

Figure 3.10: X-ray data collected for $BiAlO_3$ at 30, 500 and 700 ^{o}C.

3.3.3 Dielectric studies

Figure 3.11 shows the temperature-dependent real part ($\chi\prime$) of the dielectric response of BAO at various frequencies in the temperature range 27 - 600 ^{o}C. At

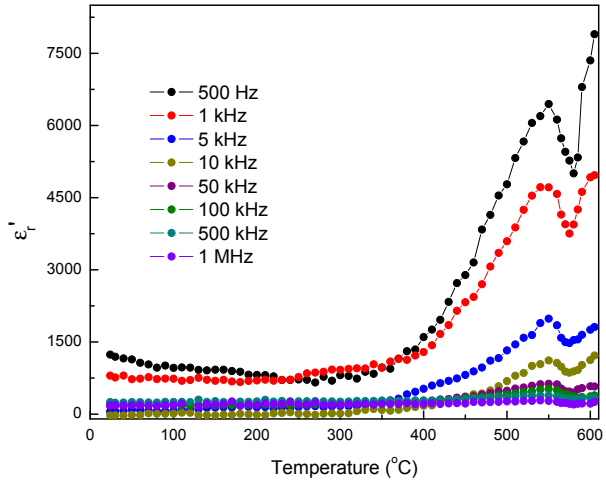

Figure 3.11: Real part of temperature-dependent dielectric constant of $BiAlO_3$ exhibiting a maximum at the decomposition temperature.

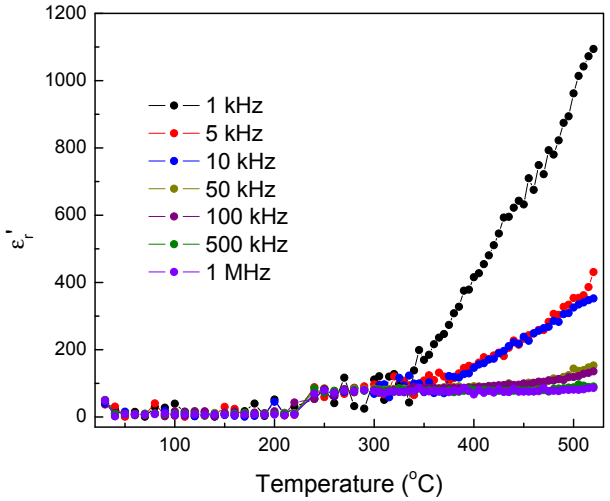

Figure 3.12: Real part of temperature-dependent dielectric constant of $BiGaO_3$.

room temperature BAO shows a dielectric constant value of 180 for a high frequency of 1 MHz. The dielectric constant at low frequencies has a well-defined maximum around 550 ^{o}C and increases further with increase of temperature above 580 ^{o}C. Figures 3.11 and 3.9 suggest that the dielectric maximum corresponds to

the decomposition temperature of the high-pressure rhombohedral phase and not to the high-symmetry phase. Furthermore, the dielectric constant exhibits frequency dispersion over the entire range of temperature employed without any appreciable shift in the dielectric maximum. The increase in the dielectric constant of BAO observed above 570 ^{o}C is due to the increase in DC conduction with increasing temperature. The temperature-dependent dielectric constant for BGO is shown in figure 3.12. The dielectric constant of BGO at room temperature is very low and shows an increase at high temperature due to DC conduction.

3.3.4 Raman studies on $BiAlO_3$

Soft mode behavior can give the insight into the phase transition well above (or below) T_C. Raman and Nedungadi were the first to observe soft modes in the $\alpha-\beta$ transition of quartz which was accompanied by a decrease in the frequency of a totally symmetric optic mode as the temperature approached the phase transition temperature from below [48]. Operationally, a soft mode is a collective excitation whose frequency decreases anomalously as the transition point is reached. While in a second-order transition the soft-mode frequency goes to zero at T_c, in a first-order transition the change of phase occurs before the mode frequency is able to go to zero [48].

In order to understand the behavior of soft-mode phonons and thermal behavior of the high-pressure rhombohedral phase and the subsequent appearance of the ambient pressure phase, we have recorded Raman spectra of BAO at various temperatures. Due to limitations in our instrument, we could record the spectra only up to 520 ^{o}C. BAO, belongs to the point group C_{3v}^{6}, has totally 20 modes, $\Gamma_{Total} = 5A_1 + 5A_2 + 10E$. One A_1 and one E modes are acoustic and 5 A_2 are

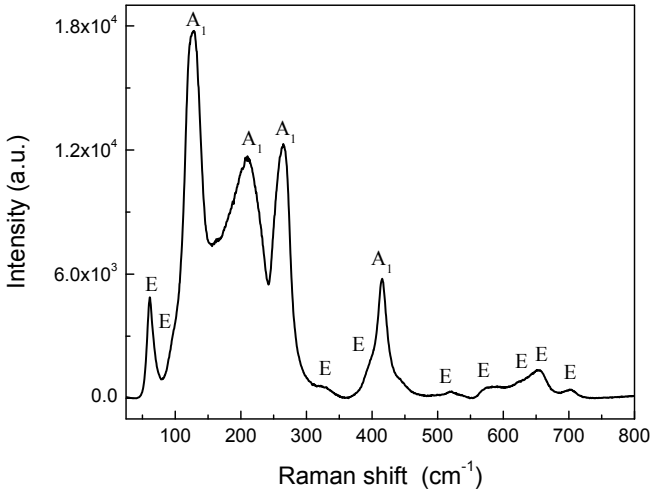

Figure 3.13: Room-temperaute raman spectrum of $BiAlO_3$

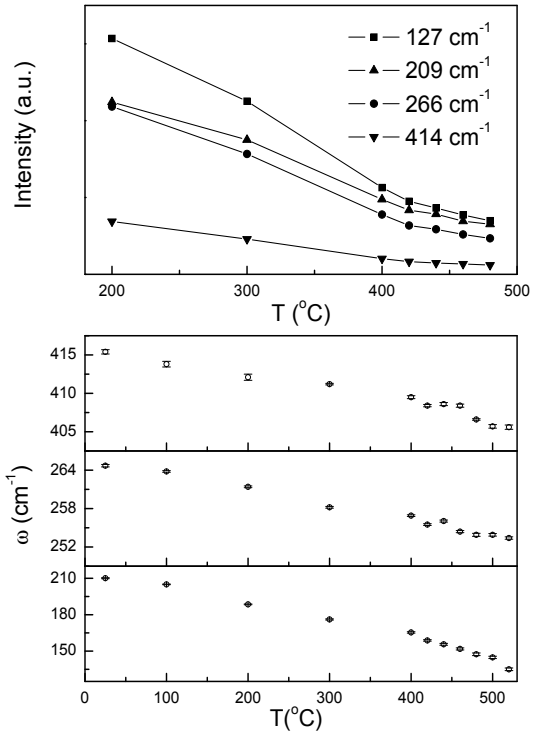

Figure 3.14: Temperature dependence of the frequency and the intensity of various Raman bands in $BiAlO_3$.

Raman and infrared inactive. Hence group theoretical analysis of the perovskite with R*3c* symmetry predicts 13 Raman active modes ($\Gamma = 4A_1 + 9E$). These 13 Raman modes exclude transverse and longitudinal splitting of the A_1 and E modes. We observe all the 13 modes at room temperature (Fig. 3.13) in agreement with spectrum reported in the literature [47]. The modes are assigned on the basis of the Raman studies carried out on $BiFeO_3$ single crystal which has similar structure[49]. With increasing temperature, frequencies of all A_1 modes decrease and the peaks become broader. The temperature dependence of frequency and intensity of some of the Raman modes are shown in figure 3.14. The figure reveals that both the frequency and the intensity of the Raman bands decrease with increasing temperature up to 520 ^{o}C. The room temperature Raman spectrum of a sample heated to 600 ^{o}C showed a completely different Raman spectrum with 22 modes. This finding supports the suggestion that the rhombohedral structure decomposes above 550 ^{o}C.

3.3.5 Polarization - Electric field loop

The polarization-electric field curve of BAO recorded at room temperature on a 200 μm thin sample using Ag electrode is shown in figure 3.15. The shape of the curve is typical of ferroelectric material with a maximum polarization value of 16 μC/cm^2 and remanent polarization (P_r) of 11.5 μC/cm^2. A coercive field of 69 kV/cm was obtained for an applied voltage of 2.25 kV with a frequency of 10 Hz. However the observed polarization value for BAO at room temperature is lower than that predicted (75.6 μC/cm^2) [43] and also calculated using structural data (32 μC/cm^2) [47]. The literature value of polarization reported for bulk $BaTiO_3$ is 26 μC/cm^2 at room temperature which is considerably higher than that observed

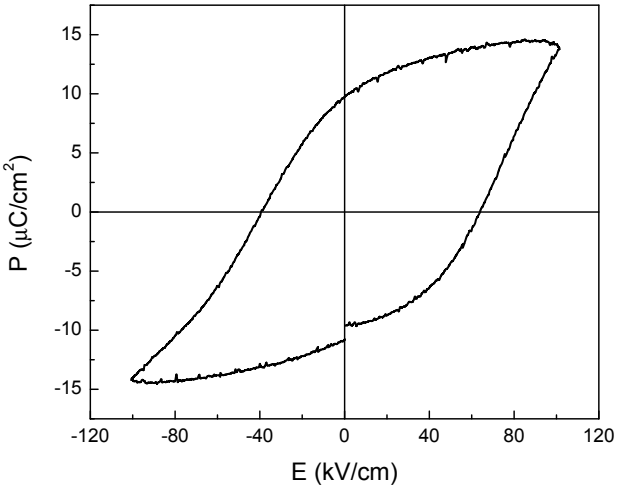

Figure 3.15: Ferroelectric hysteresis of $BiAlO_3$ at room temperature.

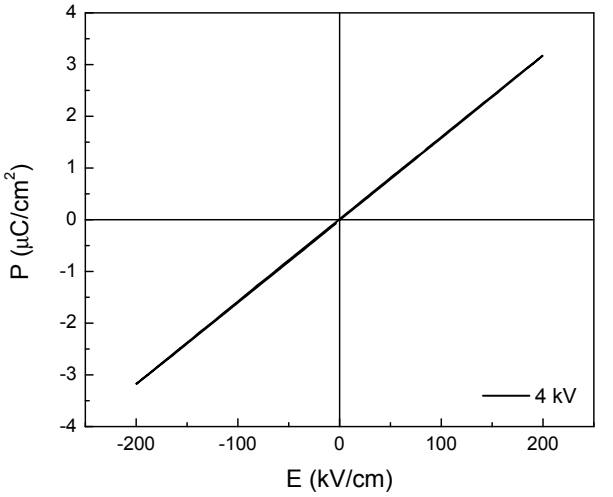

Figure 3.16: Room temperature P-E hysteresis loop of $BiGaO_3$ at various applies drive voltage for the pellets of thickness less than 200 μm.

in the BAO system [50]. The remanent polarization of commercial PZT samples reported by PI Ceramics (PIC 151) is 36 $\mu C/cm^2$ with a coercive field of 9 kV/cm [51]. Figure 3.16 shows the polarization-electric field curve of BGO recorded at room temperature on a 150 μm thin sample using Ag electrode. BGO shows a

linear hysteresis loop indicating that the system is not ferroelectric which is in accordance to the symmetry restriction for a material to be a ferroelectric.

3.4 Conclusions

Initially, high pressure and high temperature synthesis resulted in formation of $BiAlO_3$ phase along with $Bi_2O_2CO_3$ impurity phase due to the presence of $Bi_2O_2CO_3$ in the commercially available bismuth oxide. A heat treatment at 700 ^{o}C converts $Bi_2O_2CO_3$ into Bi_2O_3. $BiAlO_3$ with rhombohedral phase (R$3c$) has been successfully prepared at a pressure 4.5 GPa and 800 ^{o}C by preheating commercial bismuth oxide. $BiAlO_3$ has been prepared at lower pressures and temperatures comparing to literature work which might have been aided by the removal of CO_2 from bismuthoxycarbonate present in bismuth oxide. $BiAlO_3$ undergoes an endothermic transition at 550 ^{o}C due to the decomposition of the metastable high pressure rhombohedral phase and an exothermic transition at 580 ^{o}C due to the formation of $Bi_{26-x}Al_xO_{40-\delta}$ and Al_2O_3. The exothermic peak is accompanied by a dielectric constant maximum. The material is ferroelectric at room-temperature with a maximum polarization of $\sim$ 16 μC/cm^2 and the Raman bands show decrease in frequency and intensity up to 520 ^{o}C. $BiGaO_3$, with orthorhombic structure rather than predicted distorted perovskite structure similar to $PbTiO_3$, shows linear hysteresis in accordance with symmetry restriction for a material to be ferroelectric.

CHAPTER 4

Effect of oxygen non-stoichiometry on structural physical properties of $BiMnO_{3-\delta}$**

4.1 Introduction

Multiferroics constitute a fascinating class of materials of great current interest today [15, 20, 52–55]. From the point of view of classical ferroelectricity, it would appear a contradiction to have a material which is ferroelectric and also ferromagnetic or antiferromagnetic, since the former requires empty d-orbitals while the latter requires d-electrons. Multiferroic properties in most materials are actually attained through novel mechanisms, such as, lone-pair effects, frustrated magnetism, charge-ordering and local noncentrosymmetry [18, 20, 53–56].

Of the various multiferroics reported in recent years, $BiMnO_3$ occupies a special place since it is the only material known to-date which is ferroelectric and ferromagnetic ($T_C \sim 105$ K), the properties believed to arise from the $6s$ lone pair and orbital ordering respectively[17, 57–59]. The reported value of the spontaneous polarization in $BiMnO_3$ is, however, small as also the magnetocapacitance.

$BiMnO_3$ has a highly distorted perovskite-type structure and represents the high-pressure high-density phase in the ternary Bi-Mn-O system. Heating a mixture of bismuth and manganese oxides in the correct ratio at ambient pressure leads

Paper based on this work has been published in *J. Mater. Chem.* **18 (2008) 2191.

to formation $Bi_2Mn_4O_{10}$ and $Bi_{12}MnO_{20}$ phases, whereas at high pressure (> 40 kbar) the formation of the perovskite is favored.

$BiMnO_3$ has been investigated since 1965 mainly for its unexpected ferromagnetic behavior [60]. Contrary to $LaMnO_3$, which undergo A-type antiferromagnetic ordering ($T_N \sim 150$ K) [61], $BiMnO_3$ is a soft ferromagnetic material with a Curie temperature (T_C) around 100 K [62]. In 1999, Atou *et al.* reported that $BiMnO_3$ is related to a heavily distorted perovskite structure with monoclinic symmetry belonging to the space group C*2* using electron diffraction and neutron powder diffraction [63]. The lattice parameters reported for this phase are $a = 9.5323(6)$ Å, $b = 5.6064(3)$ Å, $c = 9.8535(7)$ Å and $\beta = 110.667(5)^o$. Presence of polarized Bi $6s^2$ lone pair was believed to be responsible for the structural distortion. The Jahn-Teller distortion and ordering of a vacant $d_{x^2-y^2}$ orbital of Mn^{3+} has been suggested to play an important role in the ferromagnetic property [63, 64].

Theoretical calculations predicted that $BiMnO_3$ would exhibit ferroelectricity at room temperature which makes it as a multiferroic material [15, 65]. Later, Seshadri *et al.* pointed out the magnetic behavior of $BiMnO_3$ is related to the stereochemical activity of the $6s^2$ lone pair of the bismuth ion that plays a fundamental role in distorting the structure [17]. In 2002, Bismuth manganate shown to have ferroelectricty at low temperature both in thinfilm and bulk [57]. The successful growth of $BiMnO_3$ thin films on strontium titanate (STO) substrate by laser ablation, supplied a further example for the stabilization of a metastable perovskite by "lattice pressure" in the epitaxial growth [66, 67]. Recently, Chi *et al.* showed room temperature ferroelectricity in $BiMnO_3$ ceramic [68]. In 2003, Kimura *et al.* reported that $BiMnO_3$ ceramic shows magnetocapacitance near the ferromagnetic ordering temperature [59]. Further a structural transition from C*2* to P*bnm* symmetry has been reported around 750-770 K which is ascribed to be

the ferroelectric transition (T_E) of the system [59].

In 2005, Montanari *et al.* reported that the metastable bismuth manganate found to have a polymorph at room temperature using electron diffraction and high-resolution electron microscopy [69]. The new polymorph has a triclinic (pseudorhombohedral) superstructure with a = 13.62 Å, b = 13.66 Å, c = 13.66 Å, α = 110.0^o, β = 108.8^o and γ = 108.8^o and mostly segregated at the grain surface. Magnetic susceptibility of this second form shown to have a critical temperature of 107 K, a few degrees above the ferromagnetic transition of the monoclinic C*2* form measured at 99 K. This phase is reported to be a high energy polymorph as it disappearance by reheating the samples at ambient pressure, i.e. kinetically converts to the usual phase once a sufficient temperature has been achieved. It has also been reported that the perovskite $BiMnO_3$, synthesized under high-pressure conditions, decomposes if heated at ambient-pressure in the temperature range of 500-650 ^{o}C. Later Montanari *et al.* [70] suggested a complex pathway to decomposition by the formation of different metastable phases depending on the heating rate, pressure and atmosphere from high-temperature x-ray diffraction, electron diffraction, thermal analysis and magnetic investigation.

Recently selected area electron diffraction (SAED), convergent beam electron diffraction (CBED) and the Rietveld method using neutron diffraction data showed that $BiMnO_3$ crystallizes in the centrosymmetric space group C*2/c* at room temperature [71]. The crystallographic data are a = 9.5415(2) Å, b = 5.61263(8) Å, c = 9.8632(2) Å and β = 110.6584(12)^o. Further, it has been shown to undergo a structural transition to another monoclinic structure (C*2/c*) with low monoclinic angle using neutron diffraction data at 550 K and the lattice parameters reported are a = 9.5866(3) Å, b = 5.59903(15) Å, c = 9.7427(3) Å and β = 108.601(2)^o. By the analysis of Mn-O bond lengths, it has been suggested that the orbital order

present in $BiMnO_3$ at 300 K melts above T_{OO} = 474 K. This first order phase transition at 474 K has been shown to be accompanied by a jump in magnetization and small changes in the effective magnetic moment and Weiss temperature, μ_{eff} = 4.69 μ_B and θ = 138.0 K at 300-450 K and μ_{eff} = 4.79μ_B and θ = 132.6 K at 480-600 K. SAED analysis confirmed that the sample belongs to C-centered due to the absence of (*h0l*) reflection (*h = 2n+1* and *l = 2n+1*) and has the C glide. CBED studies confirmed the presence of mirror symmetry. Theoretical calculations suggested that the ground state of perovskite-structure $BiMnO_3$ is centrosymmetric with space group C*2/c* and zero ferroelectric polarization. However it is pointed out that the calculations are for ideal stoichiometric $BiMnO_3$, which might not always be achieved experimentally [72].

Recently Kodama *et al.* [73], based on atomic pair distribution analysis, have reported that the space group of $BiMnO_3$ is indeed C*2* wherein atomic shifts of P*2* or P2_1 domains break a symmetry of the C-center. Later Yokosawa *et al.* showed the presence of noncentrosymmetric long-range (C*2*) and short-range ordered structures (P*2* or P2_1) using the SAED [74].

One of the problems with $BiMnO_3$ is also that some of the measurements reported in the literature are on samples containing impurity phases [57, 59]. In view of the importance of $BiMnO_3$ as a potential multiferroic material, we have investigating the chemistry of this material in detail. We considered that a possible source of the problem with $BiMnO_3$ could be related to the stoichiometry of the compound since there are certain inherent limitations in controlling the oxygen stoichiometry in the high-pressure synthetic procedure employed for preparing $BiMnO_3$. The purity and oxygen stoichiometry of the starting materials play important roles in deciding the stoichiometry of the final product in such synthesis. It is indeed known that some $Bi_2O_2CO_3$ impurity is always present in $BiMnO_3$ preparations, giving

rise to oxygen deficiency. As it is known that the structure and physical properties of many metal oxides will vary depending on the oxygen stoichiometry, we varied the oxygen content in the bismuth manganate which resulted in identification of a new orthorhombic bismuth manganate phase. This chapter deals with the effect of oxygen non-stoichiometry on the structure and properties of $BiMnO_3$.

4.2 Experimental

$BiMnO_{3-\delta}$ samples were prepared at 850 ^{o}C under a pressure of 4.5 GPa by the reaction of Bi_2O_3 preheated to 700 ^{o}C in oxygen, with an appropriate mixture of MnO and MnO_2, to enable control of the oxygen content. By such a procedure, we have obtained four $BiMnO_{3-\delta}$ phases with different oxygen stoichiometries. The Bi:Mn ratio of these phases was found to be exactly 1:1 by EDAX analysis.

Phase purity of samples was verified with Rigaku and Bruker D8 Discover x-ray diffractometers using Cu K_α radiation. Rietveld refinement was carried out on the x-ray data using Fullprof software [44]. Ferroelectric measurements were carried out on capacitors, prepared by depositing gold on both sides of the pellets using DC sputtering, using Radiant Technologies Precision workstation. Capacitance and dielectric measurements were carried out using Agilent 4294A Impedance analyzer from 100 Hz to 1 MHz in the temperature range of 20 - 360 K. Thermogravimetric analysis (TGA) was carried out on all $BiMnO_{3-\delta}$ samples in a reducing atmosphere (20 % H_2 and 80 % Ar) to determine the oxygen stoichiometry. Rietveld refinements, using Fullprof, were carried out on the neutron diffraction data collected using D2b instrument with a wavelength $\lambda = 1.594$ Å at Institut Laue Langevin (ILL), Grenoble, France. Magnetization measurements were carried out with a vibrating sample magnetometer in Physical Property Measuring System (PPMS,

Quantum Design, USA). Heat capacity was measured by the relaxation method between the temperature interval of 2 K and 120 K under zero applied magnetic field with PPMS. The sample heat capacity was obtained by subtracting out the addenda contribution from the total heat capacity.

4.3 Results and discussion

4.3.1 Oxygen non-stoichiometry in $BiMnO_{3-\delta}$ samples

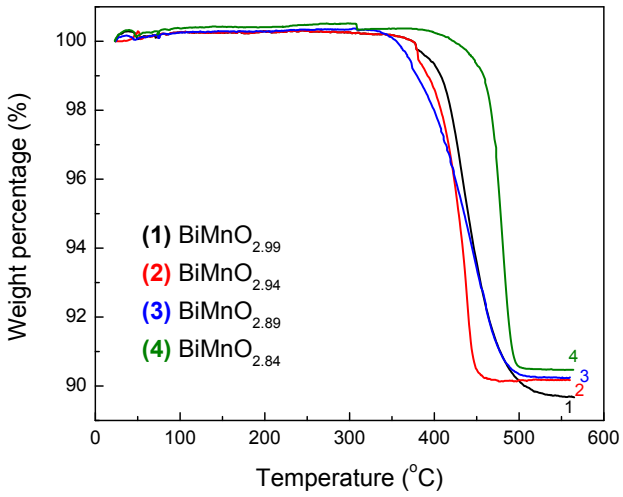

Figure 4.1: Thermogravimetric curves of four $BiMnO_{3-\delta}$ phases in reducing atmosphere.

By employing precision thermogravimetric analysis (TGA) carried out in a hydrogen atmosphere, we have been able to obtain the composition of the four phases, by making use the fact that $BiMnO_3$ gives rise to Bi metal and MnO as final products on decomposition under reducing atmosphere. In figure 4.1, we show TGA curves obtained for the four phases in a reducing atmosphere. The compositions of the four phases obtained by us are $BiMnO_{2.99}$, $BiMnO_{2.94}$, $BiMnO_{2.89}$

and $BiMnO_{2.84}$ with an uncertainty of $\pm$ 0.02. Prior to the analysis of the present system, the reduction of Fe_2O_3 carried out and confirmed the accuracy of the instrument.

4.3.2 Structural analysis

The x-ray diffraction (XRD) patterns of the four compositions are shown in figure 4.2. We see distinct differences between x-ray patterns of $BiMnO_{2.99}$ and $BiMnO_{2.84}$. Further the inset clearly shows the change in $2\theta \sim 32^o$ peak induced by different oxygen stoichiometry in the sample.

$BiMnO_{2.99}$ can be assigned an orthorhombic structure with the lattice dimension ($\sqrt{2}a_p \times 2a_p \times \sqrt{2}a_p$) similar to that of $LaMnO_3$. It is also possible that the $BiMnO_{2.99}$ phase may have a small monoclinic distortion. Figure 4.3 shows the profile matching on x-ray data of orthorhombic $BiMnO_{2.99}$ phase and the refined lattice parameter obtained for this near stoichiometric composition are $a = 5.5182(4)$ Å, $b = 7.8216(8)$ Å and $c = 5.5550(4)$ Å. An orthorhombic phase of $BiMnO_3$ has been reported to occur at high temperatures [75]. Preliminary electron diffraction analysis showed the presence of a Bi-Mn-O phase having an orthorhombic structure with $a = 5.5052(5)$ Å, $b = 11.0997(5)$ Å and $c = 15.486(1)$ Å cell parameters. However the Rietveld refinement using the neutron data for the sample $BiMnO_{2.99}$ gave a large isothermal parameter(Table 4.1) even though both the orthorhombic phases were included in the refinement.

The high oxygen-deficient composition, $BiMnO_{2.84}$, has a monoclinic structure. The profile matching on x-ray data of $BiMnO_{2.84}$ phase is shown in figure 4.5. The cell parameters obtained for this phase are $a = 9.5272(9)$ Å, $b = 5.6048(6)$ Å, $c = 9.8391(9)$ Å and $\beta = 110.439(5)^o$ fitted with space group C*2/c*. Rietveld

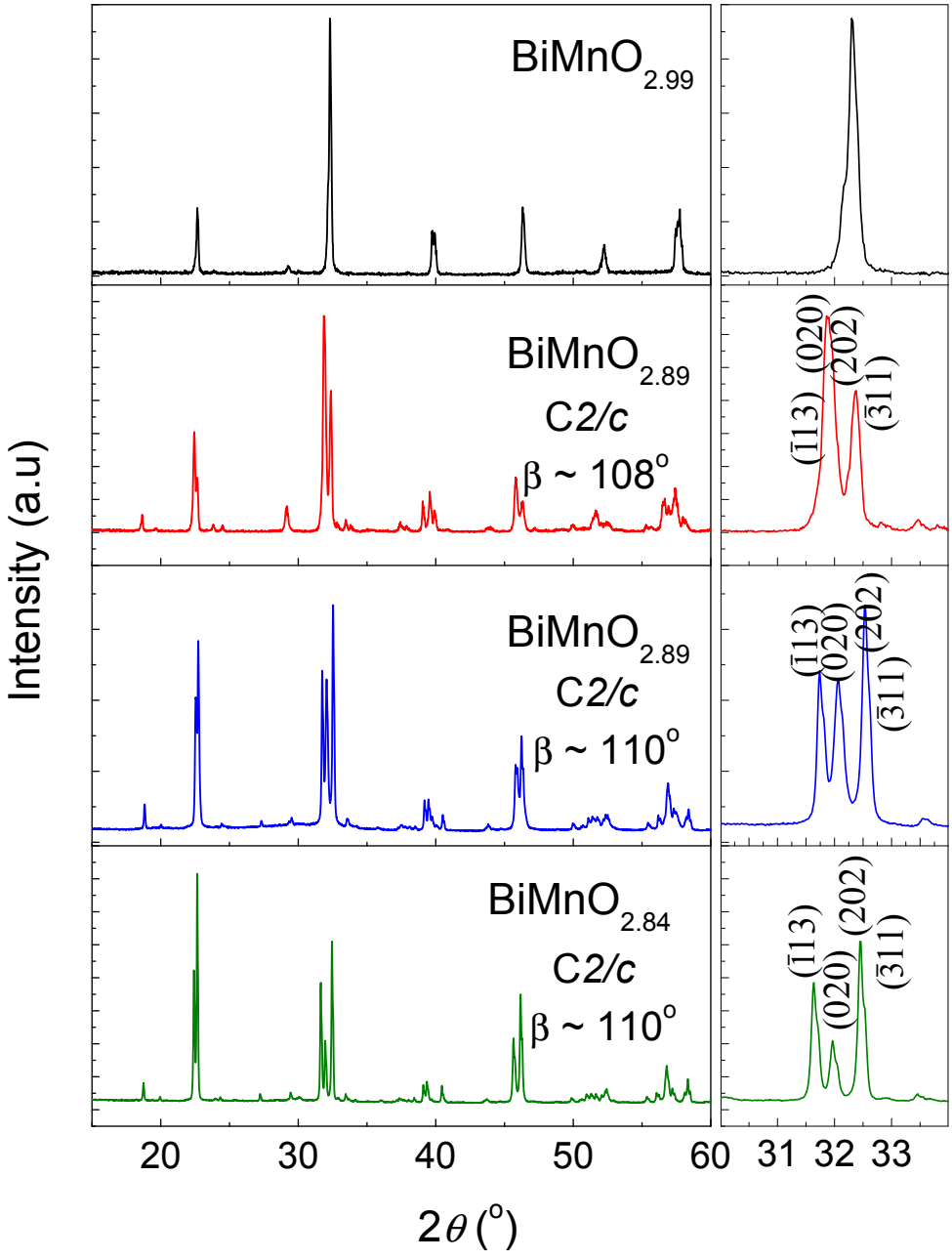

Figure 4.2: X-ray pattern of four $BiMnO_{3-\delta}$ phases and the peak corresponding to $2\theta = 32^o$.

refinement on neutron data of this sample also gave large isothermal parameters (Table 4.2) and the fit is shown in figure 4.6. The XRD patterns of $BiMnO_{2.94}$

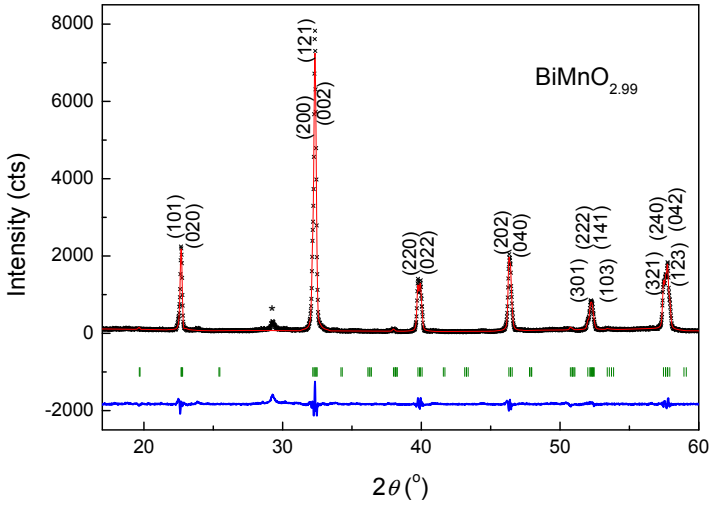

Figure 4.3: Profile matching of x-ray powder diffraction pattern of $BiMnO_{2.99}$ phase using $\sqrt{2}a_p \times 2a_p \times \sqrt{2}a_p$ parameters. *Unknown peak

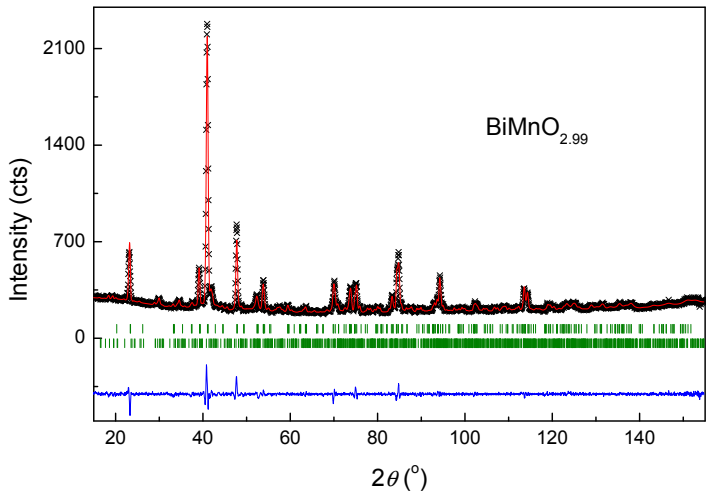

Figure 4.4: Rietveld refinement on powder neutron diffraction data of $BiMnO_{2.99}$, collected at room temperature using D2b instrument with $\lambda = 1.594$ Å at the Institut Laue Langevin (ILL), Grenoble, France. Vertical tick marks are symmetry-allowed reflections. First row belongs to the phase with Pnma space group and the second row corresponds to the phase with P$n2_1m$.

Table 4.1: Structural parameters for $BiMnO_{2.99}$ obtained from Rietveld refinement with the room-temperature neutron diffraction data collected with $\lambda = 1.594$ Å. *Fixed parameters

P*nma*					
$a = 5.5702(5)$ Å $b = 7.8762(7)$ Å and $c = 5.5360(2)$ Å					
Atoms	x	y	z	B	Occupancy
Bi	-0.010(5)	0.25	0.026(2)	7.4(2)	1*
Mn	0	0	0	5.3(1)	1*
O	0.495(6)	0.25(2)	0.006(4)	6.8(3)	1.10(3)
O	0.267(1)	0.0366(6)	0.761(2)	4.4(1)	1.90(3)
$R_{Bragg} = 6.18$ % and $\chi^2 = 3.52$					

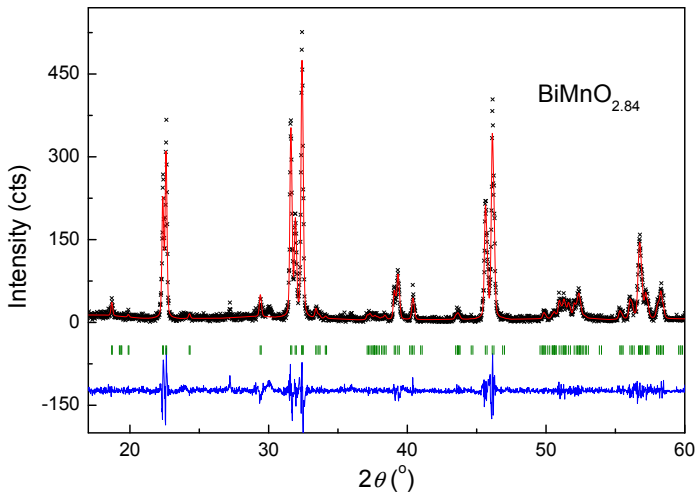

Figure 4.5: Profile matching of x-ray powder diffraction pattern of $BiMnO_{2.84}$ phase.

and $BiMnO_{2.89}$ also correspond to a monoclinic structure. All the three monoclinic structures can be assigned to the C*2/c* space group, although we cannot entirely rule out C*2* space group. The XRD patterns of $BiMnO_{2.89}$ and $BiMnO_{2.84}$ are similar. Figure 4.7 shows the profile matching on x-ray data of $BiMnO_{2.94}$ phase. The refined lattice parameter obtained are $a = 9.545(1)$ Å, $b = 5.5925(6)$ Å, c

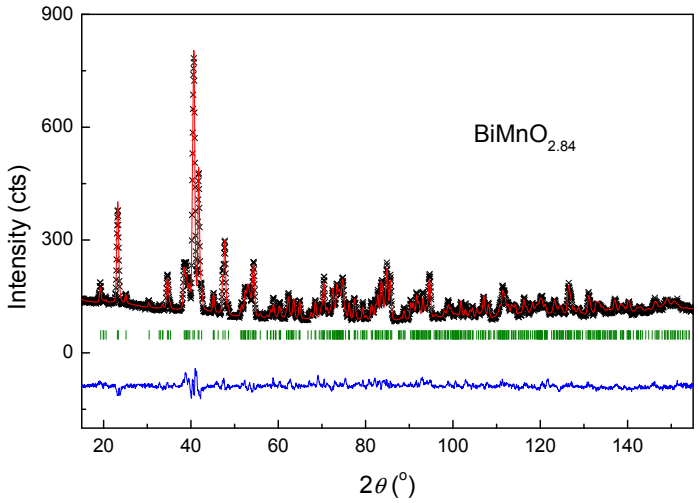

Figure 4.6: Rietveld refinement on powder neutron diffraction data of $BiMnO_{2.84}$, collected at room temperature using D2b instrument with $\lambda = 1.594$ Å at the Institut Laue Langevin (ILL), Grenoble, France.

Table 4.2: Structural parameters for $BiMnO_{2.84}$ obtained from Rietveld refinement with the room-temperature neutron diffraction data collected with $\lambda = 1.594$ Å. *Fixed parameters

C2/c					
$a = 9.5229(5)$ Å $b = 5.5998(3)$ Å $c = 9.8316(5)$ Å and $\beta = 110.363(3)^o$					
Atoms	x	y	z	B	Occupancy
Bi	0.1357(4)	0.2218(5)	0.1286(4)	1.60(5)	2*
Mn	0	0.213(2)	0.75	1.3(2)	1*
Mn	0.25	0.25	0.5	0.9(2)	1*
O	0.0948(5)	0.1798(8)	0.5800(5)	1.53(8)	2*
O	0.1444(5)	0.5617(7)	0.3669(7)	1.69(8)	2*
O	0.3569(5)	0.5425(8)	0.1644(5)	1.45(7)	2*
$R_{Bragg} = 12.4$ % and $\chi^2 = 7.62$					

= 9.740(1) Å and $\beta = 108.892(5)^o$ and the obtained lattice parameter are similar to the high temperature monoclinic phase reported in literature [71]. The x-ray pattern of $BiMnO_{2.94}$ shows the possible presence of the monoclinic phase with

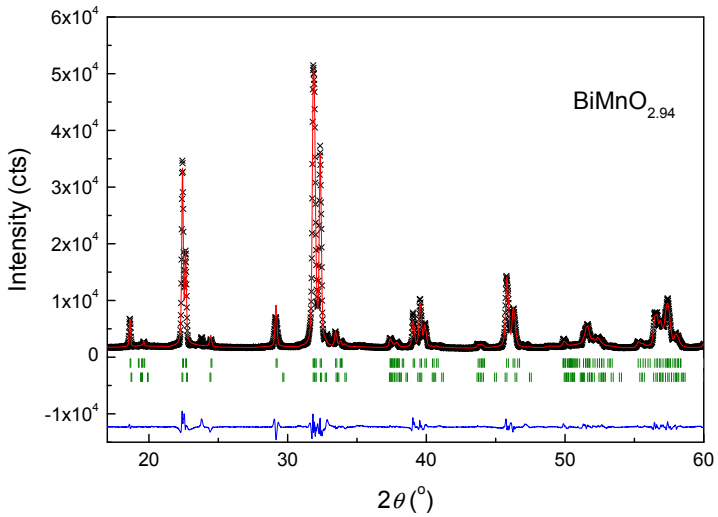

Figure 4.7: Profile matching of x-ray powder diffraction pattern of $BiMnO_{2.94}$ phase.

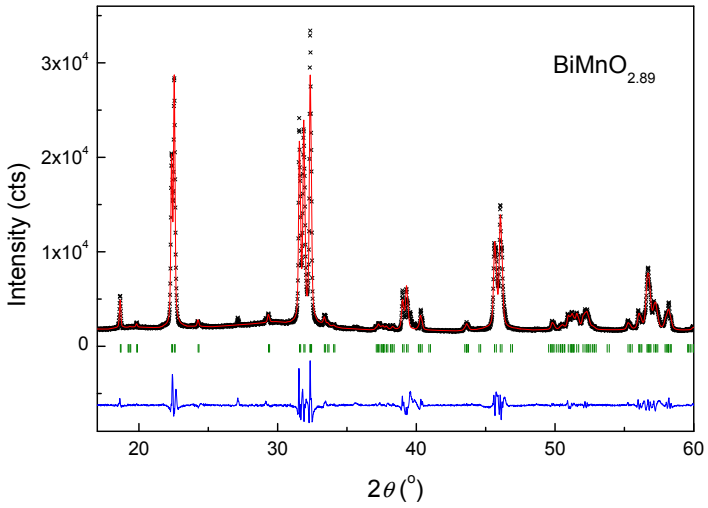

Figure 4.8: Profile matching of x-ray powder diffraction pattern of $BiMnO_{2.89}$ phase.

$\beta \sim 110^o$ as an impurity. This may be due to the presence of various phases with different oxygen stoichiometry. Figure 4.8 shows the profile matching on x-ray data of $BiMnO_{2.89}$ phase and the refined lattice parameters obtained are $a =$

9.5487(6) Å, b = 5.6132(4) Å, c = 9.8462(5) Å and β = 110.287(3)^o. The only significant difference in the structures of these oxygen-deficient monoclinic phases is in the monoclinic angle. Bellik *et al.* [71] have reported the occurrence of two monoclinic phases of $BiMnO_3$ as a function of temperature. What we find in the present study are four room-temperature $BiMnO_3$ phases, differing in oxygen stoichiometry, obtained by high-pressure synthesis.

4.3.3 Magnetic properties

The temperature variation of magnetic susceptibility of the four compositions are shown in figure 4.9. Orthorhombic $BiMnO_{2.99}$ is a canted antiferromagnet (T_N = 30 K). There is no heat capacity anomaly at T_N (Fig. 4.10), but magnetic hysteresis is observed at 5 K with a magnetization value of 2.13 μ_B/Mn at 5 T. Further, the temperature dependent zero field susceptibility at various field shows that the T_N peak disappears at higher field (Fig. 4.11). The magnetic structure of the orthorhombic $BiMnO_{2.99}$ appears to be similar to that of $LaMnO_3$ where the canted antiferromagnetism or weak ferromagnetism is attributed to Dzyaloshinskii-Moriya interaction [76].

The oxygen-deficient monoclinic $BiMnO_{2.84}$ shows a sharp ferromagnetic transition with a T_C value of $\sim$ 105 K and a magnetization value of 2.59 μ_B/Mn at 5 T. The values of the coercive field in $BiMnO_{2.99}$ and $BiMnO_{2.84}$ are 800 Oe and 80 Oe, respectively. $BiMnO_{2.94}$ and $BiMnO_{2.89}$ also show ferromagnetic transitions similar to $BiMnO_{2.84}$ (Fig. 4.9), with a distinct shoulder in the susceptibility curve around 85 K. The effective paramagnetic moment of $BiMnO_{2.99}$ is 4.55 μ_B, close to the spin-only value of 4.90 for Mn^{3+} (Table 4.3). Table 4.3 shows the observed and calculated μ_{eff}, θ_P and magnetization(M) value observed at a mag-

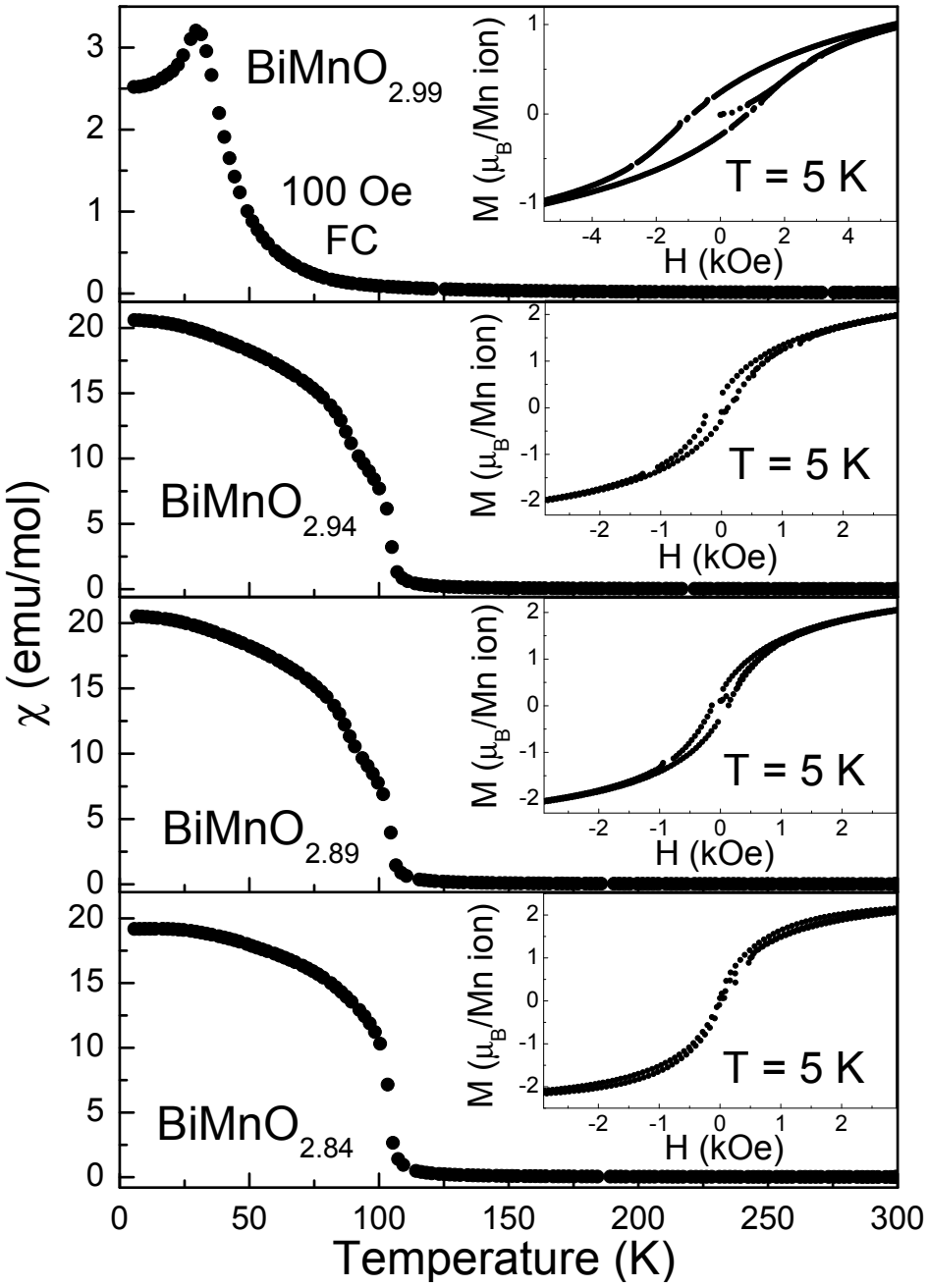

Figure 4.9: Temperature dependent field cooled (FC) susceptibility of four $BiMnO_{3-\delta}$ phases. Magnetic hysteresis curves are shown as insets.

netic field of 7 T for four $BiMnO_{3-\delta}$ phases. With increasing oxygen deficiency, the magnetic moment increases with values of 5.29, 5.30 and 5.4 μ_B respectively

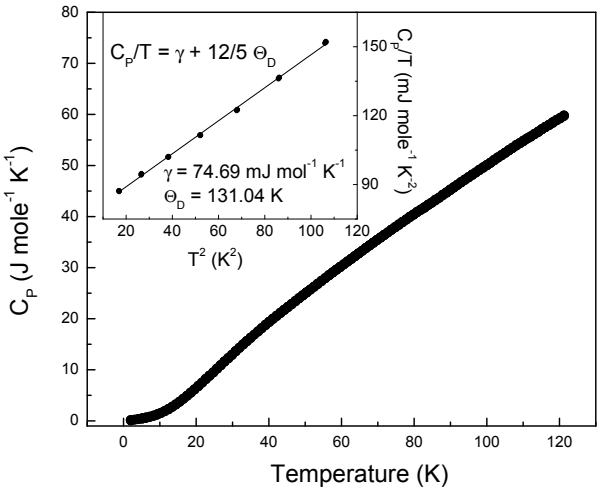

Figure 4.10: Heat capacity versus temperature plot of $BiMnO_{2.99}$.

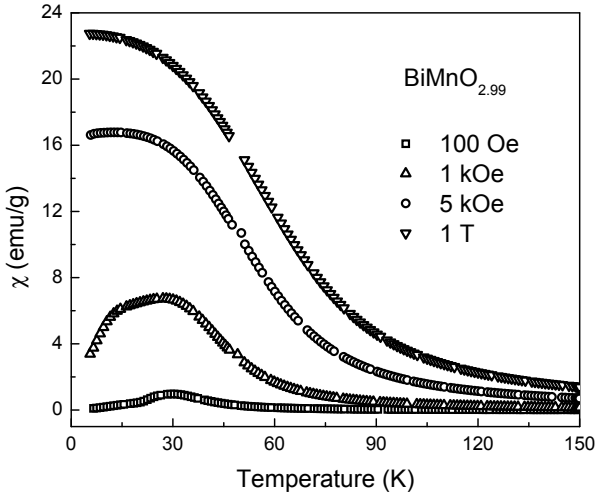

Figure 4.11: Temperature dependent Zero field (ZFC) susceptibility of $BiMnO_{2.99}$ for different magnetic field.

for $BiMnO_{2.94}$, $BiMnO_{2.89}$ and $BiMnO_{2.84}$. This is consistent with the presence of Mn^{3+} (d^4) and Mn^{2+} (d^5) ions which can give rise to ferromagnetism according to the Goodenough-Kanamori rules [4, 6, 7]. While $BiMnO_{2.99}$ and $BiMnO_{2.84}$ seems to be clearly monophasic, $BiMnO_{2.94}$ and $BiMnO_{2.89}$ may contain domains of two

magnetic phases as suggested by the shoulder in the magnetic susceptibility data in the ferromagnetic transition regime. The two domains could indeed have the space groups C*2* and C*2/c*. Preliminary electron diffraction studies show the presence of phases belonging to both the C*2* and C*2/c* space groups in these phases. Considering the XRD and magnetic data of the different phases, it appears that the actual composition of the bismuth manganate reported in the literature could be associated with some oxygen non-stoichiometry.

Table 4.3: Observed and calculated μ_{eff}, θ_P and M at H = 7 T for four $BiMnO_{3-\delta}$ phases

$BiMnO_{3-\delta}$	Observed μ_{eff} (μ_B)	Calculated μ_{eff} (μ_B)	θ_P (K)	M at H = 7 T (μ_B/Mn)
$BiMnO_{2.99}$	4.55	4.92	77.99	2.32
$BiMnO_{2.94}$	5.29	5.01	111.96	3.07
$BiMnO_{2.89}$	5.30	5.12	109.67	3.15
$BiMnO_{2.84}$	5.40	5.22	111.45	2.60

4.3.4 Dielectric studies

Figure 4.12 shows the temperature dependant dielectric constant of the four BiMn $O_{3-\delta}$ phases. BiMn $O_{2.99}$ shows a dielectric anomaly at 300 K, the dielectric constant reaching a value of $\sim$ 106 at 100 Hz near the maxima. $BiMnO_{2.89}$ shows a dielectric anomaly at 340 K, the dielectric constant at the maxima reaching $\sim$ 105 at 100 Hz. We also see a dielectric anomaly in $BiMnO_{2.94}$ around 320 K, with a dielectric constant of $\sim$ 104 (100 Hz) near maxima. In contrast to other phases, $BiMnO_{2.84}$ phase shows dielectric anomaly around 250 K and the increase of dielectric constant above 300 K can be attributed to dc conduction. It is important to mention here that the differential scanning calorimeter analysis of $BiMnO_{2.99}$

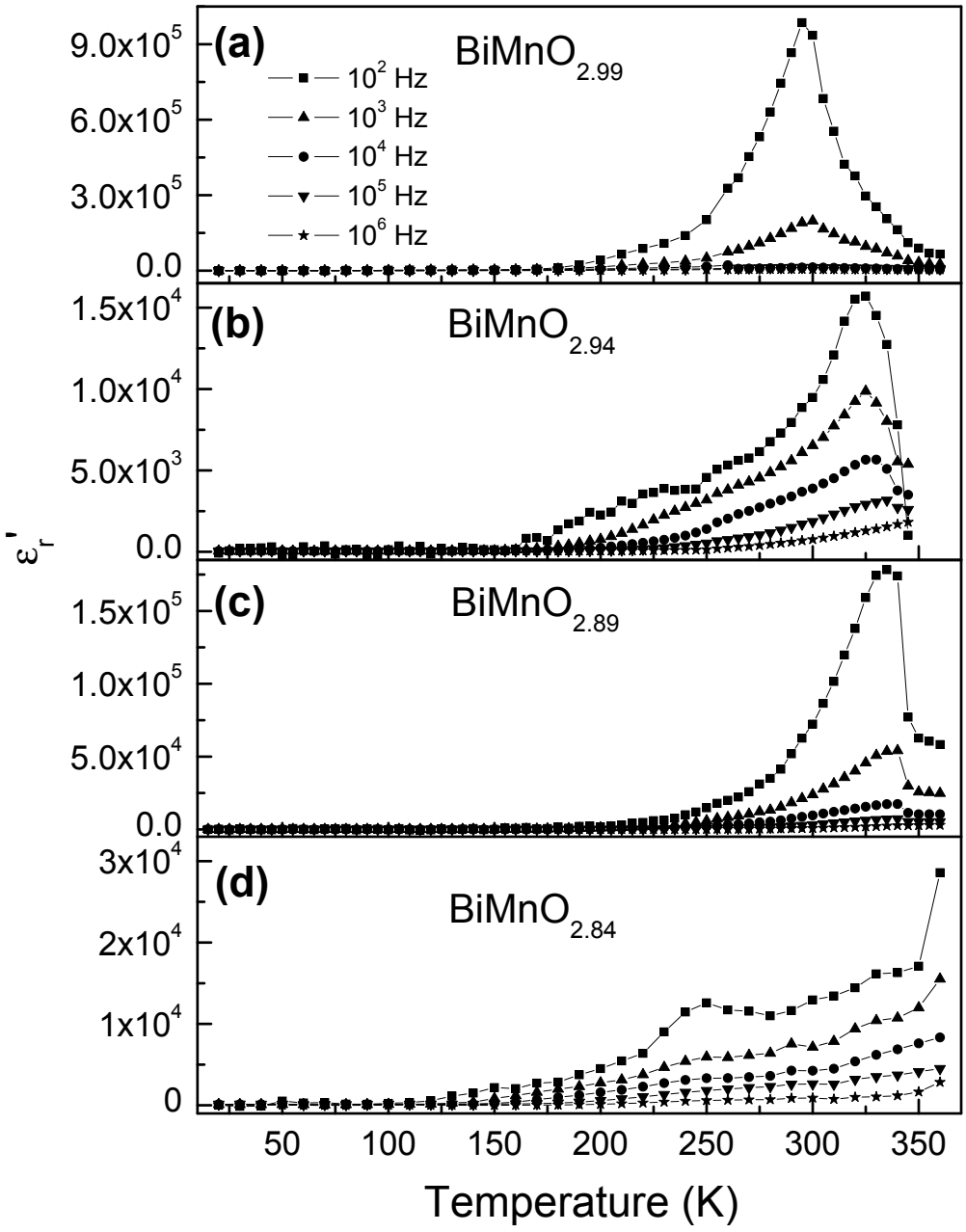

Figure 4.12: Temperature dependent dielectric constant (real part) of four $BiMnO_{3-\delta}$ phases as a function of frequency.

shows a kinetically irreversible transition (Fig. 4.13) just above room temperature. This may associate with transformation of triclinic structure to monoclinic

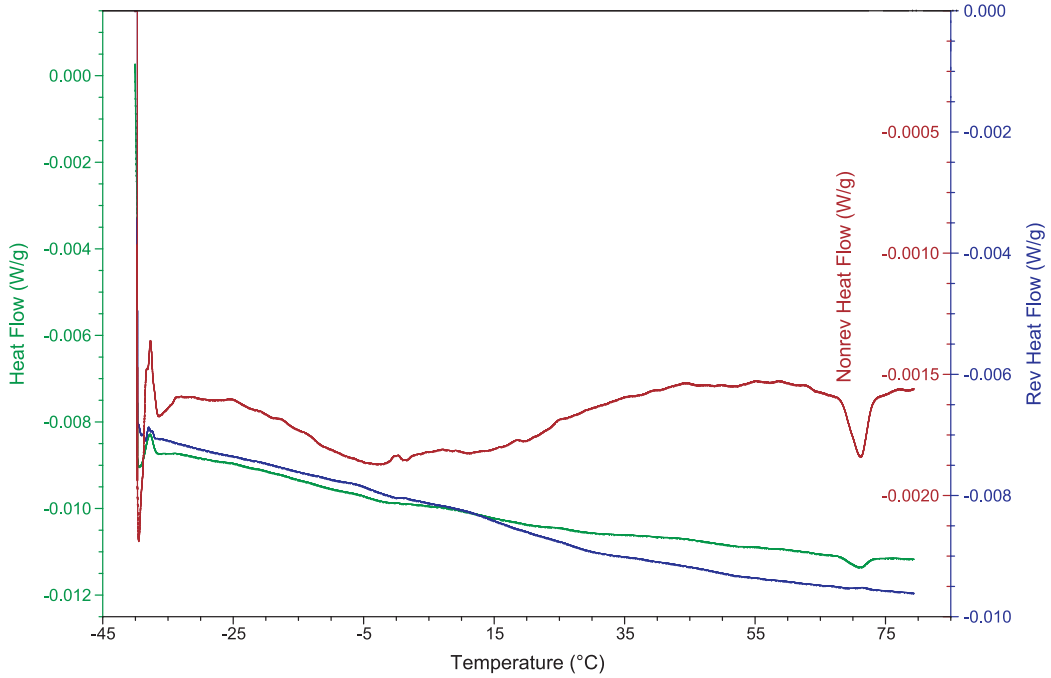

Figure 4.13: Differential scanning calorimeter curve of $BiMnO_{2.99}$ phase.

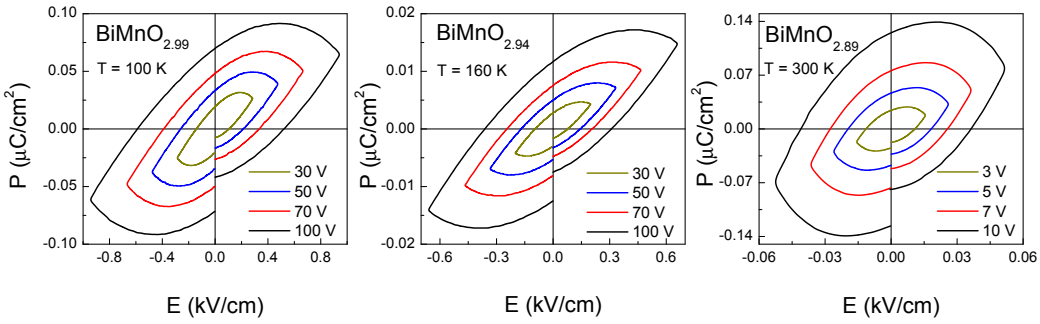

Figure 4.14: Polarization-electric field loop of $BiMnO_{2.99}$, $BiMnO_{2.94}$ and $BiMnO_{2.89}$.

as reported in literature [69]. Due to the leakage behavior, the samples show linear lossy polarization-electric field loop (Fig. 4.14). At this stage we cannot entirely be sure that ferroelectricity or the multiferroic nature of $BiMnO_{3-\delta}$ phases as the ferroelectric hysteresis measurements at high electric field in low temperatures are

not possible due to our instrumental limitations.

4.4 Conclusions

$BiMnO_3$ is an interesting material where changes in oxygen stoichiometry give rise to phases with different structures and magnetic properties. We identified a new bismuth manganate phase with near stoichiometric composition, $BiMnO_{2.99}$. Of the four phases prepared by us, the near-stoichiometry $BiMnO_{2.99}$ as well as the oxygen-deficient $BiMnO_{2.84}$ are monophasic with distinctive structures and magnetic properties, the former being orthorhombic and the latter monoclinic. $BiMnO_{2.99}$ exhibits canted antiferromagnetism while $BiMnO_{2.84}$ exhibits ferromagnetism. $BiMnO_{2.94}$ and $BiMnO_{2.89}$ are also monoclinic and ferromagnetic, but could contain domains of two closely related phases, possibly differing in oxygen stoichiometry. Thus, the present study brings out how the properties of $BiMnO_3$ are more complex than originally believed and that oxygen stoichiometry is likely to play a crucial role in determining the structures and magnetic properties.

CHAPTER 5

Multiferroic Properties of Nanocrystalline $BaTiO_3$**

5.1 Introduction

Ferroelectic materials exhibit spontaneous electric polarization that can be switched to its symmetry equivalent states with applied electric field. Ferroelectric ABO_3 perovskites are not only of fundamental interest but also of technological importance due to the strong coupling of their polarization with electric and stress fields. Switchability of the direction of polarization with applied electric field makes them useful in making non-volatile memories while their sensitivity to stress and strain fields is responsible for their use in micro-electromechanical systems. It will greatly widen the range of their applications, if the polarization is coupled with magnetic field as well. Such magnetoelectric coupling is a fundamentally interesting property allowed by the symmetry of multiferroic materials that exhibit ferroelectricity and ferromagnetism under the same physical conditions.

Ferroelectricity in $BaTiO_3$ (BTO) arises from the off-centering of the Ti ions with respect to a centrosymmetric cubic perovskite crystal. The fact that off-centering of the B-cation (eg. Ti^{4+}) originates from its d^0 electronic state [15], contraindicates the possibility of magnetism that arises from local magnetic mo-

Paper based on this work has been published in *Solid state commun.* **149 (2009) 1; Another manuscript based on this work is under preparation

ments associated with the occupation of the d-states at the B-site. Thus Multiferroics [10] form a rare class of materials that exhibit magnetoelectric coupling arising from the coexistence of ferromagnetism and ferroelectricity, with potential for many technological applications [77, 78].

Over the last decade, an active research on multiferroics has resulted in the identification of a few routes that lead to multiferroicity in bulk materials [14, 18, 79]. In perovskite materials such as $BiMnO_3$ [57, 65] and $BiFeO_3$ [12, 16] ferroelectricity arises from the stereochemically active $6s$ lone-pair of Bi^{3+} ions, and the magnetism originates from interacting spins of the d-electrons of Mn^{3+} or Fe^{3+} ions. In manganates, such as $YMnO_3$, ferroelectricity is related to the geometry of its structure. While a superposition of two distinct types of charge ordering was shown to yield broken centrosymmetry and ferroelectricity in CMR materials [18, 80] spin cycloids [81], were found to be the source of polarization in $TbMnO_3$ [14, 59].

It is known that ferroelectricity is suppressed at the nano-scale due to depolarization fields arising from the bound charges at the surface. For example, ferroelectricity in BTO nanoparticles disappears below a critical size (40 nm) [82, 83]. On the other hand, recent work has shown that ferromagnetism occurs in nanoparticles of the otherwise nonmagnetic oxides [84], but decreases with increasing particle size. Magnetism in these nanoparticles, considered to arise from vacancies at the surface, is suggested to be a universal phenomenon. A recent finding of ferroelectricity in much smaller (12 nm) nanoparticles of BTO [85] motivated us to explore the simultaneous occurrence of ferromagnetism and ferroelectricity in BTO nanocrystalline sample where the former is expected to arise from the surface and the latter from the core. Here, we use a combination of experiment and first-principles simulations to demonstrate that multiferroic nature emerges in in-

termediate size nanocrystalline $BaTiO_3$, ferromagnetism arising from the oxygen vacancies at the surface and ferroelectricity from the core. A strong coupling between a surface polar phonon and spin is shown to result in a magnetocapacitance effect observed at room temperature, which can open up possibilities of new electro-magneto-mechanical devices at the nano-scale. As the source of ferromagnetism is believed to be due to surface defects, positron annihilation spectroscopy (PAS) has been employed to characterize these defects

5.2 Experimental

Nanocrystalline BTO sample was prepared by polymer precursor method using $BaCO_3$ and titanium (IV) isopropoxide as starting materials [86, 87]. Stoichiometric quantity of titanium (IV) isopropoxide was added to a mixture of ethanol and acetic acid (3:1 volume ratio) and stirred continuously. After two hours, barium citrate solution, prepared with required amount of citric acid and $BaCO_3$, was added. Polyvinyl alcohol solution was finally added to the mixture and followed by continuous stirring until the formation of a white sol. The sol was centrifuged and dried at room temperature. Thermogravimetric analysis of the as-prepared sample showed that the decomposition of organic components occurs around 500 ^oC. In order to completely remove the organic part, the sample was heated at 700 ^oC in oxygen. For characterization of ferroelectricity through measurement of P-E hysteresis loop, a dense nanocrystalline BTO sample was prepared by pressing the (40 nm) particles into pellets and heating at 1000 ^oC for 1 hr. This step yields a dense nanocrystalline BTO that facilitates the measurement of ferroelectric hysteresis loop. Rietveld refinement was carried out using Fullprof software [44] on the x-ray data collected with Bruker D8 Discover x-ray diffractometers. Magnetization

measurements were carried out with a vibrating sample magnetometer in Physical Property Measuring System (Quantum Design, USA). Capacitors were prepared by depositing gold on both sides of the pellets using DC sputtering. Ferroelectric measurements were carried out using Radiant Technologies Precision workstation. Capacitance and dielectric measurements with and without magnetic field were carried out using Agilent 4294A Impedance analyzer from 100 Hz to 1 MHz in the temperature range of 20 - 380 K attached to a close-cycle cryocooled Nb_3Sn superconducting magnet.

Positron annihilation studies were carried out on BTO samples of size 60 nm, 100 nm and 2 μm prepared by heat treatment at 700 ^{o}C, 1000 ^{o}C and 1200 ^{o}C respectively. For positron annihilation studies a 10 μCi ^{22}Na source of positrons (enclosed between 2 μm thin nickel foils) has been sandwiched between two identical and plane faced pellets [88–90]. The positron annihilation lifetimes have been measured with a fast-slow coincidence assembly. The detectors are 25-mm-diam $\times$ 25-mm-long cylindrical BaF_2 scintillators optically coupled to Philips XP2020Q photomultiplier tubes. The resolving time (full width at half maximum $\sim$ FWHM) measured with a ^{60}Co source and with the windows of the slow channels of the fast-slow coincidence assembly set to select pulses corresponding to 300 keV to 550 keV in one channel and 700 keV to 1320 keV in the other, is 250 ps. For each positron annihilation lifetime spectrum about 10^6 coincidence counts have been recorded. Measured positron annihilation lifetime spectra have been analyzed by computer programme PATFIT-88 [91] with necessary source corrections to evaluate the possible lifetime components τ_i, and their corresponding intensities I_i. For the coincidence Doppler broadening of annihilation γ-radiation (CDBAR) measurement, two identical HPGe detectors (Efficiency : 12 % ; Type : PGC 1216sp of DSG, Germany) having energy resolution of 1.1 keV at 514 keV of ^{85}Sr have been

used as two 511 keV γ- ray detectors. The CDBAR spectrum have been recorded in a dual ADC based - multiparameter data acquisition system (MPA-3 of FAST ComTec, Germany). The peak to background ratio of this CDBAR measurement system, with $\pm$ ΔE selection, is $\sim 10^5$:1 [92, 93]. CDBAR spectra have been also analyzed by constructing the ratio curve [93–96].

5.3 Results and discussion

5.3.1 Morphology and structure

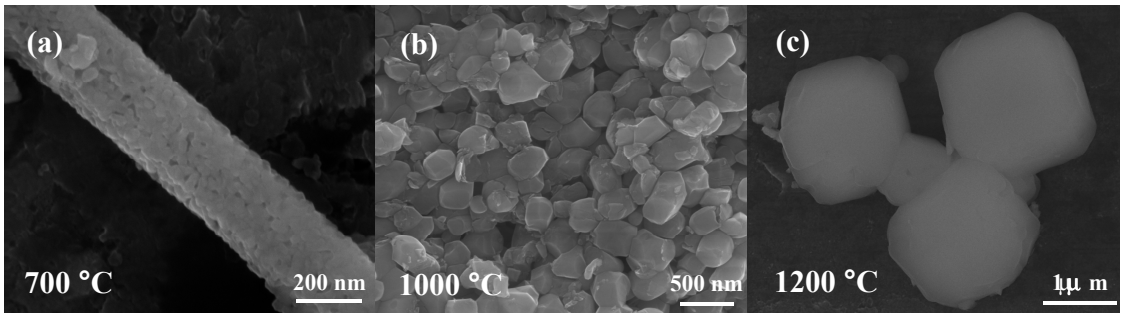

Figure 5.1: FESEM image of the BTO sample heated to (a) 700 ^{o}C (40 nm) (b) 1000 ^{o}C (300 nm) and (c) bulk BTO sample obtained by sintering the nanoparticles at 1200 ^{o}C.

FESEM image of samples heated at 700 ^{o}C and 1000 ^{o}C show rods containing assemblies of nanoparticles with an average diameter - 40 nm (Fig. 5.1a) and a dense nanocrystalline BTO sample (Fig. 5.1b) with an average diameter of about 300 nm respectively. The FESEM image of the bulk BTO sample (Fig. 5.1c), obtained by sintering the pressed nanoparticles at 1200 ^{o}C, shows the grain size to be around $\sim 2\mu$m. Room-temperature x-ray diffraction pattern of all the three samples showed the tetragonal (P$4mm$) structure, with the lattice parameters, a = 4.0047(2) Å and c = 4.0226(4) Å, a = 3.9968(1) Å and c = 4.0298(1) Å and a

= 3.9951(1) Å and c = 4.0377(1) Å, respectively (Table 5.1). The increase in c/a ratio with particle size is consistent with increasing tetragonality and magnitude of off-center distortion of Ti-ions from their cubic symmetry [97].

Table 5.1: Cell parameters and Ti-O bond lengths for $BaTiO_3$ sample heated at different temperature.

P*4mm*			
Parameter	700 ^{o}(40 nm)	1000 ^{o}C (300 nm)	1200 ^{o}C (2 μm)
a (Å)	4.0071(1)	3.9980(2)	3.9951(1)
c (Å)	4.0273(2)	4.0311(2)	4.0377(1)
Ti-O(1) (Å)	2.02(6)	2.08(8)	2.12(8)
Ti-O(1) (Å)	2.01(6)	1.95(8)	1.92(8)
4 × Ti-O(2) (Å)	2.005(2)	2.003(2)	1.998(4)

5.3.2 Magnetism

Measurement of magnetization in the BTO particles heated at 700 and 1000 ^{o}C clearly show ferromagnetism at room temperature (Fig. 5.2a and 5.2b). The coercivity increases from 95 to 435 Oe with increase in particle size from 40 to 300 nm, which may be due to change in the distribution of defects at the surface and shape anisotropy. On the other hand, the saturation magnetization reduces from 0.0025 to 0.0012 emu/gm with increasing particle size and finally the bulk BTO sample failed to exhibit magnetic hysteresis as expected of a bulk BTO. It exhibits diamagnetic behavior at room temperature as shown in Fig 5.2c. Since there are no magnetic elements involved in the preparation of BTO nanoparticles and there was no contamination of magnetic materials during the process of magnetization measurements, the ferromagnetism is intrinsic to the nanocrystalline BTO. The observed ferromagnetism is consistent with the suggestion that nanoparticles of

the otherwise non-magnetic oxides are ferromagnetic [84]. The origin of ferromagnetism may lie in the magnetic moments arising from the oxygen vacancies on the surfaces of the nanoparticles as suggested earlier [84]. It is, therefore, understandable that an increase in the particle size caused by sintering eliminates the magnetism due to the decrease in the surface to volume ratio. In fact, it has been shown theoretically that point defects such as cation or anion vacancies in insulators can create magnetic moments [98, 99]. Further, it was shown that the range of exchange interaction between the magnetic moments and the critical concentration of vacancy determine the magnetic ground state of a material, for example HfO_2, where neutral Hf vacancies induce magnetic moments on neighboring oxygens [100].

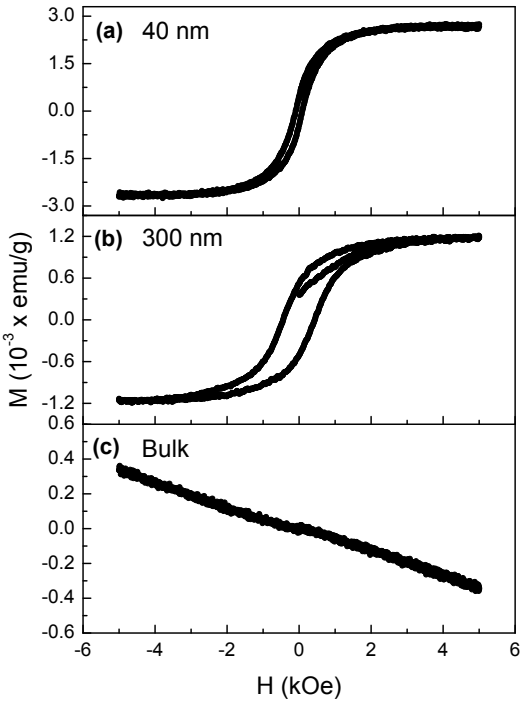

Figure 5.2: Room-temperature magnetic hysteresis of (a) 40 nm, (b) 300 nm and (c) bulk BTO.

5.3.3 Ferroelectricity

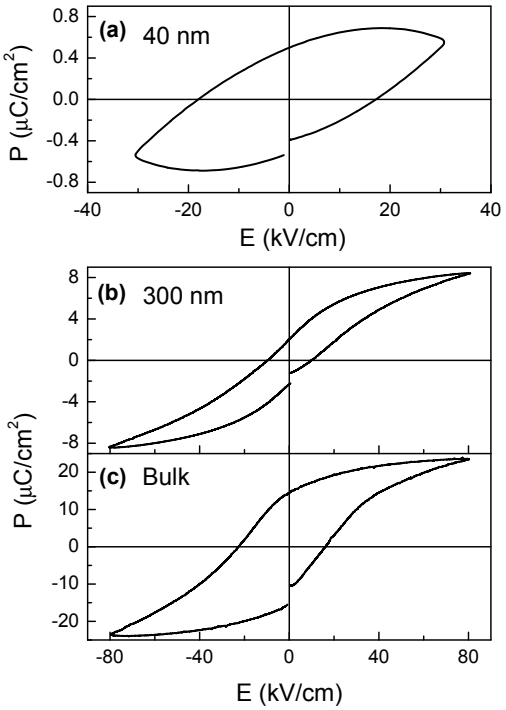

Figure 5.3: Room-temperature polarization versus electric field curve of (a) 40 nm, (b) 300 nm and (c) bulk BTO.

The polarization (P-E) hysteresis loop measured for the 40 nm sample is (Fig. 5.3a) similar to that reported for 50-100 nm BTO particles [101]. This kind of P-E loop does not quite represent the true ferroelectric nature of the particles, as one can expect such behavior in the P-E measurement carried out on cold pressed nanoparticles. It requires a local probe such as Electric Force Microscope (EFM) to see switching of polarization in individual nanoparticles. In fact, with the use of EFM technique it has already been shown that nanoparticles of $BaTiO_3$ with an average size of as small as 12 nm is ferroelectric [85]. However, a clear ferroelectric nature of polarization hysteresis is seen (Fig. 5.3b) in the sintered particles (300 nm). For a drive voltage of 2 kV, the hysteresis loop recorded at a frequency

of 100 Hz shows a remnant polarization (P_r) value of 2.04 $\mu C/cm^2$, a maximum polarization (P_{Max}) of 8.42 $\mu C/cm^2$ and a coercive field (E_c) of 10 kV/cm. For the bulk BTO, these parameters are; P_r = 14.5 $\mu C/cm^2$, P_{Max} = 23.4 $\mu C/cm^2$ and E_c = 22 kV/cm (Fig. 5.4).

5.3.4 Dielectric studies

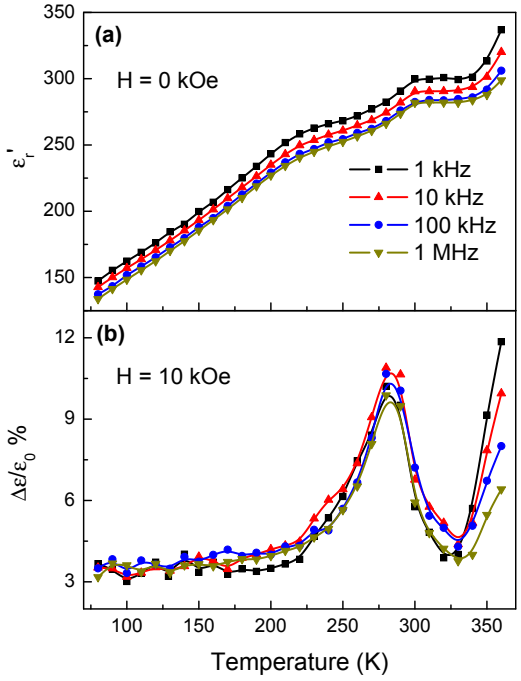

Figure 5.4: Temperature-dependent (a) dielectric constant and (b) magnetocapacitance of nanocrystalline BTO.

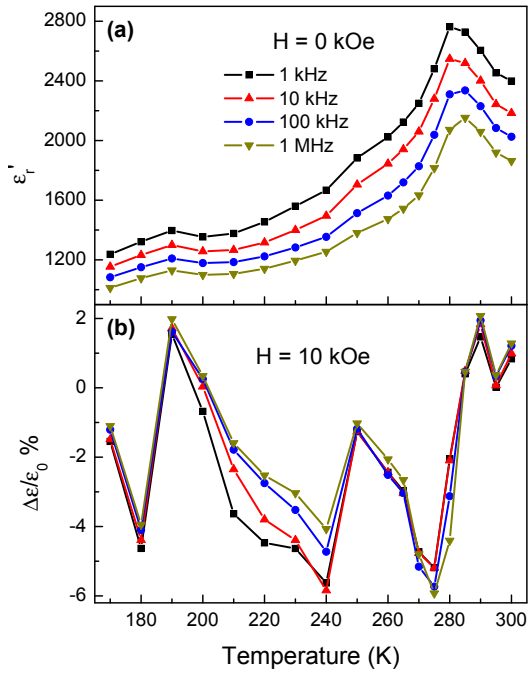

Figure 5.5: Temperature-dependent (a) dielectric constant and (b) magnetocapacitance of bulk BTO.

The temperature dependence of the dielectric constant (Fig. 5.4a) of 300 nm nanocrystalline BTO sample at various frequencies exhibits dielectric anomalies around 230 K and 300 K, which correlate respectively with the ferroelectric phase transitions of BTO from the low-temperature rhombohedral to the orthorhombic

structure followed by the orthorhombic to tetragonal phases. The coupling between magnetization and electric polarization in the BTO nanocrystalline sample is manifested in the magnetocapacitance (MC): $\Delta\varepsilon(H)/\varepsilon(0) = [\varepsilon(H)-\varepsilon(0)]/\varepsilon(0)$. We observe a positive MC of fairly large magnitude (10 %) near room temperature in an applied magnetic field of 1 T (see figure 5.4b for its temperature dependence in the interval 77-360 K), which remains positive down to 77 K. The increase of MC above room temperature should be associated with the tetragonal to cubic transition that is expected to be around 400 K. For bulk BTO, Dielectric measurements shows anomalies near phase transition temperatures (Fig. 5.5a) but MC measurement shows that there is no influence due to the applied magnetic field(Fig. 5.5b).

5.3.5 First-principles calculations

We now develop an understanding of these observations using first-principles density functional theory (DFT) calculations, which have proven to be quite effective in the determination of the origin of ferroelectricity in $BaTiO_3$ [9], focusing here on identification of the origin of its ferromagnetism at nano-scale. Simplifying the geometry of nanocrystalline BTO and their structure, we consider here a slab of $BaTiO_3$ of 1.2 nm thickness, consisting of seven [100] atomic planes and terminated with TiO_2 planes. We use a periodic supercell that consists of the slab and vacuum layers with in-plane periodicity of 2×2 unit cells of $BaTiO_3$. In the absence of any defects, such a slab is a good insulator as each plane is charge neutral (either BaO or TiO_2) and does not exhibit any magnetism as all the Ti^{4+} cations are in the d^0 state.

Our first-principles calculations are based on a spin-dependent density func-

tional theory calculations using a standard plane-wave code Quantum ESPRESSO [102] with a local density approximation [103] to interaction energy of electrons. We use ultra-soft pseudo-potentials [104] to represent the interaction between ions and electrons, and include semi-core s and p states of Ti and Ba explicitly in the valence. An energy cutoff of 30 Ry (180 Ry) on the plane wave basis was used in representation of Kohn-Sham wave-functions (density). Most calculations involved supercells with 70 atoms; phonons were determined for a smaller supercell with 24 atoms using a frozen phonon method. The supercell with 70 atoms consists of 2 $\times$ 2 unit cells in the plane of the surface and allows for reconstruction, particularly in the presence of oxygen vacancies at the surface. Brillouin zone integrations were sampled with a Monkhorst-Pack mesh [105] of k-points that is equivalent to a 4 $\times$ 4 $\times$ 4 mesh for the primitive cell of $BaTiO_3$. Structural optimization was carried out with BFGS algorithm to minimize energy using Hellman-Feynman forces.

From the earlier experimental [84] and theoretical [99] work, it is known that magnetism in oxide nanoparticles arises from vacancies. Oxygen vacancies are not uncommon in oxides of the type BTO. To assess the site preference of oxygen vacancies, we determined fully relaxed spin-dependent ground state structures for two configurations, one with oxygen vacancies in the bulk, and another with oxygen vacancies at the surface of the slab. With the choice of the supercell we have used, the in-plane concentration of vacancies is 12.5 atomic % ($<$ 5 atomic % in cell). We find that the configuration with oxygen vacancies at the surface is lower in energy by about 1.2 eV per oxygen vacancy. The magnitude of this energy difference is much larger than any errors in the DFT calculations and implies a much greater abundance of oxygen vacancies at the surface than in the bulk at room temperature ($\Delta E/k_BT = 48$; note that the entropy of vacancy sites in the bulk is higher due to larger number of configurations available, but its contribution to free energy

diminishes at nano-scale)

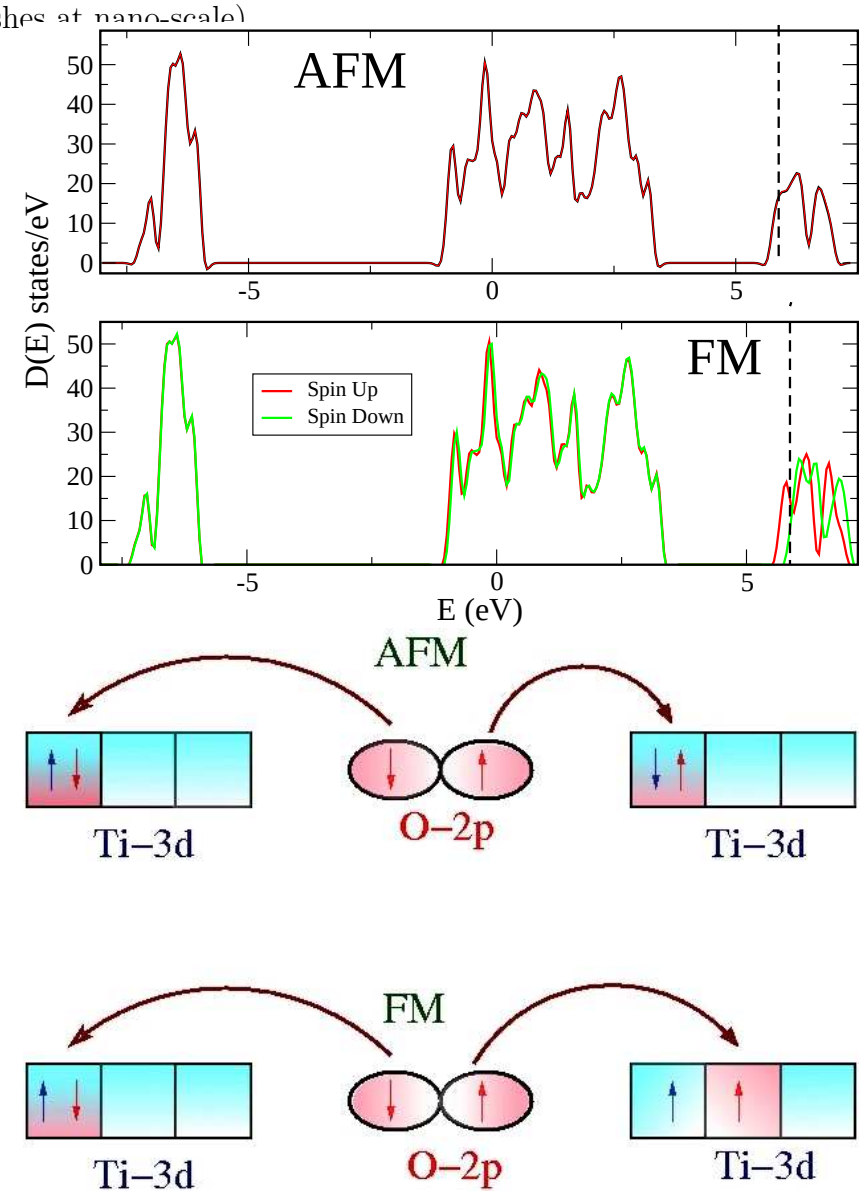

Figure 5.6: Mechanism of magnetism in $BaTiO_3$ with oxygen vacancies. Top two panels show the density of electronic states of AFM and FM states of the configuration with oxygen vacancies at the surfaces. In the bottom half, a sketch of superexchange interactions shows that the same d-state is involved in the AFM state, while two different d-states are involved in the FM state. The latter is more stable than the former due to Hund's coupling that favors parallel alignment of spins of electrons in different d-states.

We now assess the stability of ferromagnetic and antiferromagnetic states in

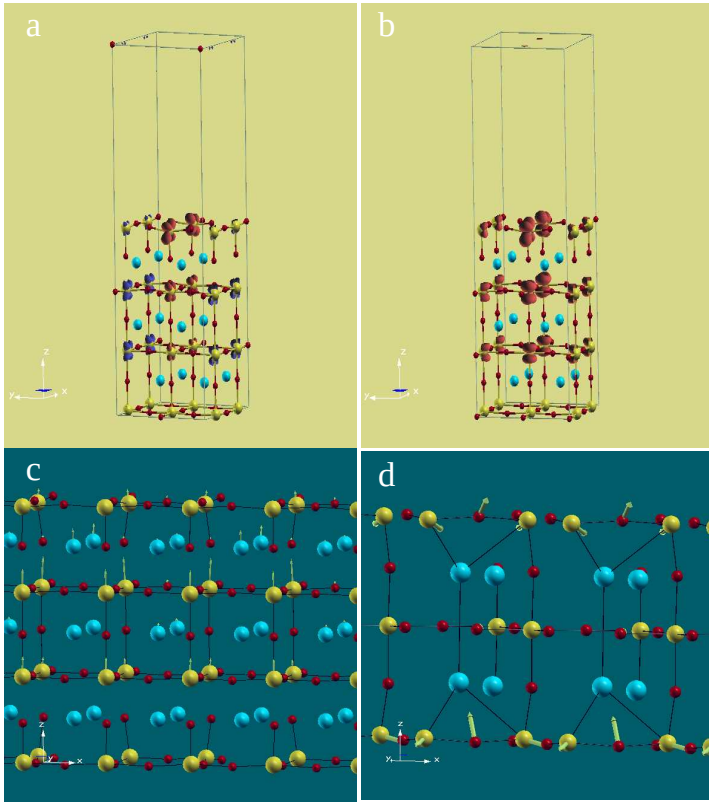

Figure 5.7: Magnetization density and low-energy structural distortions of nano-slabs of $BaTiO_3$. Barium, Titanium and Oxygen atoms are shown as blue, yellow and red spheres respectively, and the slab extends periodically to infinity in the plane perpendicular to the z-axis (vertical direction [1]). Isosurfaces of magnetization density at 10% of its peak values (red and dark blue isosurfaces indicate positive and negative magnetization respectively) shown for AFM state (a) and FM state (b) of nano-slab with oxygen vacancy on the top [001] plane reveal that the magnetization penetrates about 1 nm from the surface. Cylindrical symmetry of magnetization density at Ti sites in the FM state (b) gives additional evidence for the two d-orbitals xz and yz involved in FM exchange. In (c), arrows indicate atomic displacements (within a factor) that link a ferroelectric FM state polarized along [001] direction with the reference centrosymmetric FM state of nano-slab with oxygen vacancies at both the surfaces. It is clear that polar off-centering atomic displacements are very small at the surfaces. In (d), the unstable phonon mode found in the AFM state of nano-slab with 5 atomic planes and oxygen vacancies on both the surfaces: it is localized at the surface and couples strongly with spin-ordering at the surface.

the presence of oxygen vacancies both in the bulk and at surfaces. As the coordination of oxygen is two (both being Ti atoms), its vacancy is expected to result

in occupation of d-states of primarily the neighbouring Ti atoms with an electron each. FM and AFM ordering have been simulated by initializing spins on these two Ti ions to parallel and anti-parallel configurations respectively. In either case, we find the ferromagnetic state to be lower in energy by more than 10 meV with 2 μ_B magnetic moment per oxygen vacancy. The origin of this can be understood from interpretation of the density of states (Fig. 5.6) with exchange interactions. Upon introduction of oxygen vacancies, states with Ti d-character at the bottom of the conduction band get populated with a total of two electrons per oxygen vacancy. These states are relatively extended (more than one nm from the surface, see figure 5.7a, b) and their energies split up due to spin-dependent interaction. As these states are quite extended in the plane of the surface, they allow mediation the magnetic interactions necessary for a long-range order [99, 100]. The ferromagnetic superexchange involves two different d- states (xz and yz) populated with electrons of parallel spins and Hund's coupling favors it to antiferromagnetic superexchange involving the same d- state populated with electrons of anti-parallel spins (Fig 5.6). Consistent with its greater stability, the density of states in the FM configuration exhibits a dip or a pseudo-gap at the Fermi level.

To estimate the effects of oxygen vacancies on ferroelectricity, we have determined the energetics of structural distortions corresponding to local energy minima in which all the Ti atoms in the supercell are off-centered along a given direction (say, (001), (110) and (100)). In the ferromagnetic state of the nano-slab with oxygen vacancies at the surface, we find the ferroelectric phase polarized along (110) axis to be the lowest in energy, followed by the ones polarized along (100) and (001) directions respectively. The energy lowering with ferroelectric distortions along each of the three directions is noticeably lower for the slab with reflection symmetry in the horizontal plane (σ_z, oxygen vacancies at both surfaces), than

that for the asymmetric slab with oxygen vacancy at only one of the two surfaces. While the lowering of energy with ferroelectric distortions in slabs is about three times weaker than in the bulk, ferroelectricity does seem to survive in the nano-thin slabs of $BaTiO_3$ with oxygen vacancies at the surface. Ferroelectric structural distortions mainly involve off-centering of Ti and O atoms and they are much smaller at the surface than in the interior of the slab (Fig. 5.7c).

To assess the local stability of the completely relaxed FM and FE structure, we have determined Γ point phonons (note that they include phonons corresponding to Γ, X, M and R modes of the bulk). We find that all the phonons are stable in the FM state, with four of them below 100 cm^{-1}, which is expected of a ferroelectric material [106]. The frequency of most of these phonons changes by at most 0.5 % when the magnetic ordering changes from FM to AFM type, indicating a rather weak spin-phonon coupling. However, we find an unstable phonon ($\omega = 170i$ cm^{-1}) in the AFM state that has a strong overlap (40 %) with a phonon at 300 cm^{-1} in the FM state, indicating its very strong coupling with spin. This mode (Fig. 5.7d) is confined to the surface of the slab (like the magnetization density of the AFM state) and has some components of the other low-energy phonons of the FM state as well. Its coupling with spin should have therefore observable consequences when these soft modes show a strong temperature dependence, ie. near the ferroelectric transitions. In particular, changes in magnetization with applied magnetic field would result in shifts in the frequency of these soft polar modes and hence in its contribution to dielectric response. This surface mode (Fig. 5.7d) is thus responsible for the magneto-capacitive anomaly observed here experimentally.

5.3.6 Positron annihilation

PAS can provide valuable information about the nature of defects as the annihilation parameters are sensitive to lattice imperfections. In PAS, the positron may be trapped in crystal defects, i.e. the wave function of the positron is localized at the defect site until annihilation and thus useful to characterize the defects in the sample [107, 108]. PAS has been used to characterize defects in metals, semiconductors and polymers. Further, it has been shown that PAS is an excellent technique for studying open-volume defects, vacancy-impurity complexes, and for identifying the sublattice occupied by the dopants. Previous studies on doped and undoped BTO using PAS has been shown to reveal that the nature of defect is oxygen vacancy [107]. Hence, we have investigated the BTO nanoparticles of different sizes using PAS and correlate the results with the saturation magnetization. XRD patterns confirmed that all the samples were single phase with a tetragonal structure. FESEM image of samples heated at 700 ^{o}C, 1000 ^{o}C and 1200 ^{o}C are shown in figure 5.8(a-c). The 700 ^{o}C heat treated sample shows rods containing assemblies of nanoparticles with an average diameter of 60 nm (Fig. 5.8a). Figure 5.8b shows the 100 nm nanoparticles prepared by 1000 ^{o}C heat treatment. The FE-SEM image of the bulk BTO sample (Fig. 5.8c), obtained by sintering the pressed nanoparticles at 1200 ^{o}C, shows the average grain size to be around ~ 2 μm.

The magnetic measurements carried out on 60 nm, 100 nm and 2 μm (bulk) samples and are shown in figure 5.8d. The first two samples clearly show ferromagnetism at room temperature whereas the 2 μm sample shows diamagnetic curve as expected for the bulk BTO. The saturation magnetization of smaller (60 nm) particles is higher (0.00298 emu/gm) than that (0.00213 emu/gm) of bigger particles which is consistent with the suggestion that surface defects decreases with

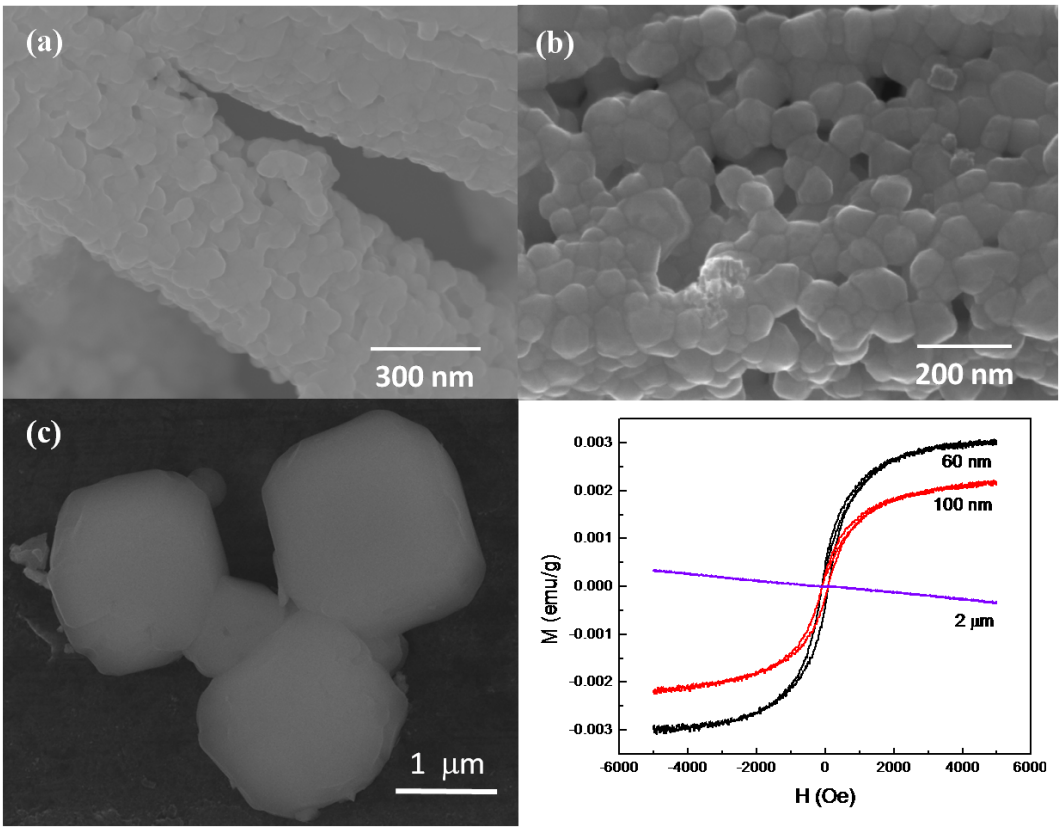

Figure 5.8: FESEM micrographs of $BaTiO_3$ nanoparticles treated at (a) 700 ^oC, (b) 1000 ^oC and (c) 1200 ^oC. (d)Room temperature magnetic hysteresis of 60 nm, 100 nm and 2 μm size $BaTiO_3$.

increasing particle size [109].

Table 5.2: Positron lifetimes and their corresponding intensities for all the three BTO samples.

Sample	τ_1 (ps)	τ_2 (ps)	τ_3 (ps)	I_2 (%)	I_3 (%)
60 nm	163 ± 2	348 ± 10	1965 ± 100	51 ± 1	4 ± 0.2
100 nm	165 ± 2	322 ± 8	1631 ± 100	48 ± 1	2 ± 0.2
2 μm	161 ± 2	353 ± 10	1465 ± 100	18 ± 1	1 ± 0.2

Table 5.2 shows the value of the positron lifetimes and their corresponding intensities for all the three BTO samples. The free fitting of all the positron lifetime spectra for all the three samples (60 nm, 100 nm and 2 μm) are found to be best

fitted with three lifetime components fitting, yielding a very long (1400 to 2000 ps) lifetime component (τ_3) with intensity (I_3) of 1 to 4 %. This component is due to the formation of orthopositronium and its subsequent decay as parapositronium by pick-off annihilation processes [88, 89]. In polycrystalline samples, there always exist microvoids where positronium formation is favorable. The short lifetime component (τ_1) of 163 ± 2 ps is generally attributed to the free annihilation of positrons. The theoretically calculated free positron lifetime in bulk $BaTiO_3$ is 152 ps, which is slightly less than the presently observed value, 163 ± 2 ps [107]. The most important lifetime component is the intermediate one, τ_2, which arises from the annihilation of positrons at defect sites. One can have an idea about the defect concentration from I_2, the intensity of the intermediate lifetime component [88–90]. It is obvious from table 1 that the I_2, which is a measure of defect concentration, is higher in 60 and 100 nm particles than the bulk sample and decreases with increasing particle size. Thus, as the particle size increases, the decrease of magnetization or the suppression of magnetism is in agreement with the decrease of defect concentration.

In order to identify the nature of defects in BTO samples, ratio-curve analysis technique of CDBAR spectra has been used [93–96, 107]. Figure 5.9 shows the area normalized ratio curve of CDBAR spectra of the three samples (60 nm, 100 nm and 2μm) with respect to CDBAR spectrum of defects free 99.9999% purity Al sample. All the ratio curves (Fig. 5.9) show one major peak at $\sim 11 \times 10^{-3}$ $m_o c$ and another peak at $\sim 20 \times 10^{-3}$ $m_o c$. In general, the peak at momentum value $\sim 11 \times 10^{-3}$ $m_o c$ in the ratio-curve with respect to Al is mainly coming from the annihilation of positrons with the $2p$ electrons of oxygen and some contributions coming from the annihilations with the $3d$ electrons of Ti, $5p$ electrons of Ba, while the peak at momentum value $\sim 20 \times 10^{-3}$ $m_o c$ is coming from the annihilation of

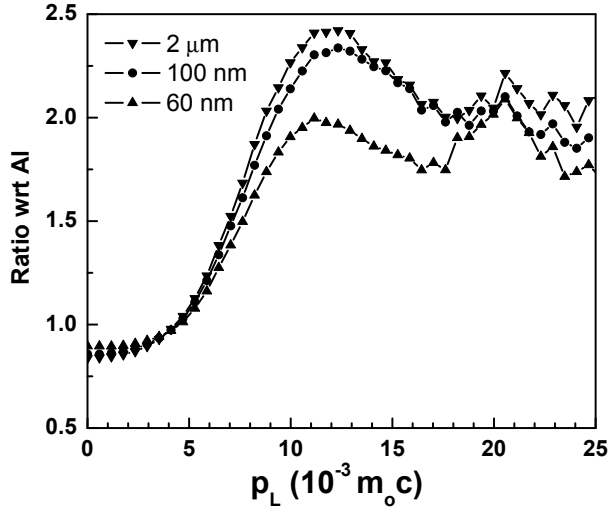

Figure 5.9: Area normalized ratio curve of 60 nm, 100 nm and 2 μm size $BaTiO_3$ CDBAR spectra with respect to defects free 99.9999 % purity Al CDBAR spectrum.

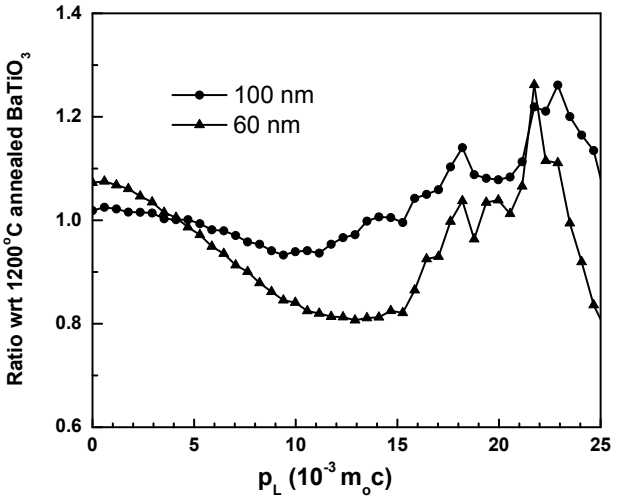

Figure 5.10: Area normalized ratio curve of 60 nm and 100 nm size $BaTiO_3$ CDBAR spectra with respect to 2 μm size $BaTiO_3$ CDBAR spectrum.

positrons with the core electrons of Ti. From figure 5.9 it is clear that the peak height at $\sim 11 \times 10^{-3}$ $m_o c$ decreases with decreasing particle size, while the peak height at $\sim 20 \times 10^{-3}$ $m_o c$ is almost same for all the three samples, which indicates

the presence of a significant amount of oxygen vacancy in 60 nm particles than the bulk sample. This is also clear from figure 5.10 where area normalized ratio curve of 60 nm and 100 nm samples have been plotted with respect to the bulk BTO CDBAR spectrum. Figure 5.10 also shows a broad dip in the momentum value $\sim 11 \times 10^{-3}$ $m_o c$. This indicates lesser annihilation of positrons with the $2p$ electrons of oxygen in the 100 nm and 60 nm samples compared to the bulk sample. Similar trend of ratio curve has also been observed by Ghosh *et al.* [107] on $BaTiO_3$ samples with oxygen vacancy (V_O). Thus, from ratio curve analysis, defects in 100 nm and 60 nm samples have been identified as oxygen vacancy. Each oxygen vacancy is expected to donate two electrons to the empty d-state of single Ti^{4+}-ion to become Ti^{2+} ion or one electron each to two Ti^{4+}-ions, probably situated on either side of the oxygen vacancy, to make them Ti^{3+}-ions [99, 110]. Both the configurations result in the ferromagnetic ground state due to Hund's rule coupling provided there is a minimum concentration of oxygen vacancies required for magnetic percolation. The fact that relatively large value of I_2 and the observed ferromagnetism in 60 nm and 100 nm samples indicate the presence of critical concentration of oxygen vacancies on the surface of the particles. In the case of bulk sample, the low value of defect is consistent with the observed diamagnetism.

Nanocrystalline $BaTiO_3$ with an average size of 60 nm and 100 nm show ferromagnetic hysteresis at room temperature whereas the 2 μm sample exhibits diamagnetism as expected for a bulk sample. Positron annihilation studies show lesser annihilation of positrons with the $2p$ electrons of oxygen in the 100 nm and 60 nm samples compared to the bulk sample indicates the presence of oxygen vacancies. Thus, the observed ferromagnetism in nanocrystalline $BaTiO_3$ samples can be correlated with presence of oxygen vacancy at the surface of the particles.

5.4 Conclusions

In conclusion, the present study demonstrates a new kind of multiferroicity in classical ferroelectric $BaTiO_3$ in nanocrystalline form. The multiferroic nature is rendered possible by the surface magnetism of the nanocrystalline BTO. Interestingly, the ferroelectric and magnetic properties are coupled as shown by the observation of magnetocapacitance. It is interesting to ponder on the possible existence of both ferroelectricity and ferromagnetism occurring at the surfaces of nanoparticles of the otherwise non-ferroic oxides. Positron annihilation studies show the presence of oxygen vacancy at the surface of the particles which can be related to the observed ferromagnetism.

CHAPTER 6

Crystal structure and dielectric properties of ordered perovskites, $Ba_{2-x}Sr_xBiSbO_6$ ($0 \leq x \leq 2$) and $BaBi_{0.7}Nb_{0.3}O_3$**

6.1 Introduction

Oxides with perovskite structure have been investigated for their interesting physical properties such as magnetism, superconductivity, magnetoresistance and ferroelectricity [111]. The perovskite compound $BaBiO_3$ (BBO) is a well known charge ordered semiconductor where Bi^{3+} and Bi^{5+} ions are ordered in rock-salt manner and thus the chemical formula is written as $Ba_2Bi^{+3}Bi^{+5}O_6$. This compound becomes superconductor upon partial replacement of Ba^{2+} ions with Pb^{2+}/K^+ ions [112–115]. Hence, the bismuth valence state has become an important parameter to understand the physical properties of bismuth containing compounds. Bismuth ions with $6s^2$ and $6s^0$ configurations are common while the intermediate $6s^1$ state does not exist. BBO has been reported to have monoclinic structure ($a \approx b \approx a_p\sqrt{2}$; $c \approx 2a_p$ and $\beta \approx 90^o$) at room temperature with centrosymmetric $I2/m$ space group based on analysis of powder neutron data [116]. In the monoclinic structure,

Paper based on this work has been published in *Chem. Mater.* **19 (2007) 4114; *Physica B* **404** (2009) 154; A manuscripts based on a part of this work is submitted and two more under preparation

BBO has been reported to have two different BiO_6 octahedra with shorter and longer bond lengths which corresponds to Bi^{5+} and Bi^{3+} ions arranged in an alternate fashion [116]. However, a recent study based on convergent beam electron diffraction showed non-centrosymmetric triclinic symmetry [117]. Recently, there has been a great deal of interest in compounds having $6s$ lone pair which may be stereochemically active as in PbO [118, 119], rendering the compounds ferroelectric [17, 120]. Since BBO contains $6s$ lone pair electrons, it is of interest to study the structure and dielectric properties by replacing Bi^{5+} ions with other pentavalent ions (Sb^{5+} and Nb^{5+}) as the parent compound is highly conducting. We also studied the compounds prepared by replacing Ba^{2+} ions with Sr^{2+} ions in Ba_2BiSbO_6 (BBS). The compound BBS, prepared by the complete replacement of larger size Bi^{5+} ions with smaller Sb^{5+} ions [121], has been reported to exhibit centrosymmetric rhombohedral structure ($R\bar{3}$) based on neutron diffraction data collected using longer wavelength $\lambda = 2.5724$ Å [122]. Later Kennedy *et al.* [123] confirmed the room temperature structure and also reported the high and low temperature phase transitions using high resolution time-of-flight neutron data. In BBS, oxygen ions are located significantly away from their ideal positions and form a larger BiO_6 and smaller SbO_6 octahedra which are arranged alternatively with bismuth and antimony in +3 and +5 oxidation states respectively [123]. Since the structure depends on the exact location of oxygen ions, an accurate determination of oxygen positions is necessary to confirm the structure.

Further these ordered perovskites are known to undergo various structural transitions. BBO undergoes several structural phase transition in the temperature range 4.2 - 975 K, the low-temperature monoclinic ($P2_1/n$) to the room-temperature monoclinic ($I2/m$) at 132 K, $I2/m$ to the rhombohedral ($R\bar{3}$) at 430 K, and finally, to the high-temperature cubic ($Fm\bar{3}m$) phase at 820 K. A similar

structural behavior is reported for another derivative of BBO, namely, BBS, except that the transition temperatures are lower: 250 K for I*2/m* to R$\bar{3}$ and 515 K for R$\bar{3}$ to F$m\bar{3}m$, and the low-temperature structure (P$2_1/n$) is not formed at all. The fact that the transition temperatures are lower in BBS is due to the substitution of smaller Sb^{5+} ions (r = 0.60 Å) for larger Bi^{5+} ions (r = 0.76 Å) or a chemical pressure [121]. It is interesting and important to note a pressure dependent study on BBS, which revealed that the rhombohedral phase of BBS undergoes a phase transition to the monoclinic I*2/m* structure. These studies confirm that both pressure and temperature can induce these structural changes.

Here, we report the structural and dielectric properties of Ba_2BiSbO_6 (BBS), $BaSrBiSbO_6$ (BSBS), Sr_2BiSbO_6(SBS) and $BaBi_{0.7}Nb_{0.3}O_6$ (BBN).

6.2 Experimental

The samples $Ba_{2-x}Sr_xBiSbO_6$ (x = 0, 1 and 2) and $BaBi_{0.7}Nb_{0.3}O_6$ were prepared by conventional solid state reaction method. Stoichiometric amount of high purity $BaCO_3$/$SrCO_3$, Bi_2O_3 and Sb_2O_5/Nb_2O_5 were weighed and mixed thoroughly in an agate mortar. The mixed powder was calcinated at 700 ^{o}C and 800 ^{o}C for 24 hours with intermittent grindings. Finally, the powder was pressed into pellets and sintered at 900 ^{o}C for 12 hours. The sample $BaBi_{0.7}Nb_{0.3}O_6$ was sintered at 950 ^{o}C for 12 h in a flowing O_2 atmosphere. The phase purity was verified with Bruker D8 Discover x-ray diffractometer using Cu Kα radiation. Rietveld refinements, using the program GSAS [124, 125], were carried out on the neutron diffraction data collected for BBS using D2b instrument with a wavelength λ = 1.051 Å at Institut Laue Langevin (ILL), Grenoble, France. For BSBS, data were collected at 295 K, 150 K and 3.5 K with λ = 1.594 Å and using the same wavelength the room

temperature data was collected for BBN. The Electron Diffraction (ED) studies of Sr_2BiSbO_6 were carried out using JEOL 200CX electron microscope fitted with an eucentric goniometer ($\pm 60^o$) equipped with a KEVEX Energy Dispersive Spectroscopy (EDS) analyzer. Specimens for transmission electron microscopy (TEM) were prepared by crushing a small piece of the sample in an agate mortar containing ethanol and dropping a droplet on a copper grid covered by a holey carbon film. High-resolution Z-contrast images were obtained using a 3000F microscope equipped with a Scanning Transmission Electron Microscopy (STEM) unit operating with a High Angle Annular Dark Field (HAADF) detector (resolution of 1.36 Å). Capacitance and dissipation of the samples for various frequencies ranging from 100 Hz to 1 MHz were measured using Agilent impedance analyzer from room temperature to 800 K. For dielectric studies, the capacitor was prepared by sputtering gold on both sides of the pellet using DC sputtering.

6.3 Results and discussion

6.3.1 Ba_2BiSbO_6 and $BaSrBiSbO_6$

6.3.1.1 Structural analysis

The compounds, BBS and BSBS crystallize in the centrosymmetric space group $R\bar{3}$. BBS forms a pure phase whereas BSBS sample has minor impurity phases, $Sr_{1-x}Bi_{2+x}O_4$ (4 %) and Sb_2O_3 (2 %). In BBS, substitution of Sr^{2+} ions at Ba-site has no influence on the room temperature structure and the structure remains unchanged up to a solubility limit of 50 %. The structural change from the monoclinic structure of BBO to the rhombohedral structure in BBS and BSBS upon substitution is believed to be due to smaller ionic size of the substituted ions [123].

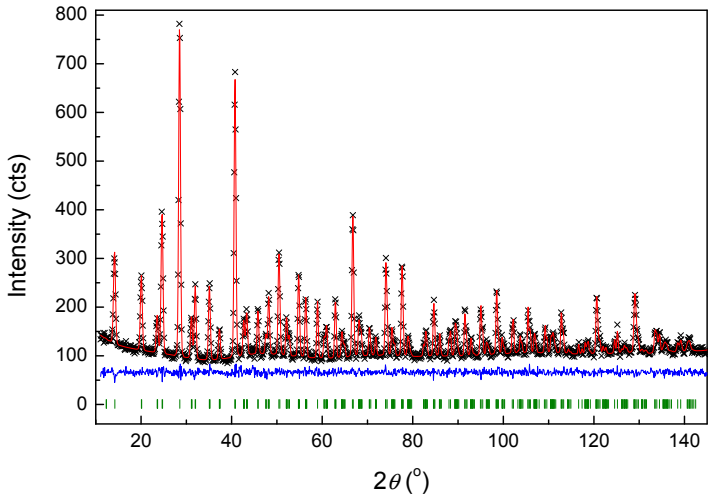

Figure 6.1: Rietveld refinement on powder neutron diffraction data of Ba_2BiSbO_6, collected at room temperature using D2b instrument with $\lambda = 1.051$ Å at the Institut Laue Langevin (ILL), Grenoble, France.

The chemical formula of these compounds can be written as $Ba_2^{2+}Bi^{3+}Sb^{5+}O_6$ and $Ba^{2+}Sr^{2+}Bi^{3+}Sb^{5+}O_6$, in which Bi-ions are in +3 oxidation state with $6s^2$ lone pair electrons and Sb-ions in +5 oxidation state. Figure 6.1 shows Rietveld fit to the room temperature neutron diffraction data for Ba_2BiSbO_6. The structural parameters obtained from the final refinement at convergence are given in table 6.1. The cell parameters are $a = 6.0351(2)$ Å and $\alpha = 60.202(1)^o$. The average bond lengths of Bi-O and Sb-O obtained are 2.303(2) and 1.989(2) Å respectively. The obtained structural parameters are in agreement with the reported values in literature where the structural parameters were reported from the neutron data with higher wavelength $\lambda = 2.5724$ Å [122]. The bond lengths are also in agreement with value reported from time-of-flight neutron data recorded to a total incident proton beam of 35-70 μA h [123].

The observed, calculated and difference neutron pattern of BSBS at 295 K, 150 K and 3.5 K are shown in the figure 6.2. The first row of vertical tick mark shows

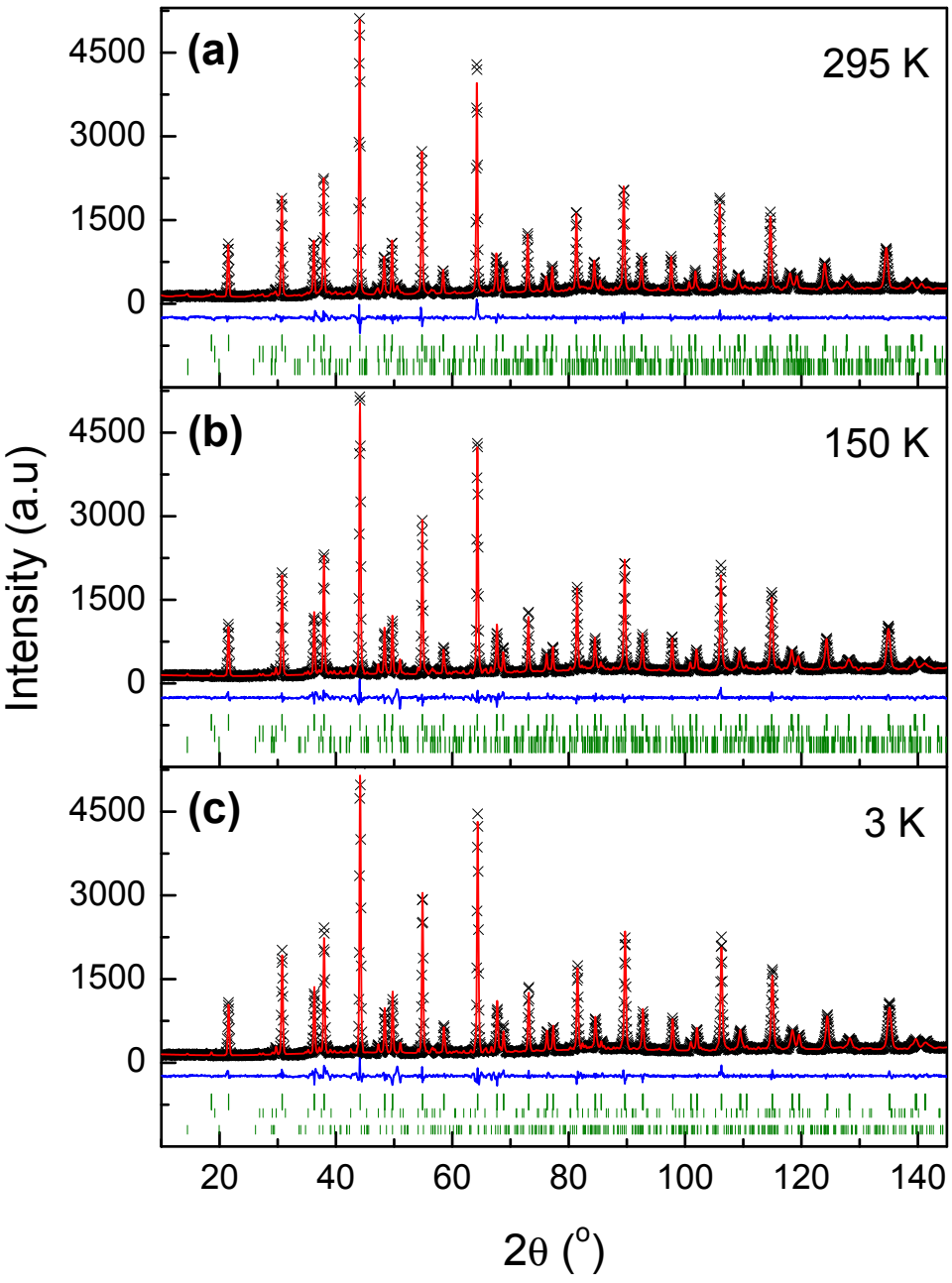

Figure 6.2: Rietveld refinement on powder neutron diffraction data of $BaSrBiSbO_6$, collected at (a) 295 K, (b) 150 K and (c) 3K using D2b instrument with $\lambda = 1.594$ Å at the Institut Laue Langevin (ILL), Grenoble, France. Vertical tick marks show the possible reflections of $BaSrBiSbO_6$ (first row) along with $Sr_{1-x}Bi_{2+x}O_4$ (second row) and Sb_2O_3 (third row) impurity phases.

Table 6.1: Structural parameters for Ba_2BiSbO_6 obtained from Rietveld refinement with the room-temperature neutron diffraction data collected with $\lambda = 1.051$ Å.

Parameters	Ba_2BiSbO_6
Space group	$R\bar{3}$
a (Å)	6.0351(2)
α (^{o})	60.202(1)
V (Å^3)	156.14(1)
Ba,Sr: x, y, z	0.2504(6), 0.2504(6), 0.2504(6)
U_{iso}/U_{11}	0.87(4)
Bi: x, y, z	0, 0, 0
U_{iso}/U_{11}* 100	0.66(5)
Sb: x, y, z	1/2, 1/2, 1/2
U_{iso}/U_{11}	0.23(6)
O: x, y, z	0.2357(4), 0.3012(4), 0.7318(8)
U_{iso}/U_{11}	1.48(12)
U_{22}, U_{33}, U_{12}, U_{13}, U_{23}	1.70(9), 2.1(1), -1.3(1), -0.3(1), -0.1(1)
R_{wp} (%)	3.59
χ^2	1.283
Bi-O (Å)	2.303(2)
Sb-O (Å)	1.989(2)

the Bragg position of the BSBS phase whereas the second and third row belongs to the impurity phases, $Sr_{1-x}Bi_{2+x}O_4$ and Sb_2O_3 respectively. Table 6.2 shows the structural parameters obtained for BSBS at different temperatures. The cell parameters obtained are $a = 5.9809(2)$ Å and $\alpha = 60.045(2)^o$ at room temperature. The volume of the cell in BSBS is smaller than BBS confirming that the smaller Sr^{2+} ions substitute at Ba^{2+} site. In the rhombohedral symmetry, the alkaline earth ions share the same position and Bi^{3+} occupies {0, 0, 0} site whereas Sb^{5+} occupies

Table 6.2: Structural parameters obtained from Rietveld refinement on neutron diffraction data collected (λ = 1.594 Å) at 295, 150 and 3.5 K for $BaSrBiSbO_6$.

$BaSrBiSbO_6$			
Parameters	3.5 K	150 K	295 K
Space group	$R\bar{3}$	$R\bar{3}$	$R\bar{3}$
a (Å)	5.9672(2)	5.9706(2)	5.9809(2)
α (^{o})	60.038(3)	60.037(3)	60.045(2)
V (Å^3)	150.37(1)	150.62(1)	151.43(1)
Ba,Sr: x, y, z	0.2481(7), 0.2481(7), 0.2481(7)	0.2533(9), 0.2533(9), 0.2533(9)	0.2475(7), 0.2475(7), 0.2475(7)
U_{iso}/U_{11}	1.11(6)	1.07(5)	1.80(5)
Bi: x, y, z	0, 0, 0	0, 0, 0	0, 0, 0
U_{iso}/U_{11}	1.38(8)	2.1(1)	0.40(8)
Sb: x, y, z	½, ½, ½	½, ½, ½	½, ½, ½
U_{iso}/U_{11}	0.27(9)	0.6(1)	1.9(2)
O: x, y, z	0.2131(9), 0.3178(8), 0.716(1)	0.2091(9), 0.3184(8), 0.723(1)	0.2232(9), 0.3090(7), 0.719(1)
U_{iso}/U_{11}	4.0(4)	5.9(4)	5.8(3)
U_{22}, U_{33}, U_{12}, U_{13}, U_{23}	9.5(4), 3.1(2), -6.1(3), -2.2(2), 2.4(2)	10.6(4), 1.1(2), -7.3(3), -1.6(2), 2.8(2)	13.9(4), 2.4(2), -8.3(3), -0.6(2), 0.1(3)
R_{wp} (%)	7.27	7.25	6.11
χ^2	1.702	1.678	1.18
Bi-O (Å)	2.265(4)	2.253(5)	2.268(4)
Sb-O (Å)	2.008(4)	2.024(5)	1.998(4)

{½, ½, ½} site. Similar to BBS, the bond distance calculation showed that the average bond lengths of Bi-O and Sb-O are 2.268(4) and 1.998(4) Å respectively. The values are consistent with the values reported for BBO and BBS [123]. Even though the BSBS structure fits well in space group $R\bar{3}$ with reliable agreement factors and structural parameters, structural analysis were been carried out using

non-centrosymmetric space group R3, a subgroup of R$\bar{3}$, on the room-temperature neutron data. The model gave a fit with $\chi^2 = 3.655$ and $R_{wp} = 10.70$ % which are higher than that for R$\bar{3}$ ($\chi^2 = 1.18$ and $R_{wp} = 6.11$ %). Thus the space group R$\bar{3}$ fits well for BSBS structure.

Further, low temperature analysis were also carried out to check whether there is any structural transition to monoclinic structure as reported for BBO and BBS [123]. In BBO, there is a discontinuous structural transition from R$\bar{3}$ to I*2/m* at around 430 K and the later transform to P$2_1/n$ at low temperature (132 K). BBS undergoes the structural transition from R$\bar{3}$ to I*2/m* at 250 K and there was no evidence for further structural transition down to 4.2 K [123]. A pressure-dependent study on BBS also reported a similar structural transition at 4 GPa [126]. Structural analysis on neutron data collected at 150 K confirmed that the structure remains in rhombohedral symmetry (Fig. 6.2b). The cell parameters obtained from 150 K data are $a = 5.9706(2)$ Å and $\alpha = 60.037(3)^o$. The average bond length of Bi-O and Sb-O obtained are 2.253(5) Å and 2.024(5) Å respectively. Further, the refinement on 3.5 K data (Fig. 6.2c) showed that the BSBS system remains in R$\bar{3}$ symmetry and the low temperature monoclinic phase (I*2/m*) does not exist in BSBS probably due to the substitution of smaller Sr^{2+} ion at the Ba^{2+}-site. The refinement on 3.5 K data gave a good fit for with $\chi 2 = 1.702$ and $R_{wp} = 7.27$ % than that for the monoclinic I*2/m* ($\chi^2 = 5.576$ and $R_{wp} = 13.16$ %). The lattice parameters obtained at 3.5 K for the rhombohedral space group are $a = 5.9672(2)$ Å and $\alpha = 60.038(3)^o$. The bond length calculation showed that the bond length of Bi-O and Sb-O are 2.265(4) Å and 2.008(4) Å respectively. The larger value of α in BBS compared to BSBS indicates that the transition from R$\bar{3}$ to cubic in the former will occur at relatively higher temperature. For the same reason, the BBS may undergo transition at low temperatures to a low symmetry

structure at relatively higher temperature compared to BSBS. This is consistent with the absence of low temperature structural transition in BSBS down to 3.5 K.

6.3.1.2 Dielectric studies

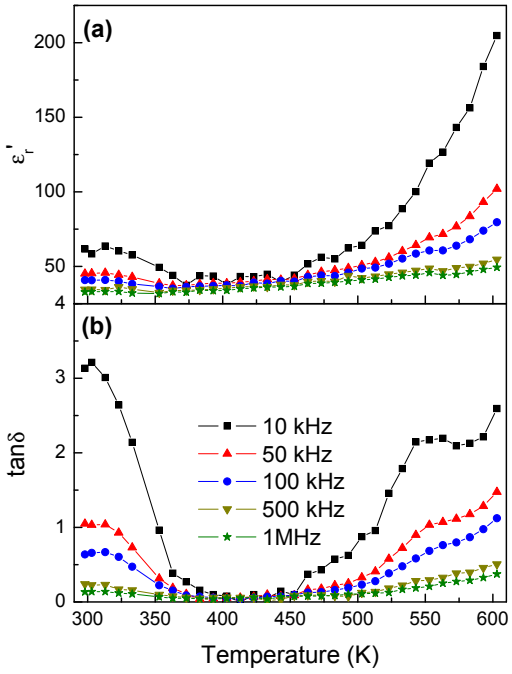

Figure 6.3: Temperature dependence of real part of dielectric response (a) and tangent loss (b) in Ba_2BiSbO_6 at various frequencies.

Figure 6.3 shows the real part of dielectric constant of BBS for various frequencies as a function of temperature. The initial decrease in the curve from room temperature can be attributed to the reported structural change from monoclinic to rhombohedral symmetry around 250 K [123]. However the dielectric change associated with the structural transition from rhombohedral to cubic symmetry is not clear which may be due to the high dc conduction.

The real part of dielectric response of BSBS for various frequencies as a function

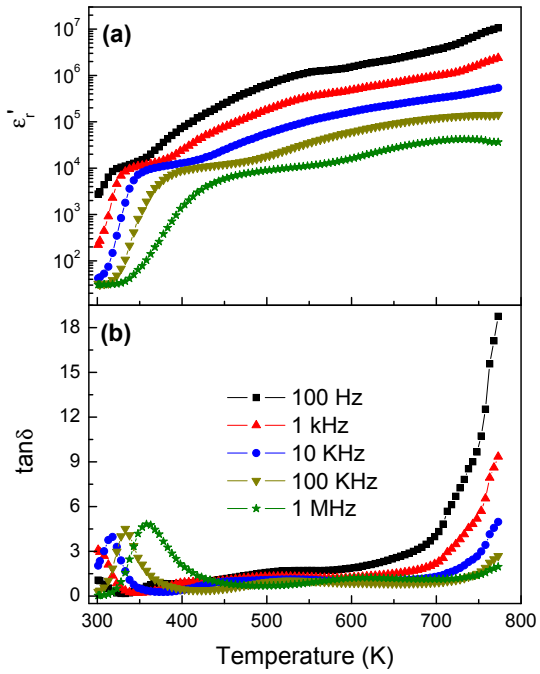

Figure 6.4: Temperaure-dependence of real part of dielectric response (a) and tangent loss (b) of $BaSrBiSbO_6$ at various frequencies.

of temperature is shown in figure 6.4a. The sample shows two dielectric anomalies near 350 K and 600 K which varies with respect to frequency. The anomaly around 350 K may associate with a structural transition from rhombohedral $R\bar{3}$ to cubic $Fm\bar{3}m$ symmetry as BBS was shown to undergo the rhombohedral to cubic structural transition around 515 K [123] and the shift in transition temperature in the present compound may be due to 50 % replacement of Sr-ion. Since the phase transition is continuous in the case of BBO and BBS, the observed dielectric anomaly in the present system is broad in nature. The exponential increase in dielectric constant above 600 K is due to the increase in the dc conduction of the sample. Both the real and imaginary part (not shown here) of the dielectric constant increases with increasing temperature and shows very high value in the order

of 107 at the maximum temperature measured. However, the dielectric loss is very low through out the temperature range (Fig 6.4b). Further, the impedance analysis of the room temperature data using the program *Zview*, showed that capacitance of the grain is in the order of 10^{-11} with a resistance of 0.3 MΩ whereas the grain boundary is in the order of 10^{-9} with the resistance of 0.5 MΩ. This implies that the high dielectric constant observed in the present system may originate due to grain boundary.

6.3.2 Sr_2BiSbO_6

6.3.2.1 Structural analysis

The compound Sr_2BiSbO_6 (SBS) is not reported in the literature to our knowledge. The x-ray powder diffraction pattern recorded on the sample is shown in figure 6.5. The pattern evidenced a perovskite-type structure with the main peak observed for $d_{hkl} \approx 3$ Å corresponding to d_{110} of the perovskite cubic sub-cell. Comparing the pattern to the ones reported for Ba_2BiSbO_6 and $BaSrBiSbO_6$ [122, 127], extra peaks are observed for example at $d \approx 9.6$ Å i.e. $4d_{[111]}$ of the perovskite cubic subcell. In addition to the peaks which could be indexed with a super-cell due to an ordering in the perovskite structure, some reflections correspond to a secondary phase, $SrBi_2O_4$, evidenced by EDS analysis [128].

To evidence the symmetry of the main phase, an ED study was performed at room temperature. The reconstruction of the reciprocal space performed by tilting around the crystallographic axes evidences a tetragonal cell with $a \approx 2a_p\sqrt{2} \approx 11.4$ Å and $c \approx 4a_p \approx 16.8$ ÅṪhe conditions limiting the reflection imply I-type lattice without other condition. So the probable space groups are: I*4* (79), I$\bar{4}$ (82), I*4/m* (87), I*4mm* (107), I$\bar{4}$*m2* (119), I$\bar{4}$*2m* (121) and I*4/mmm* (139). The [010] ED

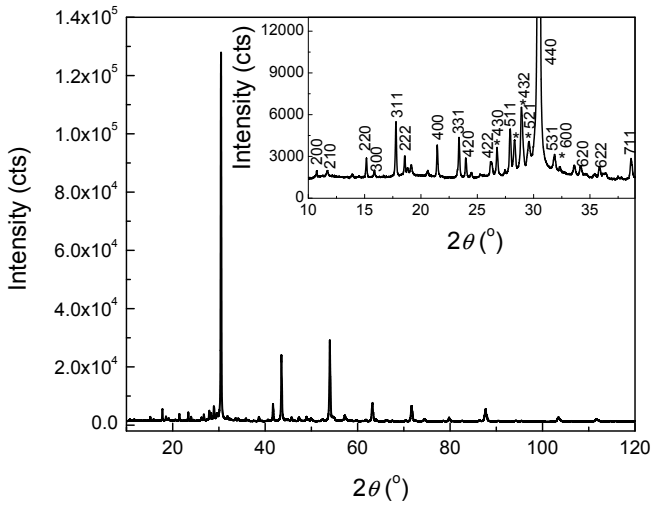

Figure 6.5: Room-temperature x-ray pattern of Sr_2BiSbO_6. Inset shows the pattern indexed assuming a primitive cubic cell and asterisks shows the possible impurity phases.

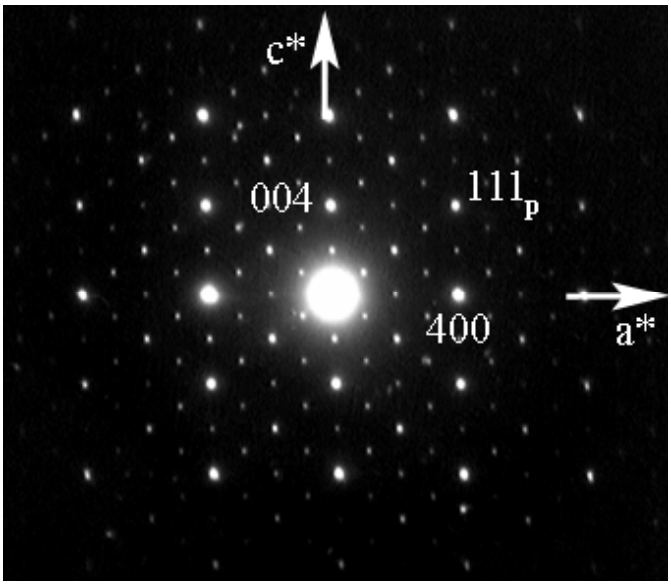

Figure 6.6: [010] ED pattern indexed in the tetragonal cell: $2a_p\sqrt{2} \times 2a_p\sqrt{2} \times 4a_p$ (The subscript p refers to the perovskite cubic sub-cell).

pattern is represented in figure 6.6 in which the subscript p refers to the perovskite cubic sub-cell. The possibility of being a cubic symmetry with $a \approx 16.8$ Å and a F lattice was ruled out due to the observation, on the ED pattern, of a slight

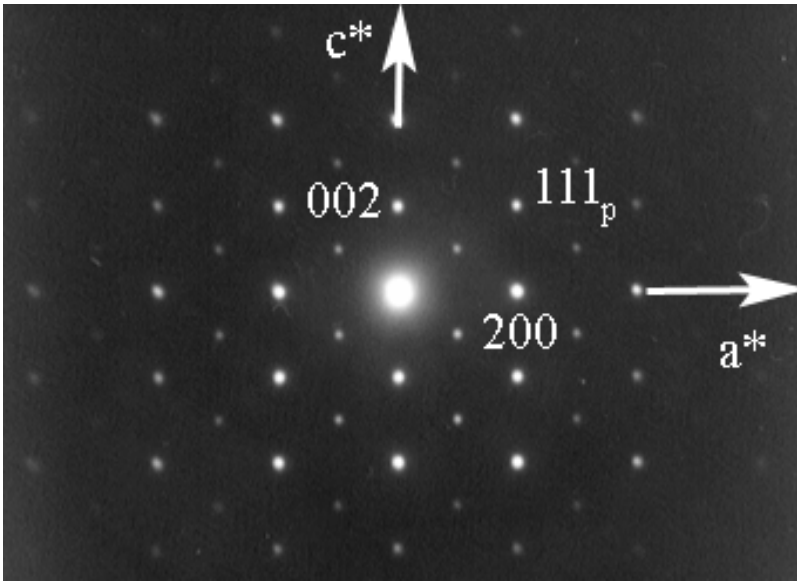

Figure 6.7: [010] ED pattern indexed in the tetragonal cell: $a_p\sqrt{2} \times a_p\sqrt{2} \times 2a_p$.

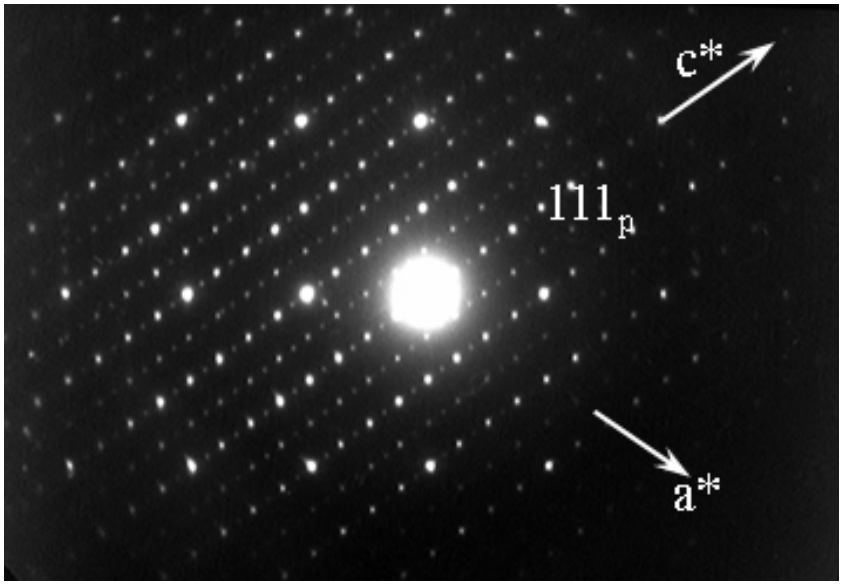

Figure 6.8: [010] ED pattern of the monoclinic supercell implied by extra-spots along $[111]^*_p$. The subscript p refers to the perovskite cubic sub-cell.

difference between d^*_{220} and d^*_{004}. Even if the aforementioned tetragonal super-cell is characteristic of the main phase, other supercells were observed on different crystallites. Some crystallites are characterized by other ordering phenomena implying a smaller tetragonal cell with $a \approx a_p\sqrt{2} \approx 5.9$ Å and c $\approx 2a_p \approx 8.4$ Å and a I

lattice figure 6.7. The last type of ordering found in the sample takes place along the $[111]^*$ direction of the cubic perovskite sub-cell and implies a $d_{hkl} \approx 19.5$ Å which corresponds to $8a_p\sqrt{3}$ (8 times the $d_{[111]}$ distance of the cubic perovskite sub-cell) (Fig. 6.8). A monoclinic supercell can be defined.

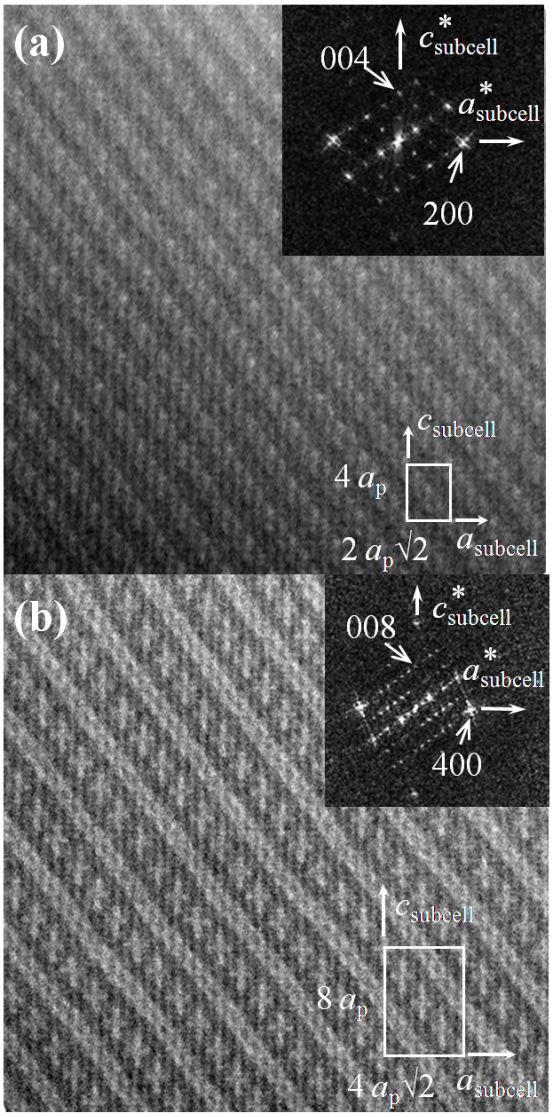

Figure 6.9: HAADF STEM images of Sr_2BiSbO_6: (a) particle presenting an alternation of one bright layer with a darker one along the $[111]^*_p$ direction and (b) another particle showing an alternation of one bright layer with a thicker dark layer along the $[111]^*_p$ direction.

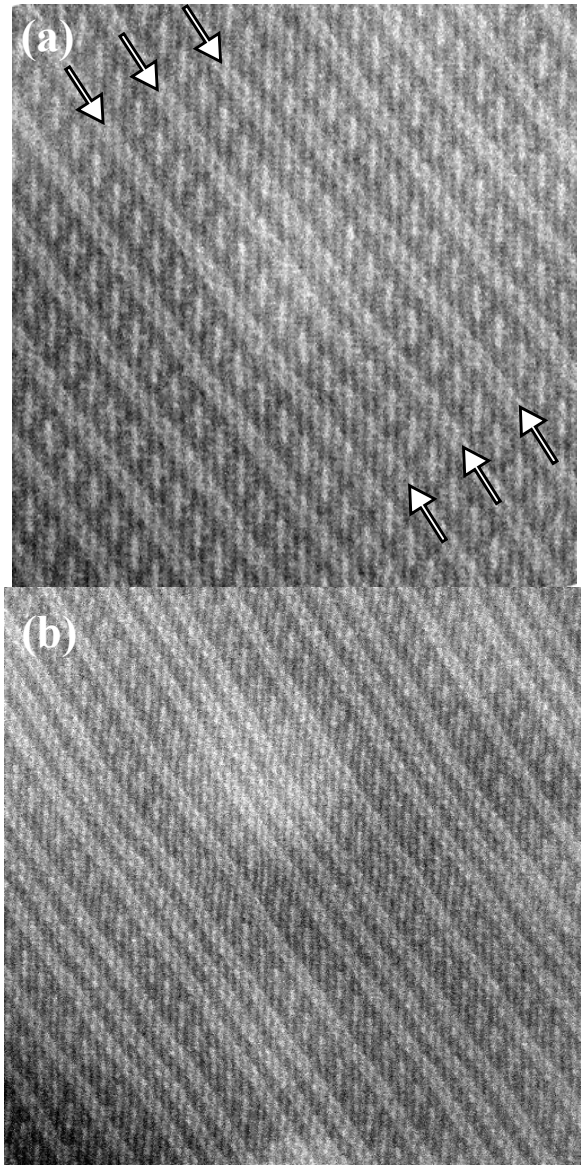

Figure 6.10: HAADF STEM images showing (a) shearing planes and (b) stacking defects in Sr_2BiSbO_6.

High Resolution STEM was performed to obtain Z-contrast images giving important information about the microstructure and eventual structural phenomena. [010]-oriented Z-contrast images are exhibited on figures 6.9 and 6.10. Figure 6.9a and 6.9b are two images recorded on two different particles corresponding to the ED patterns presented on figures 6.6 and 6.8 respectively. On both images are

represented the subcells as well as the FFT's indexed in the quadratique subcell $2a_p\sqrt{2} \times 4a_p$. On figure 6.9a, one can observe a regular stacking of one bright layer with a darker one along the $[111]_p$ direction, corresponding to a first superstructure called 1. This regular alternation is also present on figure 6.9b, but the cationic ordering implies a thicker dark layer in which the disposition of high electron density cations create cross shapes. This second superstructure is called 2. Besides these superstructures, other structural phenomena were pointed out. On figure 6.10a, stacking faults appear on the superstructure 2 as shearing planes, and random alternations between superstructure 1 and 2 along the $[111]_p$ direction are observed on figure 6.10b forming another kind of stacking defects. All theses defects were regularly observed on the different studied crystallites, and sometimes can even co-existed within a same crystallite.

The average cationic composition determined from more than 40 different crystals gave a stoichiometry of $Sr_2Bi_{0.74}Sb_{0.87}$ with high standard deviation for the Bi and Sb contents. The secondary phases observed correspond to the composition close to $(Bi,Sb)_2SrO_x$ with various Bi and Sb contents and a ratio (Bi+Sb)/Sr above 2.

The profile matching on x-ray pattern of SBS was carried out by using the lattice parameters obtained through ED assuming that the system belongs to tetragonal symmetry with the space group I*4/mmm*. Even though ED shows the presence of tetragonal phase with $2a_p\sqrt{2} \times 2a_p\sqrt{2} \times 4a_p$ and $a_p\sqrt{2} \times a_p\sqrt{2} \times 2a_p$, x-ray pattern fitted better with the former rather than the well known $a_p\sqrt{2} \times a_p\sqrt{2} \times 2a_p$ lattice parameters. The refined lattice parameters obtained are $a = b = 11.7859(2)$ and $c = 16.691(1)$ Å for I*4/mmm* symmetry. Figure 6.11 shows the profile matching of Sr_2BiSbO_6 on room-temperature x-ray diffraction data using the aforementioned lattice parameters. The vertical tick mark shows the possible

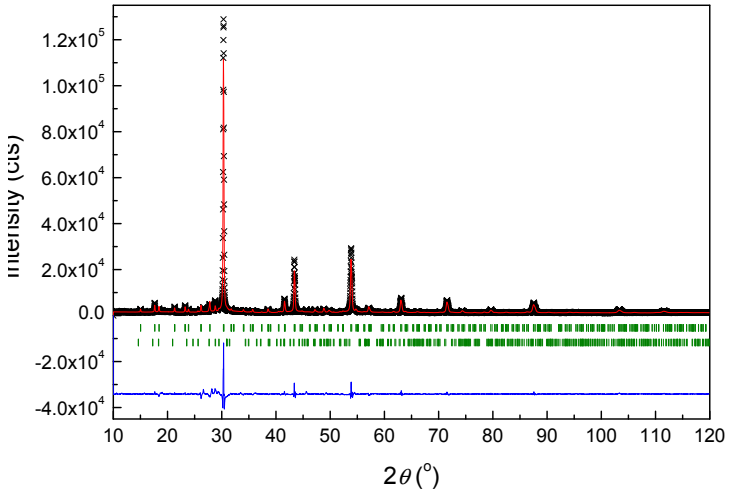

Figure 6.11: Profile analysis of Sr_2BiSbO_6 x-ray pattern including the impurity phase $SrBi_2O_4$.

reflections of the two phases; first row belongs to the main phase Sr_2BiSbO_6 and second row belongs to $SrBi_2O_4$. The cubic subcell value of SBS is compared with other related ordered perovskites in table 6.3. The smaller cubic subcell value of SBS is in agreement with smaller average ionic radii of cations at A and B sites.

To the best of our knowledge, such an ordered structure with $2a_p\sqrt{2} \times 4a_p$ lattice parameter is not known in literature. However there is a report on $Sr(Li_{1/4}Nb_{3/4})O_3$ system which shows a low temperature (T $\leq$ 1300 ^{o}C) polymorph, tentatively, indexed in a = 16.014 Å cubic cell [129]. Further this system has been reported to show two more polymorphs at high temperature by quenching experiments. At T $\geq$ 1400 ^{o}C, it forms a disordered cubic perovskite. Between 1300 and 1400 ^{o}C, it forms a polymorph with monoclinic structure. The ED studies reported that the [111] pattern contains a fourfold superstructure, implying that the layers stacked in the [111] direction have a mixed B-site composition and are ordered or that a layer description is not applicable to this structure.

Table 6.3: Comparison of cubic subcell value of Sr_2BiSbO_6 with other related ordered perovskites.

Composition	Space group	lattice parameters	$\langle r_A \rangle$ (Å)	$\langle r_B \rangle$ (Å)	a_p (Å) cubic lattice of the perovskite subcell	reference
$BaBiO_3$	I*2/m*	a = 6.18505(7) Å, b = 6.13219(7) Å, c = 8.6585 (1) Å, $\beta = 90.229(1)^o$	1.61	0.895	4.373	[123]
Ba_2BiSbO_6	R$\bar{3}$	a = 6.0351(2) Å, $\alpha = 60.202(1)^o$	1.61	0.815	4.268	[127]
$BaSrBiSbO_6$	R$\bar{3}$	a = 5.9809(2) Å, $\alpha = 60.045(2)^o$	1.525	0.815	4.230	[127]
Sr_2BiSbO_6	Tetra. symm.	a = 11.7896(9) Å, c = 16.675(2) Å	1.44	0.815	4.168	This study

Similar quenching experiments were carried out in the present system to stabilize different polymorphs, if any. The samples were inserted directly into the furnace at three different temperatures, 850, 900 and 950 ^{o}C. They were allowed to react for twelve hour and after that it was quenched to room-temperature. The x-ray pattern showed that the ordering exists up to the maximum temperature heated and there were no significant change in the main phase. However the impurity phases are seen to decrease slightly by this quenching experiment compared to the furnace cooled samples.

6.3.2.2 Dielectric studies

Dielectric response (real part) of SBS for various frequencies as a function of temperature is shown in figure 6.12. The sample does not show any dielectric anomalies up to 700 K and at room-temperature, it shows a dielectric constant value of 42

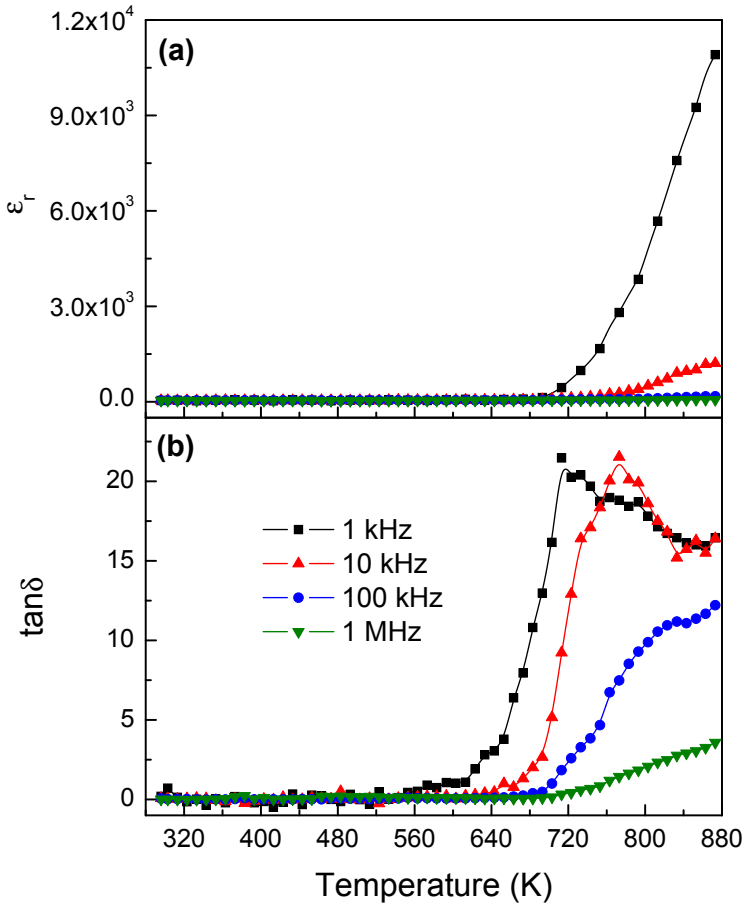

Figure 6.12: Dielectric constant and tanδ as a function of temperature.

for 1 kHz. The increase above 700 K may be due to increase in the dc conduction or belongs to a phase transition which is well known in this ordered structure [123, 127]. The imaginary part (not shown here) of the dielectric constant also shows similar increase above 700 K and reaches a value in the order of 10^5 for a frequency of 1 kHz at the maximum temperature measured which is in one order higher than that of the real part. The tanδ is also increases above 700 K. It is likely that the increase above 700 K can be attributed to dc conduction rather than a phase transition.

6.3.3 $BaBi_{0.7}Nb_{0.3}O_3$

6.3.3.1 Structural analysis

Although our intent was to replace Bi^{5+} ions in $BaBi^{3+}_{0.5}Bi^{5+}_{0.5}O_3$ by Nb^{5+} ions, we could succeed in getting a single phase material only up to 60% substitution. Beyond this limit, $Ba_5Nb_4O_{15}$ appeared as secondary phase. Therefore, we have investigated the material with the composition $BaBi^{3+}_{0.5}(Bi^{5+}_{0.2}Nb^{5+}_{0.3})O_3$. X-ray and neutron diffraction patterns of BBN could not be indexed in the monoclinic structure (I*2/m*) of the parent compound BBO, but they were found to be similar to those of $BaBi_{0.5}Sb_{0.5}O_3$, which has a rhombohedral structure ($R\bar{3}$) at room temperature [123]. It should be mentioned here that the $R\bar{3}$ phase also exists in the parent compound BBO as one of the high-temperature phases [121, 123]. Subsequently, all diffraction lines in both x-ray and neutron diffraction patterns of BBN could be indexed with the rhombohedral symmetry. Further, structural refinement was carried out on the neutron data using the structural model of $BaBi_{0.5}Sb_{0.5}O_3$ [123]. The fitted neutron diffraction pattern obtained at the convergence is shown in figure 6.13.

A good fit with reliable agreement factors (Table 6.4) confirmed that the BBN has rhombohedral structure with $R\bar{3}$ space group. There are two crystallographic sites for B cations, {0,0,0} and {½, ½, ½}. The first one is completely occupied by Bi(I) ions and other one is occupied by Bi(II) and Nb ions. The average bond lengths of Bi(I)-O and Bi(II)/Nb-O are 2.300(3) and 2.052(3) Å, respectively. The different bond lengths can be understood from the difference in ionic radii of Bi^{3+}, Bi^{5+}, and Nb^{5+} ions in octahedral coordination [121]. From the inspection of the bond lengths and a comparison with their corresponding bond lengths for BBO and $BaBi_{0.5}Sb_{0.5}O_3$ (2.29 and 2.11 Å and 2.31 and 2.199 Å, respectively), we

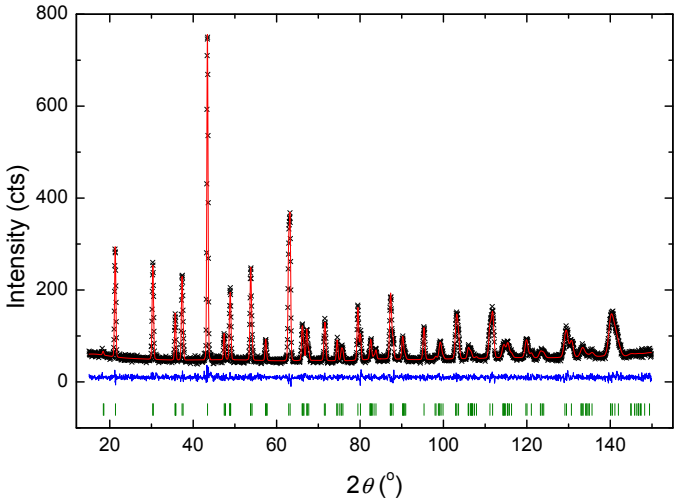

Figure 6.13: Observed, calculated, and difference neutron diffraction pattern of $BaBi^{3+}_{0.5}(Bi^{5+}_{0.2}Nb^{5+}_{0.3})O_3$ at room temperature, fitted in the $R\bar{3}$ space group. Tick marks are the symmetry allowed reflections. Neutron diffraction data were collected using the instrument D2B at ILL, Grenoble, France.

Table 6.4: Structural parameters obtained from the Rietveld refinement of the room temperature neutron diffraction data for $BaBi^{3+}_{0.5}(Bi^{5+}_{0.2}Nb^{5+}_{0.3})O_3$.

$R\bar{3}$ $a = 6.0870(2)$Å and $\alpha = 60.317(1)^o$					
Atoms	x	y	z	N	U_{iso}/U_{11}
Ba	0.2512(8)	0.2512(8)	0.2512(8)	1.00	1.2(6)
Bi(I)	0	0	0	1.00	1.0(1)
Bi(II)	0.5	0.5	0.5	0.54(5)	0.5(1)
Nb	0.5	0.5	0.5	0.46(5)	0.5(1)
O	0.2184(5)	0.3106(4)	0.7338(12)	1.0	2.4(2)
O	U_{22} = 2.8(2)	U_{33} = 3.5(2)	U_{12} = -1.4(1)	U_{13} = -0.6(2)	U_{23} = -0.4(2)
χ^2= 1.2 and R_{wp} = 5.44 %					

suggest that Bi ions occupying the {0,0,0} site are in the trivalent state and those occupying the {½, ½, ½} site are in a pentavalent state. The Bi^{5+} and Nb^{5+} ions are distributed randomly in the {½, ½, ½} site. Although this structural

model, R$\bar{3}$, resulted in reliable agreement factors and structural parameters, we made an attempt to verify the noncentrosymmetric space group R3, a subgroup of R$\bar{3}$, because of the present observation that BBN shows ferroelectricity at room temperature. The refinement gave a fairly good fit ($\chi^2 = 1.25$), but the errors on oxygen positions were at the third decimal with $R_{wp} = 5.58$ % which is slightly higher than that (5.44 %) for R$\bar{3}$. Therefore, we conclude that the space group R$\bar{3}$ better describes the structure of BBN.

This is in agreement with the present observation that substitution of smaller Nb^{5+} ions (0.64 Å) at the Bi^{5+} site in BBO results in the rhombohedral structure at room temperature. It must be emphasized that all these structures are characterized by centrosymmetric space groups.

6.3.3.2 Dielectric studies

Figure 6.14a shows the real part of dielectric response of BBN at various frequencies (100 Hz to 1 MHz) as a function of temperature. It can be seen that the dielectric constant has a broad maximum around 400 ^{o}C, where the value of the dielectric constant is very high, $\sim 7.5 \times 10^6$ for 100 Hz. However, the dielectric constant at room temperature is very low (∼100). The broad maximum in dielectric constant indicates a diffuse phase transition from rhombohedral to cubic. Also, there is a shoulder at around 480 ^{o}C that may result from the disorder at the B-site because of a decrease in the degree of long-range ordering of Bi^{3+} and Bi^{5+} ions at high temperatures. The dielectric maximum decreases drastically with an increase in frequency. Further, the maximum at 400 ^{o}C shifts toward higher temperature with increase of frequency, whereas the maximum at 480 ^{o}C does not change significantly. The imaginary part of dielectric constant also shows a similar broad maximum centered at around 460 ^{o}C as seen in figure 6.14b.

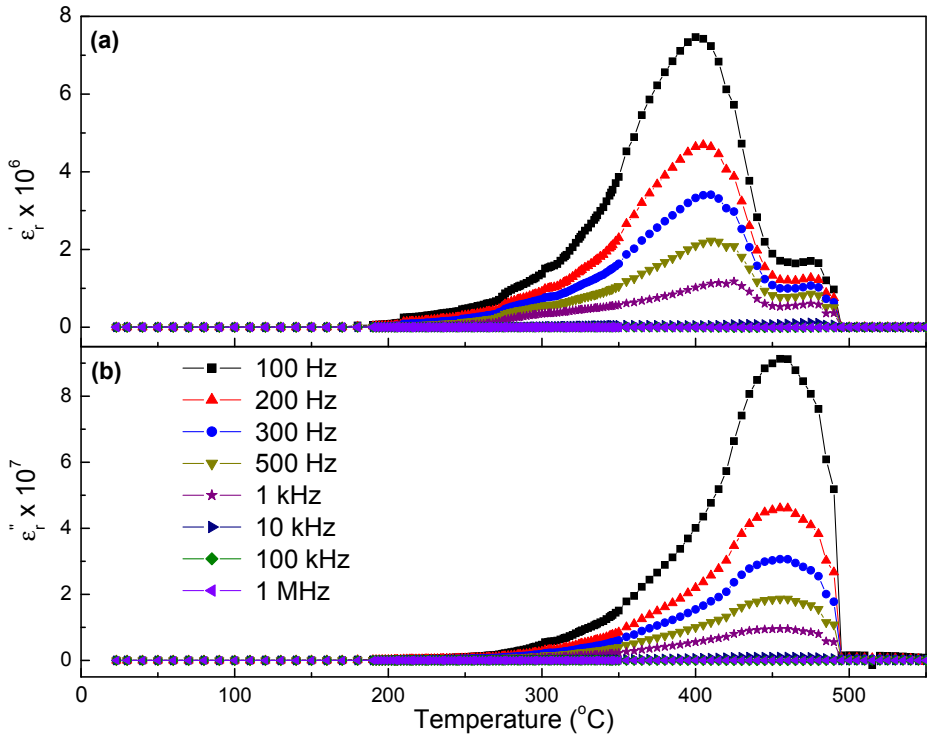

Figure 6.14: Temperature dependence of (a) real and (b) imaginary part of the dielectric constant.

6.3.3.3 Phase transition

Temperature dependence of powder x-ray diffraction showed that there is a structural transition between 450 and 700 ^{o}C (Fig. 6.15). From the inspection of the peak at $2\theta = 52^o$, it appears that the transition occurs continuously, which is consistent with the observed broad dielectric transition. This peak is composed of three reflections (233, 013 and $11\bar{2}$) in the rhombohedral phase, which becomes a single broad peak at 700 ^{o}C. Considering that the broadening of this peak is caused by the high temperature, it can be indexed as a 422 reflection in the F$m\bar{3}m$ cubic phase, as already reported in BBO and $BaBi_{0.5}Sb_{0.5}O_3$, where the rhombohedral (R$\bar{3}$) phase transforms to high-temperature cubic (F$m\bar{3}m$) structure [123]. To confirm that the high-temperature phase is cubic, we performed Rietveld refinement

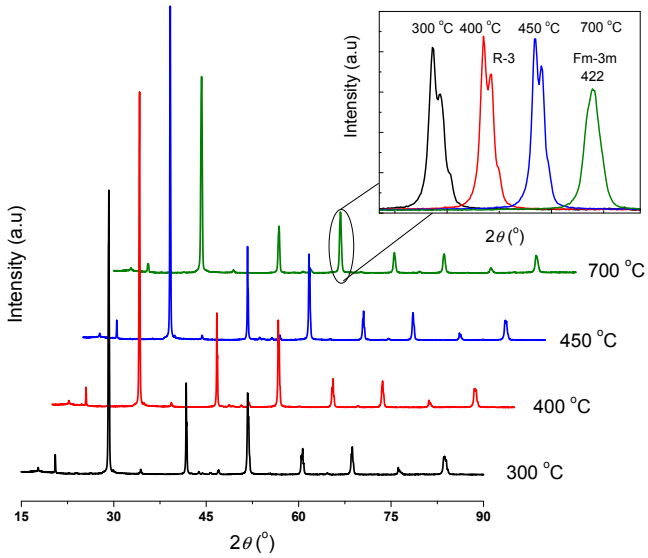

Figure 6.15: Powder x-ray diffraction patterns at higher temperatures indicating the phase transition. The peak at $2\theta = 52^o$, which corresponds to [422] reflection in the cubic phase, is expanded in the inset. The peak positions have been shifted with the same overall scale (5^o two theta). Except for the broadening due to high temperature, the peak splitting disappears between 450 ^{o}C 700 ^{o}C.

using the program Fullprof [130]. This gave a good fit to the data ($\chi^2 = 3.76$) with $R_{Bragg} = 5.0$ %. Because the temperature dependence of the dielectric constant exhibits a very broad transition with a shoulder at $\sim$ 480 ^{o}C and because of the absence of XRD data between 450 and 700 ^{o}C, it would be difficult to infer the exact temperature at which the structural transition occurs.

6.3.3.4 Pressure dependent phase transition

Energy-dispersive x-ray diffraction spectra (EDXD) under various pressures were collected at the B1 station of the Cornell High Energy Synchrotron Source (CHESS). The powdered sample of BBN was loaded into a diamond anvil cell with a tip of 500 μm, using stainless steel T 301 gasket. The pressure measurement was done using ruby fluorescence technique [131, 132]. Using Au foil, the diffraction angle was determined. All EDXD spectra were acquired at Ed = 47.539 $\pm$ 0.009 keV Å.

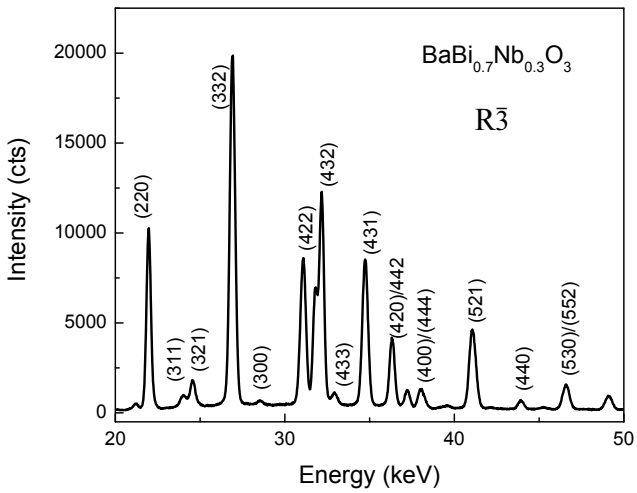

Figure 6.16: EDXD spectrum of $BaBi_{0.7}Nb_{0.3}O_3$ at ambient pressure and temperature.

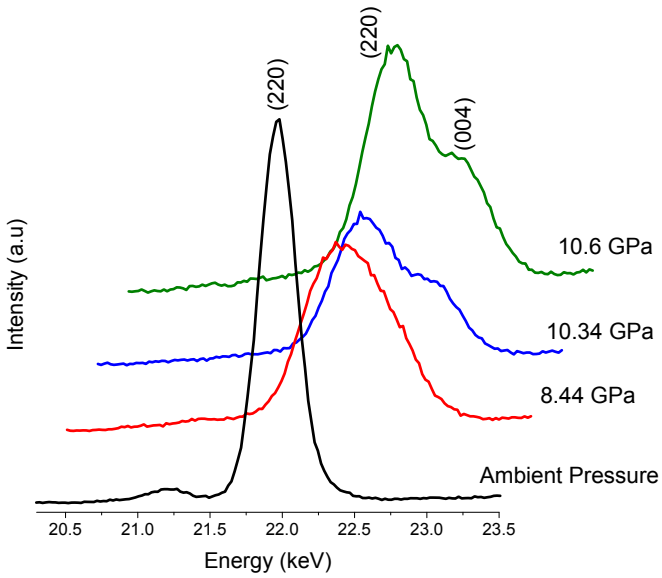

Figure 6.17: Pressure dependent EDXD spectra of 22 keV peak showing the phase transition.

X-ray diffraction spectra were analyzed by line profile fitting and lattice parameter refinements using the program XRDA [133, 134].

EDXD spectra of BBN are collected in the pressure range of 0 to 15 GPa at room temperature. Figure 6.16 shows the EDXD spectra at ambient pressure and

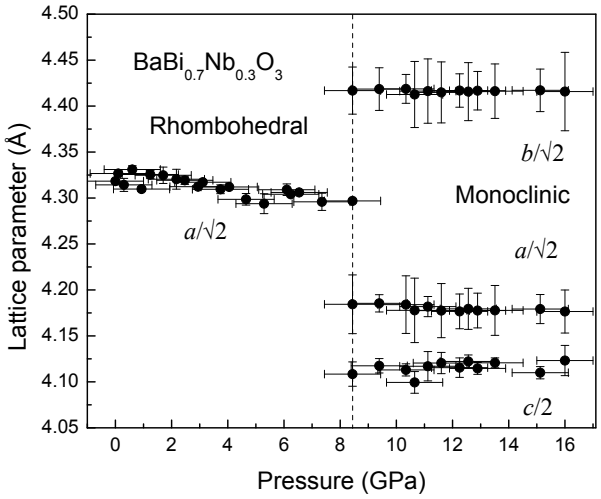

Figure 6.18: Reduced cell parameters obtained by indexing the peaks as a function of pressure.

temperature. The spectrum is consistent with the laboratory x-ray diffraction data. The peaks obtained in EDXD spectra are fitted with the lorentzian line profiles with a linear background. For indexing, the Ed = 47.539 ± 0.009 keV Å was used. The rhombohedral cell parameters and their atomic position obtained after refinement on the neutron data of BBN were taken as the initial fit parameters. In the high pressure phase, the monoclinic cell parameters and corresponding atomic positions were given based on the BBS structure [123]. The refined cell parameters obtained for rhombohedral phase at ambient pressure are $a = 6.109(2)$ Å and $\alpha = 60.3(1)^o$.

From the inspection of the peak at 22 keV as a function of pressure (Fig. 6.17), we suggest that BBN undergoes a transition from the ambient pressure rhombohedral phase ($R\bar{3}$) to monoclinic phase ($I2/m$) at 8.44 GPa. At ambient pressure, this peak is composed of (220) reflection where as at 8.44 GPa the peak splits, as shown in the figure 6.17, which can be indexed with (220) and (004) reflections. This confirms the occurrence of phase transition at 8.44 GPa from $R\bar{3}$ to $I2/m$.

Similarly, the peak composed of (112) and reflections of rhombohedral phase transforms to monoclinic phase having (020), (11$\bar{2}$), (112) and (200) reflections. The reduced cell parameters obtained by indexing the peaks as a function of pressure is shown in the figure 6.18. The discontinuous change in the cell parameter shows that the phase transition is first order in nature which is in agreement with BBS and BBO [123]. The pressure dependent study up to 15 GPa shows no evidence for the formation of primitive monoclinic structure with $P2_1/m$ space group and retains the monoclinic I*2/m* symmetry up to 15 GPa in the hitherto system due to the replacement of Bi^{5+} ions by smaller Nb^{5+} (r = 0.64 Å) ions [121]. This is consistent with observation in the case of BBS and is associated with the replacement of Bi^{5+} ions with smaller pentavalent ion [123, 126]. The refined cell parameters obtained for the monoclinic phase, I*2/m*, are a = 5.91(2) Å, b = 6.25(3) Å and c = 8.22(1) Å with monoclinic angle, $\beta = 88(1)^o$ at 15 GPa.

6.3.4 Polarization - Electric field loop

The polarization with respect to electric field curve of $BaBi_{0.7}Nb_{0.3}O_3$ after an electric poling is shown in figure 6.19. The samples Ba_2BiSbO_6, $BaSrBiSbO_6$ and Sr_2BiSbO_6 also show a similar loop. We believed that these compounds are ferroelectric assuming that there may be local non-centrosymmetric even though the compound shows average centrosymmetric structure.

Meanwhile it was explicitly shown that the cigar shaped loop originates from the leakage behavior of the material by comparing with polarization-electric field (P-E) measurements carried out on the skin of a banana [135]. The analysis of artifacts arise in the P-E measurements for the ferroelectric material are important in order to use in technological applications [136, 137]. The switching charge (Q) measured

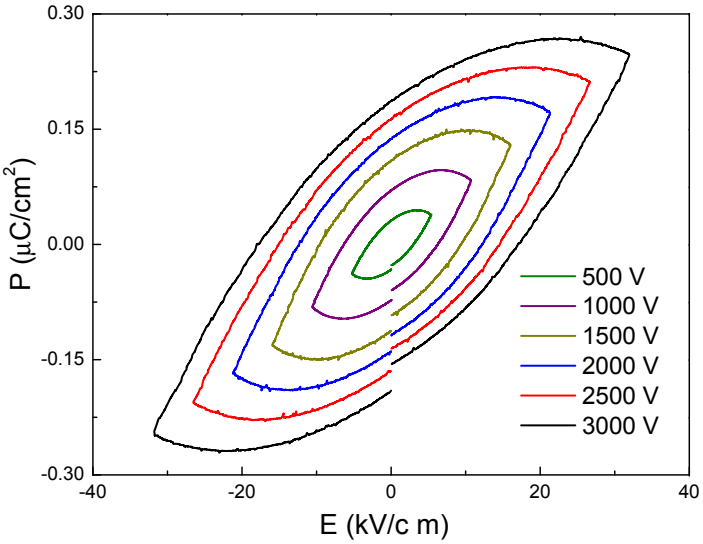

Figure 6.19: Room-temperature P-E loop measured at various driving voltages at 1 kHz.

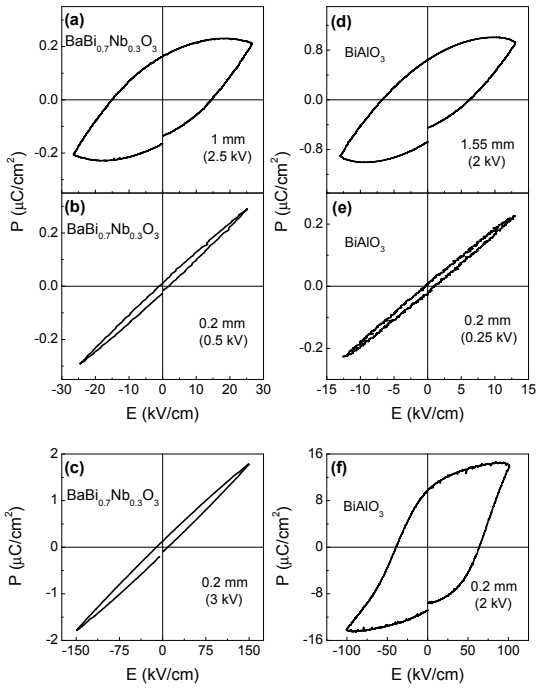

Figure 6.20: Room-temperature P-E loop of $BaBi_{0.7}Nb_{0.3}O_3$ and $BiAlO_3$ with different pellet thickness and applied electric field.

in P-E measurement will have contribution from the remanent polarization (P_r) and electrical conductivity [135]. In lossy dielectric materials, the electrical conductivity will lead to the cigar shaped loop. This made us to reinvestigate our results on $BaBi_{0.7}Nb_{0.3}O_3$ (BBN) published earlier [138].

Previously we have reported that BBN is ferroelectric by showing a P-E loop similar to cigar-shaped loop. The P-E loop reported was measured for BBN ceramic pellet of thickness around 1 mm (Fig. 6.20a). Thus the electric field applied for the pellet is low even though the driving voltage is 3 kV. In a capacitor, the electric field applied is inversely proportional to the thickness of the medium between the two electrodes. To increase the electric field applied to the material, the pellet was thinned to 0.2 mm thickness. P-E measurement was carried out in silicone oil bath in order avoid the short between the two electrodes at higher voltage. For a voltage of 250 kV at a frequency 1kHz, BBN pellet shows a linear P-E loop (Fig. 6.20b) rather than the cigar shaped loop observed for the same material of higher thickness. Further P-E measurement at a high applied electric field for 0.2 mm BBN pellet gives the same linear P-E loop (Fig. 6.20c).

For further comparison, the results obtained from similar measurements carried out in $BiAlO_3$ (BAO) are discussed below. BAO has been reported to be a ferroelectric material [120] as discussed in chapter 3. Here the P-E measurements carried out for BAO pellets of thickness 1.55 mm and 0.2 mm are shown in figure 6.20d-f. For 1.55 mm thick BAO pellet, the observed P-E loop shape are similar to that observed for 1mm BBN pellet (Fig. 6.20d). Similar to BBN, the shape changes from cigar shape to linear loop by reducing the thickness of the BAO pellet measured (Fig. 6.20e). At a high applied field (above the coercive field), BAO shows the hysteresis loop typical of a ferroelectric (Fig. 6.20f). It is known in literature that the switching charge directly proportional to the electrical conduc-

tivity contribution [135]. However we observe that by decreasing pellet thickness, the contribution due to electrical conductivity decreases which is not known in the literature to our best knowledge. It is also important to mention that the area inside the cigar shape loop also changes depending upon the frequency used in P-E measurements as the artifacts due to leakage are highly frequency dependent [137].

Hence BBN and other ordered compounds described in this chapter are not ferroelectric materials. The cigar shaped loop observed is due to the electrical conductance with higher thickness of the measured pellet. Further the symmetric Bi-O bonds indicates that the Bi^{3+}:$6s^2$ lone pair is stereochemically inactive in these ordered perovskites similar to the cubic PbS, forming a NaCl type lattice with perfectly symmetric lead sites [118]. The non ferroelectric nature is in agreement with the fact that the compounds are centrosymmetric [138] even though an ambiguity exists in symmetry of the parent compound $BaBiO_3$ [116, 117].

6.4 Conclusions

Ba_2BiSbO_6, $BaSrBiSbO_6$ and $BaBi_{0.7}Nb_{0.3}O_3$ have been confirmed to exhibit centrosymmetric rhombohedral structure with the space group $R\bar{3}$ based on the analysis of powder neutron diffraction data. BBS shows a dielectric anomaly near room temperature which may be attributed to $I2/m$ - $R\bar{3}$ structural transition at 250 K. The dielectric measurement of BSBS shows an anomaly near 350 K that may be related with the structural transition from rhombohedral $R\bar{3}$ to cubic $Fm\bar{3}m$ symmetry. Further the low temperature structural analysis indicates that the structure remains in rhombohedral symmetry down to 3.5 K. High temperature x-ray diffraction studies on $BaBi_{0.7}Nb_{0.3}O_3$ shows a phase transition from rhombohedral to cubic structure and a dielectric anomaly near this transition. BBN also shows

a phase transition from ambient rhombohedral to a monoclinic structure (I$2/m$) at 8.44 GPa based on the pressure-dependent EDXD studies. However these ordered compounds are not ferroelectric as the Bi-O bonds are symmetric indicating that the Bi^{3+}:$6s^2$ lone pair is not stereochemically active. The new compound Sr_2BiSbO_6 has an unusual ordering. ED analysis shows that the compound has tetragonal symmetry with I lattice. The possible lattice parameters are $2a_p\sqrt{2} \times 2a_p\sqrt{2} \times 4a_p$ and $a_p\sqrt{2} \times a_p\sqrt{2} \times 2a_p$. However, x-ray pattern fitted better with the former rather than the well known $a_p\sqrt{2} \times a_p\sqrt{2} \times 2a_p$ lattice parameters.

CHAPTER 7

Structural and magnetic properties of a perovskite manganate, cobaltate and ruthenate**

7.1 Ferromagnetism in perovskite oxides

Perovskites are generally metal oxides with the formula ABO_3, where A is a larger alkaline, alkaline earth or rare-earth cation and B is a small transition metal cation. In the perovskite structure, the B-site cation resides in the interstitial site of an octahedron of oxygen anions and the perovskite unit cell is built from corner-sharing $BO_{6/2}$ octahedra that are connected through B-O-B linkages. The A-site cation fits in the large cavity at the center of eight corner-sharing $BO_{6/2}$ octahedra. Depending on the choice and stoichiometry of the A and B-site cations, perovskites and layered perovskites can possess a wide variety of interesting properties including superconductivity, colossal magnetoresistance, ferroelectricity and catalytic activity.[111]

In a cubic perovskite structure, A ions occupy the corners of the cube, B ions occupy the body centre and O ions occupy the face-centre of the cube. The stability of the perovskite structure is characterized by the so-called Goldschmidt tolerance factor $f = (\langle r_A \rangle + r_O)/\sqrt{2}(\langle r_B \rangle + r_O)$, where r_A, r_B, r_O are radii of the A, B and oxygen ions respectively, represents the averaged ionic size of each element and f

Paper based on this work has been published in *J. Chem. Sci.* **118 (2006) 99; *Solid state commun.* **146** (2008) 110; *Mater. Res. Bull.* (2009) **In press**.

is close to 1, for the cubic perovskite structure.

Magnetism is an interesting field of research in the perovskite oxides. Further these oxides also possess magnetoresistive behavior. This chapter encompass the investigations carried out on ferromagnetic perovskites, namely, $La_{0.7-x}Ce_xBa_{0.3}MnO_3$, $Sr_{0.9}Ce_{0.1}CoO_{2.85}$ and $SrRu_{1-x}Cu_xO_3$.

Perovskite manganates of the type $R_{1-x}A_xMnO_3$ (where R is the rare-earth ion, such as, La, Nd, Pr, etc. and A is the divalent alkaline earth ion such as, Ca, Sr, Ba, Pb, etc.) have recently come into focus on account of the discovery of their magnetoresistance property [139, 140], though they have been studied for almost 50 years before [141].

When average radii of A-site cations or equivalently f decreases, the lattice structure transforms to rhombohedral ($0.96 < f < 1$) and then to orthorhombic structure ($f < 0.96$), in which the Mn-O-Mn bond angle is bent and deviates from 180^o. At finite doping of the divalent alkaline earth ions at the A-site, the charge balance is maintained by a fraction x of Mn^{4+} (d^3) ions distributed randomly throughout the crystal, with the reminder in the Mn^{3+} (d^4) state.

The origin of magnetism and magnetorestivity in doped manganate, $La_{0.7}Ba_{0.3}MnO_3$, may be understood on the basis of double exchange interaction between Mn^{3+} and Mn^{4+} ions [142–144]. The 'double exchange mechanism' proposed by Zener (1951), which remains at the core of the understanding of magnetic oxides, provides an explanation for the interplay between the magnetic and transport properties of the manganates for $0.2 \leq x \leq 0.4$ [142]. This occurs indirectly by means of spin coupling of mobile electrons which travel from one ion (Mn^{3+}) to the next (Mn^{4+}). The physically relevant electrons in manganates are those from the Mn $3d$ levels, which are split by the octahedral crystal field due to the O^{2-} ligands into low-lying triply degenerate t_{2g} (d_{xy}, d_{yz}, d_{zx}) levels and doubly degenerate e_g

($d_{x^2-y^2}$, d_{Z^2}) levels. In the case of the end member $RMnO_3$, Mn^{3+} ($3d^4$) ion, a strong Hund's coupling aligns the four electrons in the active shell; three electrons populate the t_{2g} orbitals while one electron occupies the e_g orbitals. The hopping motions of the electrons are prohibited by the Mott correlation effect.

When the manganates are doped with divalent alkaline earth ions, Mn^{4+} ($3d^3$) ions with only three t_{2g} electrons are formed. They represent holes in the Mn $3d$ band. The t_{2g} electrons are mainly localized, whereas the e_g electrons are mobile and use the O $2p$ orbitals as a bridge between Mn ions. As a consequence, whenever an Mn^{3+} and an Mn^{4+} ion are separated by an O^{2-} ion there is a possibility for the extra electron of the Mn^{3+} ion to hop to the Mn^{4+} ion via the O^{2-} ion. This charge motion is favoured only when core t_{2g} spins of Mn^{3+} and Mn^{4+} ions are coupled ferromagnetically.

The physics of the CMR manganates is more complex than it appears. Though the double exchange mechanism could describe the observed magnetic and electrical properties of manganates for the compositions $0.2 \leq x \leq 0.4$, the values of MR, the existence of ferromagnetic metallic (FMM) and ferromagnetic insulating (FMI) phases [145], the magnetic field-induced structural transitions and charge ordering/antiferromagnetic properties of $x \geq 0.5$ [146] have not been explained by it. There are other interactions, for example, electron-lattice interaction, antiferromagnetic superexchange interaction between the t_{2g} local spins, inter-site exchange interaction between the e_g orbitals (orbital ordering tendency) intra-site and inter-site Coulomb repulsion interactions among the e_g electrons etc., which compete with the ferromagnetic double exchange interaction. The electron-phonon coupling arising from the strong Jahn-Teller coupling is also proved to be important to understand the physics of manganates [19].

On other hand, the ferromagnetism observed in metals like Fe, Co and Ni

and oxides like $SrCoO_3$ and $SrRuO_3$ has been attributed to the collective-electron magnetism or band magnetism rather than due to the mechanisms described above for manganates.

Even though the localized moment theory explained the temperature dependence of the spontaneous magnetization and the existence of a phase transition to a paramagnetic state, it breaks down in one important aspect - it is unable to account for the measured values of the magnetic moment per atom in some ferromagnetic materials, particularly in ferromagnetic metals. The discrepancies such as, the observation of different magnetic moments per atom or ion in ferromagnetic and paramagnetic phases and non-integral number of electrons per atom or ion, were not explained by localized moment theory. These discrepancies were explained by the band theory or collective electron theory.

In the elemental ferromagnetic transition metals, Fe, Ni and Co, the Fermi energy lies in a region of overlapping $3d$ and $4s$ bands. As a result of overlap, the valence electrons partially occupy the $3d$ and $4s$ band. The $4s$ band is broad, with a low density of states at the Fermi level. Consequently, the energy would be required to promote a $4s$ electron into a vacant state, so that it could reverse its spin, is more than that which would be gained by the resulting decrease in exchange energy. By contrast, the $3d$ band is narrow and has a much higher density of states at the Fermi level. The large number of electrons near the Fermi level reduces the band energy required to reverse a spin, and the exchange effect dominates. If the Fermi energy lies within the $3d$ band, then the displacement will lead to more electrons of the low energy spin direction and hence a spontaneous magnetic moment in the ground state.

7.2 Synthesis, structure and properties of $La_{0.7-x}Ce_xBa_{0.3}MnO_3$ (x = 0.0-0.4)

7.2.1 Introduction

Doped rare earth manganese oxides $R_{1-x}A_xMnO_3$ (R = trivalent rare earth: A = divalent alkaline earth) with perovskite structure have been one of the subjects of intensive research in condensed matter because they exhibit very interesting properties such as colossal magnetoresistance (CMR), charge, orbital and spin ordering [19, 141, 147]. The origin of CMR effect in these doped manganates may be understood on the basis of double exchange interaction between Mn^{3+} and Mn^{4+} ions and charge-spin-lattice coupling [142–144]. Large number of materials with various rare earth elements including those containing $4f$ local moments have been investigated. We were interested in studying the effect of substitution of cerium at the A-site because of the fact that the cerium can exist in tri-, tetra and mixed valence state and thereby influence the structure and properties. We have found that the Ce-ions exist in trivalent state in Sr-containing manganates [148, 149]. On the other hand, it has been reported that in calcium containing $Ca_{0.9}Ce_{0.1}MnO_3$ the Ce-ions are in tetravalent state [150]. Interestingly, we found that substitution of cerium leads to a Kondo-like effect in a large band width material (W) $Pr_{0.1}Ce_{0.4}Sr_{0.5}MnO_3$ [148]. In this system the Mn-moments undergo a ferromagnetic ordering at 250 K due to DE interactions, and Ce moments order antiferromagnetically with respect to Mn moments below T $\sim$ 120 K. The electrical resistivity increases anomalously with decrease in temperature, particularly below the Curie temperature T_C, exhibiting a resistivity maximum at 120 K (T_{max}), which corresponds to the ordering of Ce moments, and a minimum at 15 K (T_{min}). The anomalous temperature depen-

dence of resistivity ρ(T) is in contrast to the expected metallic behavior below T_C due to DE interactions. Similar results were reported for $La_{0.1}Ce_{0.4}Sr_{0.5}MnO_3$ with the ferromagnetic ordering of Mn-moments at TC 280 K and Ce ordering below T ∼130 K [149]. In these systems with larger W, since there is no charge ordering of manganese ions and the Mn-sublattice remains ferromagnetic down to 1.8 K, the resistivity anomaly has been attributed to Kondo-like scattering of Mn:e_g conduction electrons by the localized Ce:4f moments. The decrease of resistivity below T_{max} or cerium ordering temperature is due to reduced spin dependent scattering.

In this report, we present the results on the effect of cerium substitution in Ba-containing $La_{0.7-x}Ce_xBa_{0.3}MnO_3$. It is well known that the perovskite $BaCeO_3$ is thermodynamically stable phase. For this reason we chose a ferromagnetic composition with low concentration of barium i.e. a substitution level of 30 %. The results of magnetic and magnetotransport properties are very much similar to that observed in cerium substituted Sr-containing compounds as discussed above.

7.2.2 Experimental

Polycrystalline samples of $La_{0.7-x}Ce_xBa_{0.3}MnO_3$ (x = 0 - 0.4) were prepared by calcinations of stoichiometric mixtures of La_2O_3, CeO_2, $BaCO_3$, Mn_2O_3 at 1100 ^{o}C and sintering at 1500 ^{o}C. Phase purity and structural analysis were carried out with powder x-ray diffraction (XRD) data by Rietveld analysis method using the program Fullprof [44]. Morphology and grain size were analyzed by Scanning Electron Microscope. Magnetization measurements were carried out with a vibrating sample magnetometer in Physical Property Measuring System (PPMS, Quantum Design, USA). Magnetoresistance measurements were done by a standard four-probe method with PPMS by an applied field of 7 T.

7.2.3 Results and discussion

7.2.3.1 Structural analysis

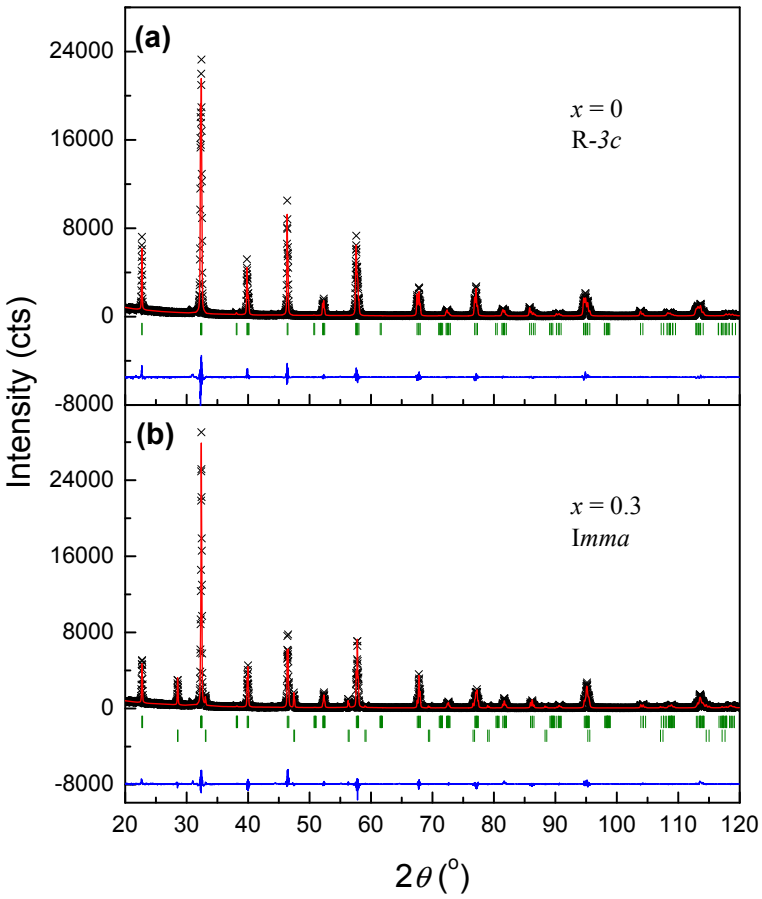

Figure 7.1: Observed, calculated and difference x-ray diffraction patters of $La_{0.7-x}Ce_xBa_{0.3}MnO_3$ ($x = 0$ and $x = 0.3$). Vertical tick marks are symmetry allowed reflections and the second row corresponds to the CeO_2 secondary phase.

For $x = 0$, the structure is consistent with rhombohedral system (space group $R\bar{3}c$) as already reported [151]. The structure remains rhombohedral up to $x = 0.2$ and for $x = 0.3$ and 0.4, it could be described by an orthorhombic phase with the space group I*mma* as expected from the analysis of octahedral distortion as a

Table 7.1: Structural parameters of $La_{0.7-x}Ce_xBa_{0.3}MnO_3$ (x = 0.0 and 0.3).

Parameter	$x = 0.0$	$x = 0.3$
Space group	$R\bar{3}c$	I*mma*
a (Å)	5.5470(1)	5.5221(1)
b (Å)	-	7.8044(2)
c (Å)	13.5001(3)	5.5443 (1)
V (Å^3)	359.75(1)	238.94(1)
La/Ce/Ba: x, y, z	0, 0, ¼	0, ¼, - 0.000(1)
B	0.17(1)	0.16(2)
Mn: x, y, z	0, 0, 0	0, 0, ½
B	0.01(3)	0.06(4)
O(1): x, y, z	0.460(1), 0, ¼	½, ¼, 0.041(5)
O(2): x, y, z	-	¼, 0.019(3), ¾
χ^2	3.83	5.54
Bragg R (%)	3.81	6.30

function of A-site cation [152]. In all the cerium substituted samples, a secondary phase of unreacted CeO_2 phase was present. In addition, in the case of $x = 0.4$, a small amount of $BaCeO_3$ phase could be seen as expected. These phases were included in the refinement as secondary phases. The observed, calculated and difference XRD patterns, for $x = 0.0$ and 0.3, obtained from the Rietveld refinement are shown in figure 7.1. Vertical tick marks are symmetry allowed reflections. The first row belongs to the main phase and the second one is due to CeO_2 impurity phase. The structural parameters for $x = 0.1$ and 0.3 are given in table 7.1.

7.2.3.2 Magnetic properties

Temperature dependence of magnetic susceptibility (χ) measured at 0.01 T by a field cooling process is shown in figure 7.2. From this figure we can see that all the samples show ferromagnetic transition above 300 K. For $x = 0.1$, the transition

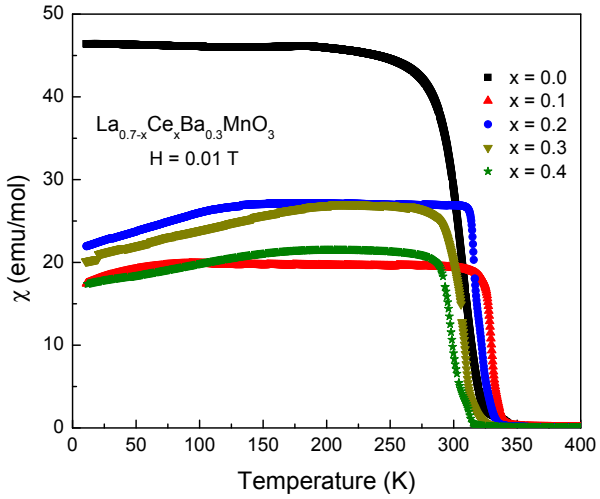

Figure 7.2: Variation in magnetic susceptibility, measured at 0.01 T in field cooled process, for various x in $La_{0.7-x}Ce_xBa_{0.3}MnO_3$ as a function of temperature.

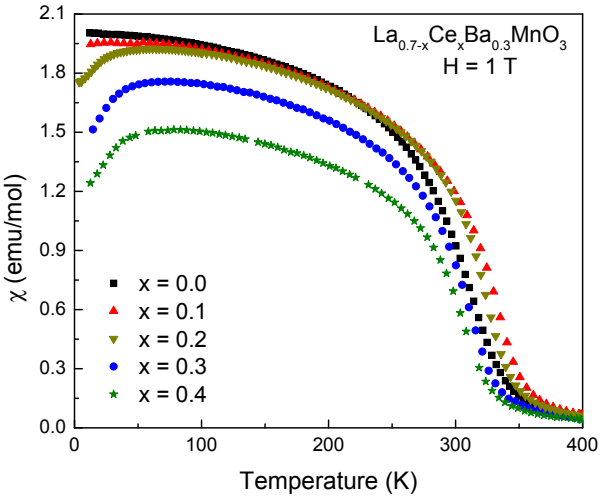

Figure 7.3: Variation in magnetic susceptibility, measured at 1.0 T in field cooled process, for various x in $La_{0.7-x}Ce_xBa_{0.3}MnO_3$ as a function of temperature.

temperature has increased to ∼340 K from ∼320 K for $x = 0$. Further increase of x leads to decrease of T_C which is consistent with the fact that the bigger La^{3+} ions are substituted by smaller Ce^{3+} ions which results in the reduction of one electron

band width W. For $x = 0.1$, the temperature dependence of susceptibility shows a tendency to decrease below ∼200 K. In fact, a clear decrease of susceptibility at low temperatures (< 50 K) can be seen from the susceptibility data measured at 1 T as shown in figure 7.3. This indicates an antiferromagnetic coupling between the ferromagnetic Mn-moments and Ce-moment as observed in the system $La_{0.1}Ce_{0.4}Sr_{0.5}MnO_3$. Above the ferromagnetic transition temperature, the susceptibility of all the samples follows the Curie-Weiss behavior. The effective magnetic moment derived from the Curie-Weiss fit is larger (5.18 - 5.40 μ_B) than the expected (∼4.59 μ_B) for 30 % hole doping. The observed higher values of magnetic moment may indicate the presence of short range ferromagnetic interactions above Curie temperature. Values of θ_P, the paramagnetic intercept obtained from the fit are consistent with the observed variation of T_C with x as shown in table 7.2.

Table 7.2: Variation of T_C, θ_P and particle size with x in $La_{0.7-x}Ce_xBa_{0.3}MnO_3$.

x	0.0	0.1	0.2	0.3	0.4
T_C (K)	327	340	330	319	312
θ_P (K)	324	335	328	317	309
Particle size (μm)	0.3708	0.4595	0.4593	0.5396	0.5815

7.2.3.3 Resistivity

Temperature dependence of resistivity ρ(T) measured under zero applied field is shown in figure 7.4. The ρ(T) behavior is similar to that observed in $La_{0.5-x}Ce_xSr_{0.5}MnO_3$ [149]. Just above 300 K, all samples show a peak which corresponds to ferromagnetic transition temperature that is consistent with the susceptibility measurements as discussed above. The increase of resistivity with decrease of temperature above T_C is believed to be due to large ionic size mismatch at the A-site [153]. For higher

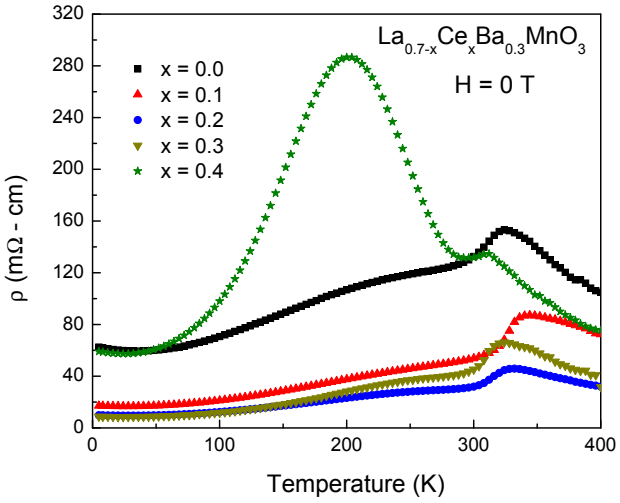

Figure 7.4: Temperature dependence of resistivity under zero applied field for various x in $La_{0.7-x}Ce_xBa_{0.3}MnO_3$. The peak around 200 K in $x = 0.4$ indictes the ordering tempreature of cerium moments.

cerium concentration ($x = 0.4$) there is a second resistivity maximum around 200 K which is related to an antiferromagnetic ordering of cerium moments with respect to Mn-moments. This peak cannot be attributed to ionic size mismatch because the size difference between La^{3+} (1.216 $\AA$) and Ce^{3+} (1.196 $\AA$)[121] is very small and there is an evidence for an antiferromagnetic ordering as inferred from the susceptibility data measured at 1 T as shown in figure 7.3.

The scattering of Mn-e_g electrons by the localized Ce-4f moments is clear from the large negative magnetoresistance (MR = [ρ(7 T) - ρ(0 T)]/ ρ(0 T)) observed for $x = 0.4$ in the vicinity of 200 K as shown in figure 7.5. All samples show large magnetoresistance above room temperature due to double exchange ferromagnetism. At low temperatures < 10 K, the magnetoresistance for $x = 0$ may arise from electron tunneling between the grain boundaries. With increase of x up to 0.3, the MR decreases. This is due to increase in the grain size with increase in cerium concentration as suggested by our SEM analysis. Figure 7.6 compares

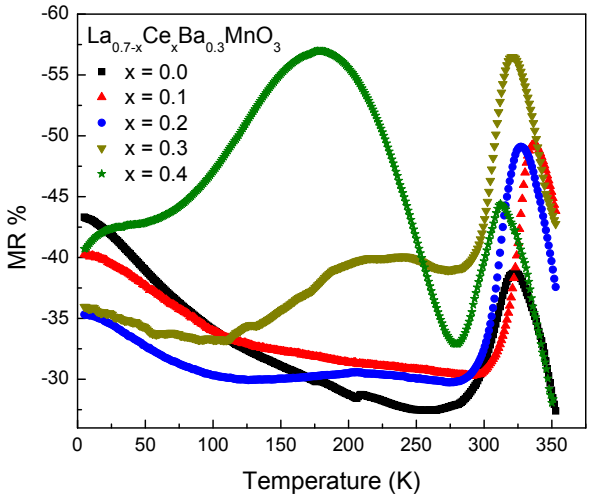

Figure 7.5: Temperature dependence of magnetoresistance, MR = [ρ(7 T) - ρ(0 T)]/ ρ(0 T)), for various x in $La_{0.7-x}Ce_xBa_{0.3}MnO_3$. The MR around 200 K in x = 0.4 arises due to the Ce:4f spin disordered scattering.

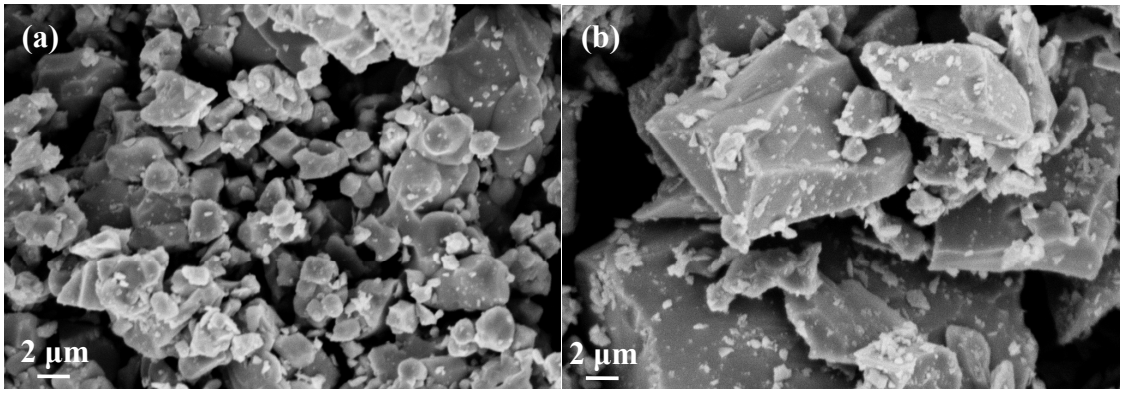

Figure 7.6: Scanning Electron Micrograph of x = 0.0 and 0.3 in $La_{0.7-x}Ce_xBa_{0.3}MnO_3$ clearly showing that the grain size of Ce-containing sample (x = 0.3) is larger than the one without cerium.

the grain size for x = 0 and x = 0.3 samples and it is obvious that the latter has larger grain size. This is also clear from the particle size calculation done using Debye-Scherrer formula on XRD data, given in table 7.2. For x = 0.4, however, the MR increases which is mainly due to Kondo-like scattering of Mn-e_g electrons by the Ce-4f moments as observed in $R_{0.1}Ce_{0.4}Sr_{0.5}MnO_3$ (R = La, Pr) [148, 149].

7.2.4 Conclusions

In conclusion, the system $La_{0.7-x}Ce_xBa_{0.3}MnO_3$ transforms from a rhombohedral structure to orthorhombic at $x = 0.3$. The behavior of magnetization, resistivity and magnetoresistance are similar to that observed for $La_{0.5-x}Ce_xSr_{0.5}MnO_3$ suggesting a Kondo-like behavior. This indicates that Ce-ions are in trivalent state.

7.3 Spin state transition in the ferromagnet $Sr_{0.9}Ce_{0.1}CoO_{2.85}$

7.3.1 Introduction

The perovskite cobalt oxides $R_{1_x}A_xCoO_3$ (R = rare earth: A = alkaline earth) have received much attention owing to various spin state transitions of cobalt ions in Co^{3+} and Co^{4+} oxidation states and associated physical properties such as magnetization, metal-insulator transition and magnetoresistance [154–156]. In these materials, the observed spin state transition arises due to the close proximity of the crystal field energy and the Hund's rule coupling energy. Since the energy difference between these two energy states is only subtle and the crystal field energy dominates over Hund's energy, a small increase in thermal energy can populate the excited state. For example, the ground state of $LaCoO_3$ is a non-magnetic insulator because of the low spin (LS) state of Co^{3+} ($t_{2g}^6 e_g^0$) ions. With increase of temperature, it undergoes a transition to an intermediate spin (IS) state ($t_{2g}^5 e_g^1$) at about 100 K, which results in a steep increase in magnetic susceptibility and a semiconductor-metal transition [157, 158]. On the other hand, the ground state of the compound $SrCoO_3$ with the cobalt ions in high oxidation state (Co^{4+}) is a metallic ferromagnet with the Curie temperature, $T_C \sim 300$ K [159]. The spin state of this system has been suggested to be intermediate with the $t_{2g}^4 e_g^1$ electronic configuration [160, 161]. Synthesis of this compound by the solid state reaction method leads to the formation of Brownmillerite-type structure [162]. It requires high oxygen pressure to stabilize this compound in the perovskite structure with the cobalt ions in the Co^{4+} oxidation state. Depending on the oxygen pressure, this compound can take different oxygen content [163, 164]. The oxygen vacancies

in $SrCoO_{3-\delta}$ result in a Co^{4+} and Co^{3+} mixed valence and thus a decrease in T_C. Alternatively, it has been reported that this compound could be stabilized in perovskite structure under normal preparative conditions by substituting various rare earth ions for Sr^{2+} ions [165–169].

In general, the transition metal oxides with the ABO_3 perovskite structure containing cerium at the A-site are difficult to prepare because of the stability of the Ce^{4+} oxidation state. The size of the Ce^{4+} ion is too small to stabilize the perovskite structure. There are only few three-dimensional perovskite oxides reported in the literature with the cerium at the A-site occupied completely or together with other rare earths/alkaline earths. In these oxides, the cerium is reported to be in Ce^{3+} state or Ce^{4+}/Ce^{3+} mixed valence state [170, 171]. As a result, the extended nature of $4f^1$ electronic configuration of cerium has significant influence on the transport and magnetic properties. For example, anomalous magnetic ordering of cerium and Kondo-like effect has been reported in $R_{0.1}Ce_{0.4}Sr_{0.5}MnO_3$ (R = La and Pr) [148, 149]. It is for these reasons, we have studied the effect of cerium substitution on magnetization, magnetotransport, Infrared (IR) absorption and heat capacity in $Sr_{1-x}Ce_xCoO_{3-\delta}$.

7.3.2 Experimental

The samples, $Sr_{1-x}Ce_xCoO_{3-\delta}$ ($x = 0.1$ and 0.2) were prepared by a citrate method as described below. The starting materials, $SrCO_3$, $Ce(NO_3)_3.6H_2O$ and $Co(NO_3)_3.6H_2O$ were taken in appropriate molar ratio with an excess of citric acid and dissolved in water to form a clear solution. First the solution was heated at 150 ^oC to evaporate water and to form a gel. The gel was heated at 250 ^oC to form a solid. The solid was then heated at 650 ^oC in flowing N_2 to decompose carbon

moiety. The resulting material was ground in an agate mortar and the powder was heated at 1000 ^{o}C (N_2) and followed by 1100 ^{o}C in O_2 atmosphere with intermittent grindings. Finally the powder was pressed into bars and annealed in flowing oxygen at 1150 ^{o}C. The oxygen content was determined by the iodometric titration method [172]. In this method, a known amount (38 mg) of the sample was dissolved in 15 ml of 2 M HCl solution containing an excess of KI resulting in the reduction of tri and tetravalent cobalt ions of the sample to Co^{2+} ions and liberation of a stoichiometric amount of iodine in the solution. Liberated iodine was titrated immediately with the standardized (0.05 M) $Na_2S_2O_3$ solution using starch as an indicator.

Phase purity and structural analysis of the samples were carried out with powder x-ray diffraction (XRD) data collected from a Phillips diffractometer by the Rietveld analysis method using the program Fullprof [44]. Magnetization measurements were performed with a vibrating sample magnetometer in Physical Property Measuring System (PPMS) (Quantum Design, USA). Fourier transform far-infrared (FTFIR) measurements were carried out using Bruker IFS 66 v/S in the transmission mode. The pellets were prepared by diluting a small portion of the sample with polyethylene. The spectra were recorded in the temperature range 113-300 K. Magnetoresistance measurements were made by the standard four-probe method with the PPMS. Heat capacity was measured by the relaxation method between the temperature interval of 2 K and 300 K under zero applied magnetic field with PPMS. In this measurement a small piece of sample was fixed on the sapphire substrate with the help of Apiezon N grease. The sample heat capacity was obtained by subtracting out the addenda contribution from the total heat capacity.

7.3.3 Results and discussion

7.3.3.1 Structural analysis

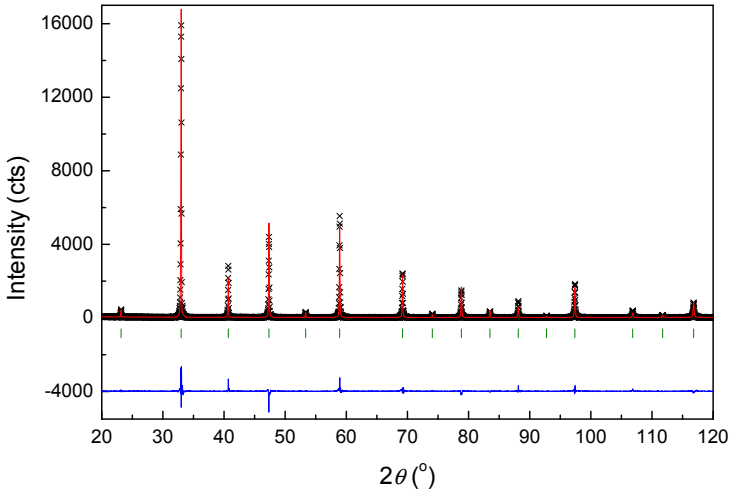

Figure 7.7: Observed, calculated and difference x-ray diffraction pattern of $Sr_{0.9}Ce_{0.1}CoO_{2.85}$ after Rietveld refinement.

Although the samples with $x = 0.1$ and 0.2 in $Sr_{1-x}Ce_xCoO_{3-\delta}$ were prepared, only the sample with $x = 0.1$ resulted in a single phase with the cubic perovskite structure. It may be mentioned here that the sample ($x = 0.1$) prepared by the solid state reaction method contained a small amount of the CeO_2 impurity phase. Since the sample with $x = 0.2$ had a considerable amount of unreacted CeO_2 impurity only the single phase sample ($x = 0.1$) prepared by the chemical route has been characterized and studied. The structural parameters obtained from the Rietveld refinement of XRD data with the space group P$m\bar{3}m$ is shown in table 7.3 and the final pattern is shown in figure 7.7. The obtained lattice parameter ($a = 3.8368(2)$ $\AA$) is close to that reported for $SrCoO_3$ [159]. The oxygen content determined from the iodometric titration method is 2.85 ± 0.01 so that the chemical formula of the sample can be written as $Sr_{0.9}Ce_{0.1}CoO_{2.85}$. According to this formula and

considering that the Ce-ions are in tetravalent state, the cobalt ions in this compound exist in a mixed valence state with 50% of Co^{3+} ions and 50% of Co^{4+} ions. Similar value of oxygen content for the sample prepared in flowing oxygen has been reported for the same system by Maignan et al. [173]. They have reported electron diffraction study of the microstructure on this system with different oxygen content. They observed superstructure that is related to the oxygen vacancy ordering. Since the present sample also has oxygen vacancy a similar microstructure could be present in this sample.

Table 7.3: Structural parameters of $Sr_{0.9}Ce_{0.1}CoO_{2.85}$ obtained from the Rietveld refinement of XRD data. *Value fixed as obtained from the analytical method (see text). B for oxygen is fixed at 1.5.

P*m3m* $a = 3.8368$ Å					
Atoms	x	y	z	B(Å^2)	Occupancy
Sr/Ce	0.0	0.0	0.0	0.91(5)	0.9/0.1
Co	0.5	0.5	0.5	0.79(8)	1.0
O	0.5	0.5	0.0	1.5	2.85*
Bragg R = 8.5 % and $\chi^2 = 4.3$.					

7.3.3.2 Magnetic properties

Temperature dependence of magnetic susceptibility (χ) measured at 0.3 T in field cooled (FC) mode is shown in figure 7.8. It can be seen that the χ increases rapidly below $\sim$ 160 K indicating the ferromagnetic transition (T_C). At low temperatures the χ tends to saturate. Above T_C, the variation of susceptibility with temperature could be fitted with the Curie-Weiss law. The value of paramagnetic effective moment, μ_{eff} obtained from the fit is 3.18 μ_B. This value of μ_{eff} is close to the calculated one (3.39 μ_B) arrived at by considering the IS state for both the

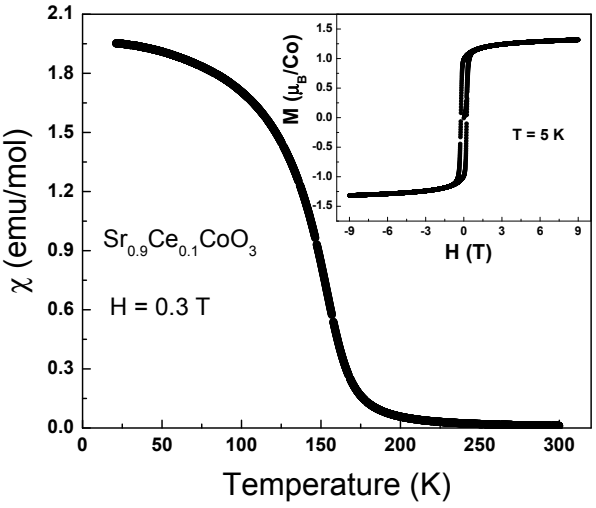

Figure 7.8: Variation of magnetic susceptibility as a function of temperature. Inset shows the isothermal magnetization at 5 K.

Co^{3+} and Co^{4+} ions and the cerium in +4 oxidation state. Such a spin state has been reported for $R_{0.67}Sr_{0.33}CoO_3$ [174]. The value of the paramagnetic Curie-Weiss temperature, θ_P obtained from the intercept is 150 K which is close to the observed T_C. The magnetization (M) as a function of applied field (H) at 5 K is shown in the inset of figure 7.8. The M(H) curve is similar to that of a soft ferromagnet and the value of saturation magnetization (M_s) is 1.15 μ_B/Co. A similar M(H) curve and saturation magnetization (M_s) value have been reported for $Sr_{0.9}Th_{0.1}CoO_{3-\delta}$ [175]. However, the observed value is much lower than the expected value (2.5 μ_B) based on the IS state of Co^{3+} and Co^{4+} ions. This may indicate that there is a spin state transition at low temperatures.

7.3.3.3 Far-infrared studies

In order to verify the spin state transition, we have carried out temperature dependent IR absorption experiments on the cubic perovskite, $Sr_{0.9}Ce_{0.1}CoO_{2.85}$ with

O_h^1 symmetry. For the cubic perovskite, ABO_3, the irreducible representation is given by $\Gamma_{total} = 4F_{1u}+F_{2u}$ [176]. One of the F_{1u} mode corresponds to the acoustic phonon and F_{2u} is silent. Hence a cubic perovskite has three IR active modes, namely, the stretching mode of the BO_3, bending mode of the BO_3 and the translational motion of A atoms with respect to the BO_3 (external mode). In general, when a spin state change occurs in the BO_6 octahedra, the bond distances and the bond angles are affected. Hence one would observe changes in the phonon frequencies across the transition as observed in $LaCoO_3$ [177].

Figure 7.9(a) shows the typical room-temperature IR spectrum for $Sr_{0.9}Ce_{0.1}CoO_{2.85}$. We can observe all the three IR active modes in the spectrum, namely, 117.3 cm^{-1}-external mode, 157.5 cm^{-1}-bending mode and 195.7 cm^{-1}-stretching mode. Figure 7.9(b-d) shows the temperature dependence of these modes. It is interesting to note that the external mode at 117.3 cm^{-1} is insensitive to the temperature variation. This is consistent with what is expected for a spin state transition which does not affect the A-site ions. On the other hand, the internal modes of BO_3 change near the ferromagnetic transition temperature (160 K). Upon decreasing the temperature one expects the optical modes to harden or remain unchanged. Softening or change in slope of the mode signifies a possible phase transition. It is important to note that the stretching mode (195.7 cm^{-1}) which is related to modulation of B-O bond distance shows a significant decrease (1%) with decrease in temperature below 160 K. On the other hand the bending mode (157.5 cm^{-1}) which is related to the bending of the O-B-O angle shows a hardening up to 160 K (0.3 %) and subsequently shows very little change with decrease in temperature. We suggest that the softening of these internal modes near T_C result from a spin state transition. At high temperatures, both Co^{3+} and Co^{4+} ions are in the IS state and have one electron in e_g orbital. Since this material undergoes metal-metal transition, only

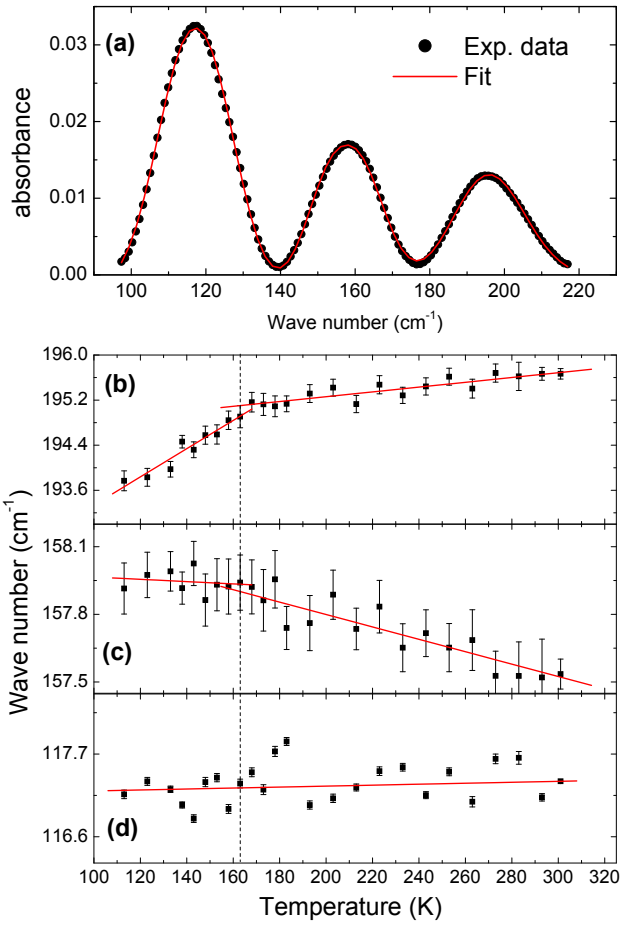

Figure 7.9: (a) Room-temperature FIR spectrum of $Sr_{0.9}Ce_{0.1}CoO_{2.85}$ (b-d). Temperature dependence of vibrational modes at (b) 117.3, (c) 157.5 and (d) 195.7 cm^{-1}. The change in slope observed near 160 K in the modes (b) and (c) suggests that there is a spin state transition.

one of them should undergo a transition to a LS state where there is no e_g electron. This will lead to net increase in Co-O bond length and thus a decrease in phonon energy (softening). Now the question is which one undergoes spin state transition. If we consider that the IS Co^{3+} ions are transformed to LS $Co^{3+}(t_{2g}^6 e_g^0)$ as observed in $LaCoO_3$ [177], the resulting ground state configuration is IS $Co^{4+}(t_{2g}^4 e_g^1)$ which is similar to that suggested for the ferromagnetic half-metallic $SrCoO_3$ where there is

a large e_g band width [161]. On the other hand, the configuration IS Co^{3+} and LS Co^{4+} can give way to double exchange mechanism. From the present study, however, it is difficult to ascertain whether the double exchange mechanism involving hopping of e_g electron with ligand hole configuration ($t_{2g}^6\underline{L}$) or band magnetism is responsible for ferromagnetism. In both the ground state configurations, there is a population of e_g orbital and the calculated saturation moment is 1.5 μ_B/Co, which is higher than the observed moment. The fact that this system shows metallic behavior and the absence of strong feature in the resistivity at the Curie temperature suggest that the ground state of this system is LS $Co^{3+}(t_{2g}^6e_g^0)$ and IS $Co^{4+}(t_{2g}^4e_g^1)$.

Alternatively, electron-phonon coupling could also be associated with the observed phonon behavior. If the changes in internal modes were due to electron-phonon coupling, one would expect not only an abrupt increase in phonon frequencies but also a decrease in full width at half maximum across the ferromagnetic transition, as for example, observed in $SrRuO_3$ and $La_{0.7}Ca_{0.3}MnO_3$ [178, 179].

7.3.3.4 Resistivity

The temperature dependence of resistivity ρ(T) measured under zero and 7 T field is shown in figure 7.10. In zero field, ρ(T) decreases linearly with decrease of temperature and deviates at around 220 K with a significant drop in ρ at 160 K indicating a broad metal-metal transition which is correlated with the ferromagnetic transition observed in magnetic susceptibility. At low temperature (T $\sim$ 60 K), there is a well defined minimum in the resistivity (ρ_{min}). Such a ρ_{min} has been observed not only in other perovskite cobalt oxides but also in bulk and thin film forms of manganates and $SrRuO_3$. The origin of ρ_{min} in these materials has been attributed to electron-electron scattering rather than the Kondo effect, grain boundary and phase separation [180–182]. Since the present sample is polycrys-

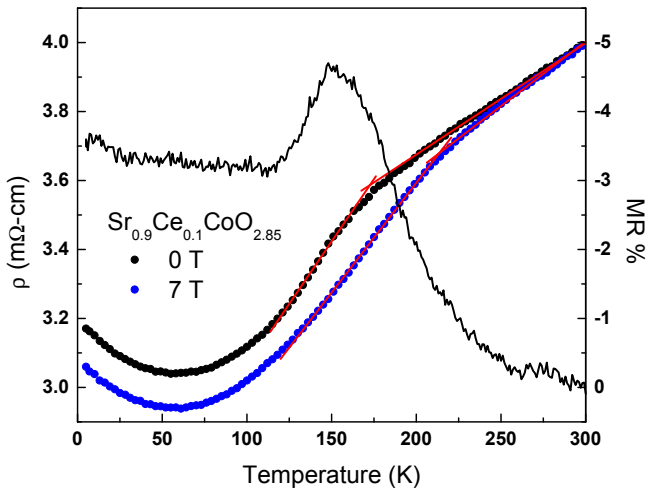

Figure 7.10: Temperature dependence of resistivity under 0 T and 7 T field showing a metal-metal transition ($\sim$ 160 K) and resistivity minimum ($T_{min} \sim 60$ K). Temperature variation of MR also shown in this figure.

talline, it is difficult to separate various contributions. However, it can be seen from figure 7.10 that the T_{min} does not change significantly with an applied field of 7 T. If the origin were solely from grain boundaries, we would expect that T_{min} should be suppressed. Therefore, the insensitivity of T_{min} to the applied filed indicates that there can be other mechanisms as discussed above which contribute to the increase in resistivity at low temperatures in addition to the grain boundary scattering.

Under 7 T, there is a positive shift of the inflection point of two linear regions indicating the presence of possible inhomogeneity or short-range correlations. It is important to note that there is a negative magnetoresistance (MR) from 250 K down to the lowest temperature measured. The MR near T_C is due to reduced spin disordered scattering. As the T_C of $SrCoO_{3-\delta}$ can be as high as 300 K depending upon the oxygen content, the observed MR at much above T_C in the present system may be due to the broad ferromagnetic transition resulting from the inhomogeneity

arising from the oxygen vacancies. However, the magnitude of magnetoresistance is smaller than that observed in manganates as shown in the figure 7.10. Similar results were reported for $Sr_{0.9}R_{0.1}CoO_{3-\delta}$ (R = La and Th) [169, 175].

7.3.3.5 Heat capacity

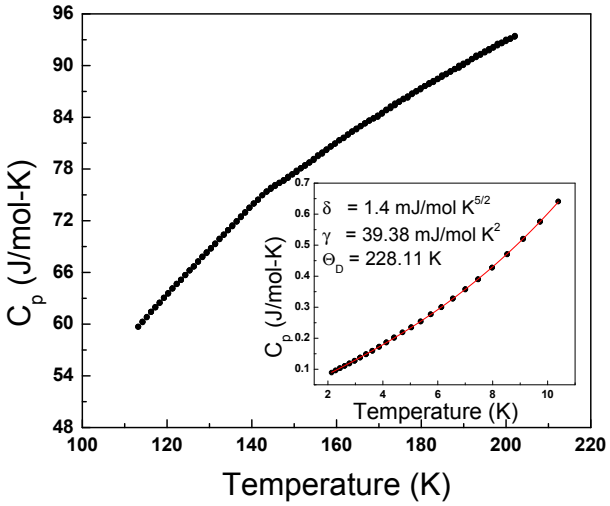

Figure 7.11: Plot of heat capacity versus temperature between 110 K and 200 K. Inset shows the variation of C_P/T versus T2 in the temperature range, 2.2 K - 10 K.

The temperature dependence of specific heat data in the temperature interval 100-200 K is shown in figure 7.11. As seen from this figure, there is a small change in slope near 150 K but there is no clear anomaly associated with the ferromagnetic transition. The absence of specific heat anomaly may be due to the broad ferromagnetic transition as indicated by ρ(T). It is also possible that the entropy change associated with the cobalt ordering is very small. In fact, a very low value (10%) of the expected entropy has been reported for $La_{0.67}Sr_{0.33}CoO_3$ and in manganates [174, 183]. The low temperature specific heat data (2.2-10 K) is shown in the inset of figure 7.11 as C vs T plot. The data are fitted with the formula C

$= \delta T^{3/2} + \gamma T + \beta T^3$ representing contributions from ferromagnetic spin waves, electrons and lattice, where δ, γ and β are the magnetic, electronic and lattice specific heat coefficients; $\beta \propto 1/\Theta_D^3$ and Θ_D is the Debye temperature. The values of δ, γ and Θ_D obtained from the fit are 1.4 mJ/mol $K^{5/2}$, 39.4 mJ/mol K^2 and 228 K, respectively. The observed value of is less than that (47.8 mJ/mol K^2) reported for $La_{0.67}Sr_{0.33}CoO_3$ but nearly 14 times larger than that in $La_{0.7}Sr_{0.3}MnO_3$ [174, 183]. Since such a high value of has been reported for the non-metallic $NdCu_2O_4$ the contribution to the linear term has been discussed in terms of magnetic origin [184].

7.3.4 Conclusions

In conclusion, we have reported that the system $Sr_{0.9}Ce_{0.1}CoO_{2.85}$ crystallizes in a cubic perovskite structure. It exhibits a ferromagnetic as well as a broad metal-metal transition around 160 K with a resistivity minimum at $T_{min} = 60$ K. It shows a negative magnetoresistance below $T \sim 250$ K with a maximum magnitude of 5% near T_C at 7 T. Magnetic measurements reveal that the Co^{3+} and Co^{4+} ions are in the intermediate spin states ($t_{2g}^5 e_g^1$) and ($t_{2g}^4 e_g^1$), respectively. Below T_C, the Co^{3+} (IS) ions are transformed to the LS state. The electronic specific heat coefficient γ = 39.4 mJ/mol K^2 is much higher than that observed in related materials.

7.4 Itinerant ferromagnetism to insulating spin glass in $SrRu_{1-x}Cu_xO_3$ ($0 \leq x \leq 0.3$)

7.4.1 Introduction

Ruthenium oxides with perovskite and related structures have been the subject of intensive research owing to their interesting properties of magnetism and superconductivity [185–187]. It is well known that $SrRuO_3$ is a metallic ferromagnet with a Curie temperature of $T_C \sim 165$ K [185]. In this material, ferromagnetism has been attributed to the collective-electron magnetism that arises from low spin Ru^{4+} ions having localized 4-d electrons with magnetic moments ranging from 0.8 - 1.6 μ_B/Ru. The unsaturated magnetization of $SrRuO_3$ even at 4.2 K and 12.5 T suggests a very narrow 4-d band compare to a 3d band of iron and/or large magnetocrystalline anisotropy. In this material, the Ru ions are coordinated with six oxygen ions forming RuO_6 octahedral layers which are connected through apical oxygen. From the literature, it is known that the magnetic coupling is very sensitive to the perturbation in Ru-O-Ru bond length and angle by chemical substitution [188]. Therefore, the study of chemical substitution either at A or B site of this ABO_3 perovskite will give an insight into the physical properties of these systems. Substitution of various transition metals such as Zn, Ni, Co, Fe, Mn and Cr at the Ru site has already been reported [189–191]. Except for Cr, the substitution of other metals suppresses T_C. For M = Cr, the T_C increases with Cr substitution up to a critical concentration and then decreases with further increase of Cr [192]. We have chosen the study of copper substitution on the magnetic and transport properties of $SrRuO_3$. This study is also interesting in view of the superconductivity reported in a double perovskite $Sr_2YRu_{1-x}Cu_xO_6$ [193]. Although

the structures of $SrRuO_3$ and $SrCuO_2$ are different, we thought that there could be a considerable amount of Cu substitution at the Ru site while preserving the perovskite structure. In this paper, we report that the substitution of Cu at the Ru site in $SrRuO_3$ decreases the T_C significantly and the system becomes insulating spin glass for $x = 0.3$. For $x = 0.2$, both clusters of ferromagnetic and antiferromagnetic regions coexist due to possible magnetic phase separation. Our results are quite different from those reported in the literature [194]. The discrepancies between these reports are discussed based on the preparation method which influences the properties greatly [195]. Further, these systematic substitutional studies may explain the observation of highest T_c for $Ru_{0.7}Cu_{0.3}Sr_2GdCu_2O_8$ [196] as the ferromagnetism get suppressed for 30% of Cu in $SrRuO_3$.

7.4.2 Experimental

Samples were prepared by a conventional solid state method from the starting materials, $SrCO_3$, CuO and RuO_2 (preheated at 600 ^{o}C) with 99.9 % purity. Stoichiometric amounts of starting materials were weighed and mixed thoroughly with the use of an agate mortar. The mixed powder was calcined at 900 ^{o}C and 1100 ^{o}C for 12 hours at each temperature with an intermittent grinding. All these samples were sintered at 1200 ^{o}C in flowing oxygen for 12 hours except $SrRuO_3$ for which the sintering temperature was 1100 ^{o}C. Phase purity and structural analysis of the samples were carried out with x-ray powder diffraction (XRD) data collected from the Seifret 3000 TT and Philips X'Pert Pro x-ray diffractometers by the Rietveld analysis method using the program fullprof [44]. Magnetic measurements were performed with a Vibrating Sample Magnetometer (VSM) in Physical Property Measuring System (PPMS), Quantum Design, USA. Standard four-probe resistiv-

ity, with and with out magnetic field (7 T), and ac susceptibility measurement of the samples were performed in PPMS.

7.4.3 Results and discussion

7.4.3.1 Structural analysis

There exists a solubility limit ($x = 0.3$) of copper in $SrRu_{1-x}Cu_xO_3$ beyond which impurity peaks belonging to CuO phase appear. For $x = 0$, the structure is consistent with an orthorhombic system (space group Pnma) as already reported [197]. The structure remains orthorhombic up to $x = 0.1$. For $x = 0.2$ and 0.3, it transforms to a tetragonal phase with the space group I$4/mcm$. This space group is in accordance with a report that the $SrRuO_3$ transforms to high temperature cubic phase (P$m3m$) through an intermediate temperature tetragonal structure (I$4/mcm$) [198].

The observed, calculated and difference XRD patterns, for $x = 0.1$ and 0.2, obtained from the final Rietveld refinement of the data collected from the Philips diffractometer with a secondary graphite monochromater are shown in figure 7.12. From the insets of this figure, it is clear that there is a structural change. In the case of $x = 0.2$, as discussed in the following paragraph, the magnetic measurements indicate the presence of small amount of $SrRuO_3$ phase. But we could not see any clear peak in the XRD pattern due to this impurity phase. This suggests that the amount of secondary phase must be less than 5 %. However, the $SrRuO_3$ phase was also included as a secondary phase in the refinement. The inclusion of the secondary phase resulted in decrease of Bragg R-factor from 3.7 to 2.99 (%) and the amount of secondary phase was determined to be 3 (%). The structural parameters obtained from the refinement are shown in table 7.4. The volume of

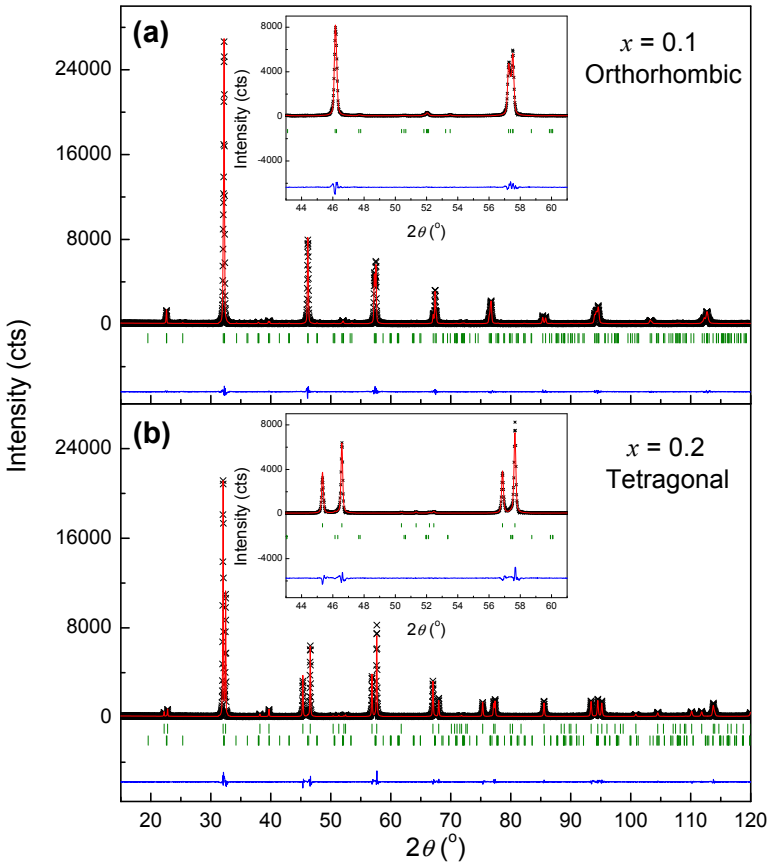

Figure 7.12: Observed, calculated and difference XRD patterns of $x = 0.1$ (orthorhombic) and 0.2 (tetragonal). Vertical tick marks are the symmetry allowed reflections. For $x = 0.2$, the vertical tick marks in second row corresponds to $SrRuO_3$ phase. Insets show splitting of lines due to structural change.

the unit cell increases with increase of copper content (242.28(1) Å^3 for $x = 0$ to 242.83(2) Å^3 for $x = 0.3$) indicating that the copper ions are in +2 oxidation state according to the ionic size consideration. The ionic radii of Ru^{4+} and Cu^{2+} in six coordination are 0.62 Å and 0.73 Å, respectively [121]. A similar behavior has been reported for $CaRu_{1-x}Cu_xO_3$ [199]. If Cu ions were in Cu^{3+} state ($r_{Cu^{3+}} = 0.54$ Å), we would expect a decrease in volume with increasing Cu content. As the Cu^{2+}

Table 7.4: Structural parameters of $SrRu_{1-x}Cu_xO_3$ ($x = 0.1$ and 0.2).

Parameter	$x = 0.1$	$x = 0.2$
Space group	Pnma	I4/mcm
a (Å)	5.5403(1)	5.5109(1)
b (Å)	7.8477(2)	-
c (Å)	5.5774(1)	7.9947(1)
V (Å^3)	242.499(9)	242.800(7)
Sr: x, y, z	0.0137(3), ¼, -0.00112(6)	0, ½, ¼
B (Å^2)	0.66(3)	0.57(5)
Ru, Cu: x, y, z	0, 0, ½	0, 0, 0
B (Å^2)	0.33(3)	0.10(5)
O(1): x, y, z	-0.001(2), ¼, 0.452(3)	0, 0, ½
O(2): x, y, z	0.224(2), -0.024(1), 0.223(2)	0.2136(9), 0.7136(9), 0
χ^2	2.96	3.78
Bragg R (%)	2.55	2.99
(Ru,Cu)-O(1) Å	1.981(2) × 2	1.999 × 2
(Ru,Cu)-O(2) Å	1.993(9) × 2	1.969(5)× 4
(Ru,Cu)-O(2) Å	1.980(9) × 2	-
(Ru,Cu)-O(1)-(Ru,Cu) (^{o})	164.13(6)	180.0
(Ru,Cu)-O(2)-(Ru,Cu)(^{o})	163.284)	163.4(2)

(d^9) electronic configuration is Jahn-Teller active, the difference in bond length between the (Ru,Cu) - O(1) and (Ru,Cu) - O(2) bonds is a measure of Jahn-Teller distortion. It can be seen from table 7.4 that for $x = 0.2$, there are two longer and four shorter (Ru,Cu) - O bonds indicating that the $(Ru,Cu)O_6$ octahedra are distorted by an elongation of two axial bonds. Further, the difference between the two longer and four shorter bonds is 0.03 Å which indicates a significant Jahn-

Teller distortion. This confirms that the copper ions are substituted as Cu^{2+} ions. Although Ru and Cu ions are distributed at the same site, such a strong Jahn-Teller distortion can only be due to Cu^{2+} ions as the Ru ions do not show Jahn-Teller distortion. For $x = 0.1$, the difference between the various bond lengths is only about 0.01 Å. The lattice parameters for $x = 0.3$ are $a = 5.5129(1)$ Å and $c = 7.9938(3)$ Å.

7.4.3.2 Magnetic properties

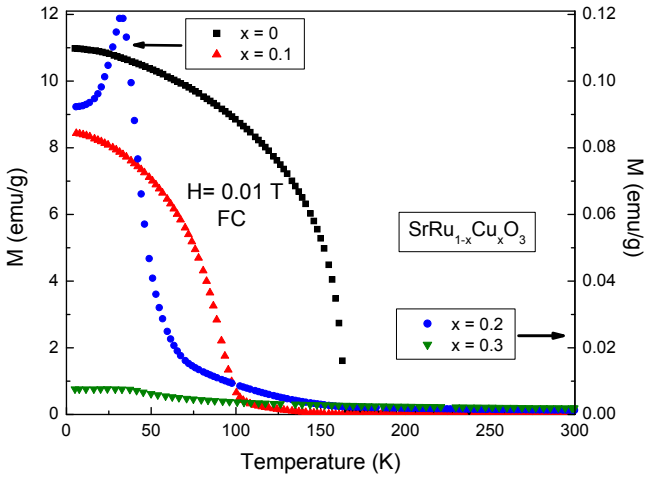

Figure 7.13: Temperature dependence of magnetization recorded at 0.01 T (FC) in $SrRu_{1-x}Cu_xO_3$. Inset shows the antiferromagnetic transition at around 32 K in $x = 0.2$.

The field cooled (FC) temperature dependent magnetization, M(T) data of $SrRu_{1-x}Cu_xO_3$ ($x = 0.0$ to 0.3) in the temperature interval of 5 K to 300 K at a field (H) of 0.01 T are shown in figure 7.13. It can be seen from this figure that for $x = 0$, there is a sharp ferromagnetic transition at 163 K which is close to the reported value [185]. With increase of x, the ferromagnetic transition decreases to 100 K and 65 K for $x = 0.1$ and 0.2, respectively. The decrease of T_C

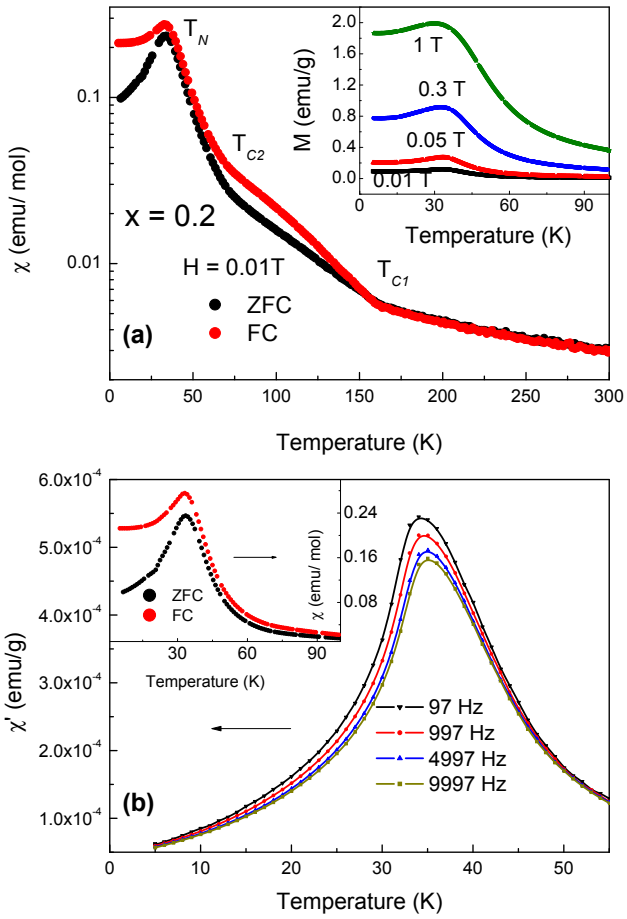

Figure 7.14: (a) ZFC and FC susceptibility measured for $x = 0.2$ at 0.01 T. (b) Frequency dependence of the real part of ac susceptibility ($\chi\prime$).

is due to the dilution of Ru^{4+} ions by the Cu^{2+} ions and hence the narrowing of Ru $4d$ bandwidth. For $x = 0.1$, in addition to the transition at 100 K, there is another weak ferromagnetic transition at the temperature close to the ferromagnetic transition observed in $SrRuO_3$. This indicates the presence of traces (< 3 %) of $SrRuO_3$ impurity phase. For $x = 0.2$, the zero field cooled (ZFC) and FC susceptibility are shown in figure 7.14a. It can be seen from the magnetization curves that there are features at 155 K, 65 K and 32 K. The feature at 155 K (T_{C1}) indicates ferromagnetic ordering due to the $SrRuO_3$ impurity phase as also

observed in $x = 0.1$ whereas, the feature at 65 K (T_{C2}) is due to ferromagnetic transition of copper substituted phase ($x = 0.2$). On the other hand, the peak at 32 K (T_N) is antiferromagnetic that arises from the magnetic interaction between Ru and Cu ions. The presence of both ferromagnetic and antiferromagnetic interactions indicates a possible magnetic phase separation. Magnetic phase separation in perovskite manganates has been investigated extensively [200, 201]. In order to confirm the antiferromagnetic ordering, we have performed magnetization at various fields. The fact that the peak at M(T) is robust and does not disappear even at a field of 1 T as shown in the inset of figure 7.14a confirms the presence of antiferromagnetic interactions. Obviously, there cannot be a long range antiferromagnetic ordering and it is only a short range in nature. Although the ZFC and FC dc susceptibility show irreversibility, as shown in expanded linear scale in the inset of figure 7.14b, the fact that the decrease of FC magnetization below the peak indicates that this transition is not that of a typical spin glass. In the spin glass system, the FC magnetization remains constant below the peak as seen for $x = 0.3$ (Fig. 7.15). Also the peak position at the ac susceptibility does not shift appreciably with frequency. The value of $(\Delta T_g/T_g)$ $(1/\ \Delta \log_1 0\ \nu)$ for 100 Hz and 1 kHz is 0.0003 (Δ, change of T_g and $\log_1 0\ \nu$; T_g, spin-glass transition temperature; and ν, frequency), assuming that T_g is the peak temperature of χ'. Such a low value rules out the possibility of a spin glass. Therefore, it appears that substitution of Cu^{2+} ions suppresses ferromagnetism and induces antiferromagnetic interaction between Cu and Ru moments.

For $x = 0.3$, there is only one transition at 40 K below which the magnetization remains constant and there is no indication for the presence of $SrRuO_3$ impurity phase. However, this feature cannot be due to ferromagnetic transition as it is always associated with a sharp rise in magnetization. In fact, the magnetic sus-

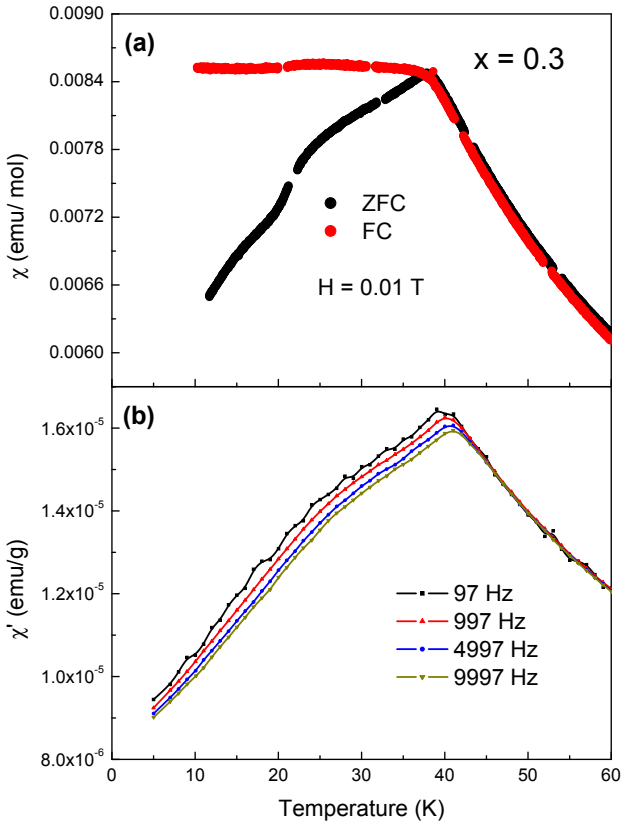

Figure 7.15: (a) ZFC and FC susceptibility measured at 0.01 T for $x = 0.3$. (b) Frequency dependence of the real part of ac susceptibility ($\chi\prime$) indicating a spin glass behavior.

Table 7.5: Variation of Θ_P, Observed and calculated μ_{eff} and M_S with x in $SrRu_{1-x}Cu_xO_3$.

x	Θ_P (K)	Exp.$\mu_{eff}(\mu_B)$	Calc.$\mu_{eff}(\mu_B)$	$M_s(\mu_B)$
0.0	163.88	2.815	2.828	1.46
0.1	102.25	2.642	2.741	0.97
0.2	-6.64	2.693	2.651	0.28
0.3	-144.41	2.575	2.550	0.074

ceptibility follows the Curie-Weiss behavior down to 50 K. All other samples show Curie-Weiss behavior above 175 K. The values of effective paramagnetic moment (μ_{eff}) for all the samples as obtained from the Curie-Weiss fit are given in table 7.5. For $x = 0$, the experimental value of $\mu_{eff} = 2.815\ \mu_B$ implies that the Ru is in +4 oxidation state with 2 unpaired electrons due to low spin arrangement (S = 1) whose calculated μ_{eff} is 2.828 μ_B. For x $\geq$ 0.1, the experimental values are close to the theoretical value calculated by considering Cu in +2 oxidation state (S = 1/2) which is in agreement with the variation of lattice volume as discussed above. For $x = 0.1$ and 0.2, the calculated moment includes the contribution from $SrRuO_3$ impurity phase. As the Ru^{4+} ions are substituted by the lower valent Cu^{2+} ions the charge compensation requires a corresponding oxygen vacancy or higher oxidation states, Ru^{5+}/Ru^{6+} of Ru-ions. Consideration of Ru^{5+} state (S = 3/2) would result in larger effective magnetic moment than the observed one. Therefore, the possibility of the existence of Ru^{5+} ions appears to be ruled out. On the other hand, the effective moment for Ru^{4+} or Ru^{6+} ions would be the same because both of them have S = 1/2. This makes it difficult to understand the change in oxidation state of Ru^{4+} ions from the present study. Finally, there can be a vacancy of oxygen that can compensate the charge imbalance due to Cu^{2+} substitution. A precise knowledge on oxygen content and spectroscopic studies are necessary to know the change in oxidation state of Ru^{4+} ions in copper substituted samples. However, the present study reveals unambiguously that the copper ions are present in the +2 oxidation state. It should be noticed from this table that the paramagnetic intercept, Θ_p changes its sign from positive to negative as x increases. This behavior is consistent with the suppression of ferromagnetism and appearance of antiferromagnetic ordering as discussed above. However, for $x = 0.3$, there is no signature of antiferromagnetic or ferromagnetic ordering in M(T) curve. In order

to understand the nature of magnetic transition in $x = 0.3$, we have measured the zero field cooled (ZFC) and FC susceptibility under 0.01 T and the result is shown in figure 7.15a. As can be seen from this figure that the ZFC curve shows a cusp with a peak at T = 38 K below which there is an irreversibility between the ZFC and FC curves. This behavior is typical of a spin glass system. Such a spin glass behavior could be explained by the disorder of Ru^{4+} and Cu^{2+} ions as well as their competing ferro- and antiferromagnetic interactions, respectively.

In order to get more insight into the spin glass behavior of $x = 0.3$, we have carried out ac susceptibility measurement at various frequencies. The real part of ac susceptibility (χ') as a function of temperature at various frequencies (97, 997, 4997, and 9997 Hz) are shown in figure 7.15b. The measurements were performed at an ac field of 5 Oe. The susceptibility curves display a cusp with a peak around 39 K as observed in ZFC dc susceptibility measurement. It is clear from this figure that there is a frequency dependence of χ' below 44 K down to low temperatures. With the increase of frequency, the peak temperature of the cusp shifts toward the high temperature. The temperature shift, K calculated from the relation, $(\Delta T_g/T_g)$ $(1/\ \Delta \log_1 0\ \nu)$ lies in the range 0.01 - 0.03. Similar value is reported for $RuSr_2Gd_{1.5}Ce_{0.5}Cu_2O_{10-\delta}$ and other spin glasses [202, 203].

The isothermal magnetization M(H) for all the samples recorded at 5 K is shown in figure 7.16. The ordered magnetic moment of x = 0.0 at 9 T field is 1.4 μ_B/Ru which is less than the expected value, 2 μ_B for a localized low spin configuration (S = 1) of Ru^{4+} ion. The low value of ordered moment has been ascribed to band magnetism [204]. With increase of x, the ordered moment decreases due to weakening of ferromagnetism. It is quite obvious from the figure that the sample with $x = 0.3$ shows a linear behavior indicating the absence of ferromagnetism. The absence of ferromagnetism may explain the observation of highest T_c

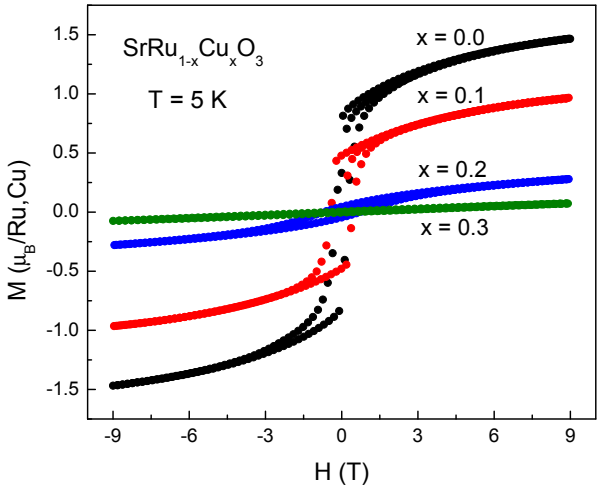

Figure 7.16: Isothermal magnetization measured at 5 K for various x values in $SrRu_{1-x}Cu_xO_3$. For $x = 0.3$, the magnetization varies linearly with field indicating the absence of ferromagnetism.

in $Ru_{0.7}Cu_{0.3}Sr_2GdCu_2O_8$ [196]. Recently, a similar study of copper substitution at the ruthenium site in $SrRuO_3$ has been reported [194]. However, our results on the structure and magnetic properties are slightly different from those reported. This may be due to different preparation conditions followed that are known to affect the structural, magnetic and transport properties. For example, preheating of RuO_2 is essential because it contains moisture. Further, the high reaction temperatures and prolonged heating could lead to Ru vacancies which can affect the structural and physical properties [195].

7.4.3.3 Resistivity

$SrRuO_3$ is well known for its metallic behavior and ferromagnetism. At the magnetic transition (T_C = 165 K) there is a drop in resistivity due to reduced spin disordered scattering as shown in the inset of figure 7.17. With the substitution of Cu at Ru-site, the system loses its metallic behavior and exhibits zero magne-

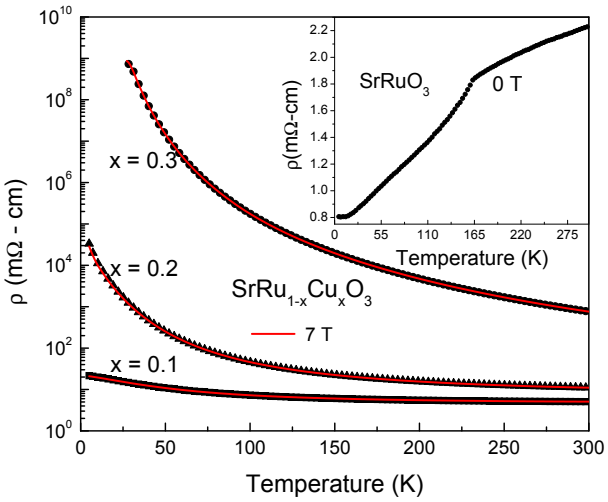

Figure 7.17: Resistivity as a function of temperature in $SrRu_{1-x}Cu_xO_3$. Inset shows the typical ρ(T) behavior of SrRuO3. Other samples show semiconducting behavior without any magnetoresistance. The data represented by various symbols are measured under zero applied field whereas the continuous lines are measured under 7 T field.

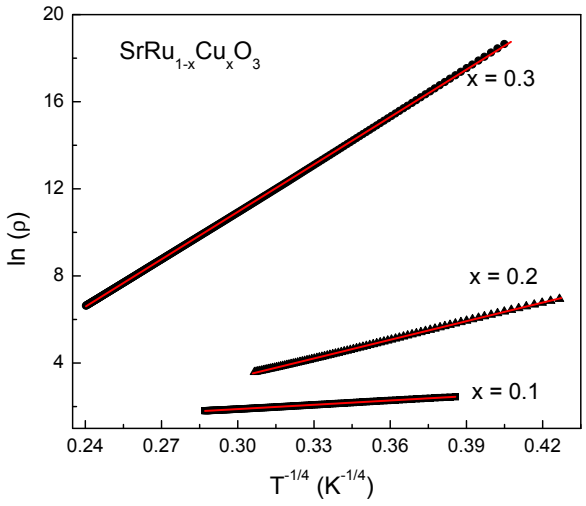

Figure 7.18: Log of resistivity as a function of $T^{-1/4}$ for $x = 0.1$, 0.2 and 0.3 in $SrRu_{1-x}Cu_xO_3$. The linear behavior is indicative of Mott variable range hopping conduction mechanism.

toresistance over the entire range of temperature measured. Figure 7.18 shows the plot of lnρ versus $T^{-1/4}$ for $x \geq 0.1$. For $x = 0.1$, and 0.2, the linear region exists only at low temperatures. For $x = 0.3$, the resistivity shows a linear behavior over the entire range of temperature. This behavior is typical of Mott variable-range hopping (VRH) conduction mechanism described by the expression, $\rho = \rho_0$ exp $(T_0/T)^{1/4}$ where ρ_0 is a resistivity prefactor and T_0 is the characteristic temperature [205–207]. The predicted hopping length is, $r = a(T_0/T)^{1/4}$, where a is the effective Bohr radius [207]. At 10 K, the values of r obtained from the calculation are $4a$, $16a$ and $41a$ for $x = 0.1$, 0.2 and 0.3, respectively.

7.4.4 Conclusions

Substitution of Cu at the Ru site of ferromagnetic metallic $SrRuO_3$ ($T_C = 165$ K) results in a structural transition from an orthorhombic ($x = 0$) to a tetragonal symmetry at $x = 0.2$. The tetragonal structure is consistent with the observed strong Jahn-Teller distortion of (Ru,Cu)O_6 octahedra. Further, the ferromagnetism and metallicity is suppressed and for $x = 0.3$ it becomes an insulating spin glass. At $x = 0.2$, the ferromagnetic ($T_C = 65$ K) and antiferromagnetic regions coexist. The suppression of ferromagnetism with increasing Cu content is caused by the narrowing of Ru-4d bandwidth while the appearance of antiferromagnetism is believed to be due to the exchange interaction between Cu and Ru moments. In the case of $x = 0.3$, a spin glass insulating behavior is observed.

References

[1] Wadhawan, V. K. *Introduction to Ferroic Materials.* (2000).

[2] Morrish, A. H. *The Physical Principles of Magnetism.* Wiley, New York, (1965).

[3] Goodenough, J. B. Theory of the Role of Covalence in the Perovskite-Type Manganites $[La, M(II)]MnO3$, *Phys. Rev.* **100**(2), 564–573 (1955).

[4] Kanamori, J. Superexchange interaction and symmetry properties of electron orbitals, *J. Phys. Chem. Solids* **10**(2-3), 87–98 (1959).

[5] Anderson, P. W. New Approach to the Theory of Superexchange Interactions, *Phys. Rev.* **115**(1), 2 (1959).

[6] Anderson, P. W. Theory of Magnetic Exchange Interactions. in *Magnetism: A Treatise on Modern Theory and Materials,* (Rado, G. and Suhl, H., eds), 25–83. Academic Press, New York (1963).

[7] Goodenough, J. B. *Magnetism and the Chemical Bond.* Interscience Publisher, New York, (1963).

[8] Jona, F. and Shirane, G. *Ferroelectric Crystals.* Pergamon Press, New York, (1962).

[9] Cohen, R. E. Origin of ferroelectricity in perovskite oxides, *Nature* **358**(6382), 136–138 (1992).

[10] Schmid, H. Multi-ferroic magnetoelectrics, *Ferroelectrics* **162**, 317–338 (1994).

[11] Ascher, E., Rieder, H., Schmid, H. and Stössel, H. Some Properties of Ferromagnetoelectric Nickel-Iodine Boracite, $Ni_3B_7O_{13}I$, *J. Appl. Phys.* **37**(3), 1404–1405 (1966).

[12] Wang, J., Neaton, J. B., Zheng, H., Nagarajan, V., Ogale, S. B., Liu, B., Viehland, D., Vaithyanathan, V., Schlom, D. G., Waghmare, U. V., Spaldin, N. A., Rabe, K. M., Wuttig, M. and Ramesh, R. Epitaxial $BiFeO_3$ multiferroic thin film heterostructures, *Science* **299**(5613), 1719–1722 (2003).

[13] Kimura, T., Goto, T., Shintani, H., Ishizaka, K., Arima, T. and Tokura, Y. Magnetic control of ferroelectric polarization, *Nature* **426**(6962), 55–58 (2003).

[14] Hur, N., Park, S., Sharma, P. A., Ahn, J. S., Guha, S. and Cheong, S. W. Electric polarization reversal and memory in a multiferroic material induced by magnetic fields, *Nature* **429**(6990), 392–395 (2004).

[15] Hill, N. A. Why are there so few magnetic ferroelectrics?, *J. Phys. Chem. B* **104**(29), 6694–6709 (2000).

[16] Neaton, J. B., Ederer, C., Waghmare, U. V., Spaldin, N. A. and Rabe, K. M. First-principles study of spontaneous polarization in multiferroic $BiFeO_3$, *Phys. Rev. B* **71**(1), 014113 (2005).

[17] Seshadri, R. and Hill, N. A. Visualizing the role of Bi 6s "lone pairs" in the off-center distortion in ferromagnetic $BiMnO_3$, *Chem. Mater.* **13**(9), 2892–2899 (2001).

[18] Efremov, D. V., Van Den Brink, J. and Khomskii, D. I. Bond- Versus site-centred ordering and possible ferroelectricity in manganites, *Nat. Mater.* **3**(12), 853–856 (2004).

[19] Rao, C. N. R. and Raveau, B. *Colossal Magnetoresistance, Charge Ordering and Related Properties of Manganese Oxides.* (1998).

[20] Cheong, S. W. and Mostovoy, M. Multiferroics: A magnetic twist for ferroelectricity, *Nat. Mater.* **6**(1), 13–20 (2007).

[21] Ikeda, N., Ohsumi, H., Ohwada, K., Ishii, K., Inami, T., Kakurai, K., Murakami, Y., Yoshii, K., Mori, S., Horibe, Y. and Kito, H. Ferroelectricity from iron valence ordering in the charge-frustrated system $LuFe_2O_4$, *Nature* **436**(7054), 1136–1138 (2005).

[22] Lottermoser, T., Lonkai, T., Amann, U., Hohlwein, D., Ihringer, J. and Fiebig, M. Magnetic phase control by an electric field, *Nature* **430**(6999), 541–544 (2004).

[23] Van Aken, B. B. and Palstra, T. T. M. Influence of magnetic on ferroelectric ordering in $LuMnO_3$, *Phys. Rev. B* **69**(13), 134113 (2004).

[24] Fiebig, M., Lottermoser, T., Fröhlich, D., Goltsev, A. V. and Pisarev, R. V. Observation of coupled magnetic and electric domains, *Nature* **419**(6909), 818–820 (2002).

[25] Goto, T., Kimura, T., Lawes, G., Ramirez, A. P. and Tokura, Y. Ferroelectricity and Giant Magnetocapacitance in Perovskite Rare-Earth Manganites, *Phys. Rev. Lett.* **92**(25), 257201 (2004).

[26] Munoz, A., Casais, M. T., Alonso, J. A., Martinez-Lope, M. J., Martinez, J. L. and Fernandez-Diaz, M. T. Complex Magnetism and Magnetic Structures of the Metastable HoMnO3 Perovskite, *Inorg. Chem.* **40**(5), 1020–1028 (2001).

[27] Nan, C.-W., Bichurin, M. I., Dong, S., Viehland, D. and Srinivasan, G. Multiferroic magnetoelectric composites: Historical perspective, status, and future directions, *J. Appl. Phys.* **103**(3), 031101 (2008).

[28] West, A. R. *Solid State Chemistry and Its Applications.* Wiley, Singapore, (1984).

[29] Young, R. *The Rietveld Method.* Oxford University Press, Clarendon, (1995).

[30] Goldstein, J. I. and Yakowitz, H. *Practical Scanning Electron Microscopy.* Plenum Press, New York, (1975).

[31] Agilent Technologies, Inc., USA. *Agilent Basics of Measuring the Dielectric Properties of Materials*, (2006).

[32] Radiant Technologies, Albuquerque, NM 87106. *Radiant Technologies vision software manual version 3.1.0*, (2002).

[33] Quantum Design, San Diego, CA 92121, USA. *Quantum Design. User manual of the physical property measurement system.*, 2 edition, (1999).

[34] Stewart, G. R. Measurement of low-temperature specific heat, *Rev. Sci. Instrum.* **54**(1), 1–11 (1983).

[35] Hwang, J. S., Lin, K. J. and Tien, C. Measurement of heat capacity by fitting the whole temperature response of a heat-pulse calorimeter, *Rev. Sci. Instrum.* **68**(1), 94–101 (1997).

[36] Cross, E. Lead-free at last, *Nature* **432**(7013), 24–25 (2004).

[37] Jarosińska, D., Biesiada, M. and Graca, M. M. Environmental burden of disease due to lead in urban children from Silesia, Poland, *Science of The Total Environment* **367**(1), 71–79 (2006).

[38] Saito, Y., Takao, H., Tani, T., Nonoyama, T., Takatori, K., Homma, T., Nagaya, T. and Nakamura, M. Lead-free piezoceramics, *Nature* **432**(7013), 84–87 (2004).

[39] Neurgaonkar, R. R., Hall, W. F., Oliver, J. R., Ho, W. W. and Cory, W. K. Tungsten bronze $Sr_{1-x}Ba_xNb_2O_6$: A case history of versatility, *Ferroelectrics* **87**(1), 167–179 (1988).

[40] Neurgaonkar, R. R., Oliver, J. R., Cory, W. K., Cross, L. E. and Viehland, D. Piezoelectricity in tungsten bronze crystals, *Ferroelectrics* **160**(1), 265–276 (1994).

[41] Xie, R. J. and Akimune, Y. Lead-free piezoelectric ceramics in the (1 - x)$Sr_2NaNb_5O_{15x}Ca_2NaNb_5O_{15}$ ($0.05 \leq x \leq 0.35$) system, *J. Mater. Chem.* **12**, 3156–3161 (2002).

[42] Eerenstein, W., Morrison, F. D., Sher, F., Prieto, J. L., Attfield, J. P., Scott, J. F. and Mathur, N. D. Experimental difficulties and artefacts in multiferroic and magnetoelectric thin films of $BiFeO_3$, $Bi_{0.6}Tb_{0.3}La_{0.1}FeO_3$ and $BiMnO_3$, *Philos. Mag. Lett.* **87**(3-4), 249257 (2007).

[43] Baettig, P., Schelle, C. F., LeSar, R., Waghmare, U. V. and Spaldin, N. A. Theoretical prediction of new high-performance lead-free piezoelectrics, *Chem. Mater.* **17**(6), 1376–1380 (2005).

[44] Carvajal, J. R. Recent advances in magnetic structure determination by neutron powder diffraction, *Physica B* **192**(1-2), 55–69 (1993).

[45] Mangalam, R. V. K., Ranjith, R., Iyo, A., Sundaresan, A., Krupanidhi, S. B. and Rao, C. N. R. Ferroelectricity in $Bi_{26-x}M_xO_{40-\delta}$ (M=Al and Ga) with the γ - Bi_2O_3 structure, *Solid State Commun.* **140**(1), 42–44 (2006).

[46] Harwig, H. A. On the Structure of Bismuthsesquioxide: The α, β, γ, and δ-phase, *Z. Anorg. Allg. Chem.* **444**, 51 (1978).

[47] Belik, A. A., Wuernisha, T., Kamiyama, T., Mori, K., Male, M., Nagai, T., Matsui, Y. and Takayama-Muromachi, E. High-pressure synthesis, crystal structures, and properties of perovskite-like $BiAlO_3$ and pyroxene-like $BiGaO_3$, *Chem. Mater.* **18**(1), 133–139 (2006).

[48] Rao, C. N. R. and Gopalakrishnan, J. *New Directions in Solid State Chemistry: Structure, Synthesis, Properties, Reactivity and Meterials Design.* Cambridge University Press, Cambridge, (1997).

[49] Fukumura, H., Harima, H., Kisoda, K., Tamada, M., Noguchi, Y. and Miyayama, M. Raman scattering study of multiferroic $BiFeO_3$ single crystal, *J. Magn. Magn. Mater.* **310**, e367–e369 (2007).

[50] Wessels, B. W. Metal-organic chemical vapor deposition of ferroelectric oxide thin films for electronic and optical applications, *Annu. Rev. Mater. Sci.* **25**(1), 525–546 (1995).

[51] Granzow, T., Balke, N., Lupascu, D. C. and Rodel, J. Evolution of a stable polarization state in lead zirconate titanate ceramics by repeated partial switching, *Appl. Phys. Lett.* **87**(21), 212901 (2005).

[52] Prellier, W., Singh, M. P. and Murugavel, P. The single-phase multiferroic oxides: From bulk to thin film, *J. Phys.: Condens. Matter* **17**(30) (2005).

[53] Eerenstein, W., Mathur, N. D. and Scott, J. F. Multiferroic and magnetoelectric materials, *Nature* **442**(7104), 759–765 (2006).

[54] Ramesh, R. and Spaldin, N. A. Multiferroics: Progress and prospects in thin films, *Nat. Mater.* **6**(1), 21–29 (2007).

[55] Rao, C. N. R. and Serrao, C. R. New routes to multiferroics, *J. Mater. Chem.* **17**(47), 4931–4938 (2007).

[56] Ramesha, K., Llobet, A., Profen, T., Serrao, C. R. and Rao, C. N. R. Observation of local non-centrosymmetry in weakly biferroic $YCrO_3$, *J. Phys.: Condens. Matter* **19**, 102202 (2007).

[57] Santos, A. M. d., Parashar, S., Raju, A. R., Zhao, Y. S., Cheetham, A. K. and Rao, C. N. R. Evidence for the likely occurrence of magnetoferroelectricity in the simple perovskite, $BiMnO_3$, *Solid State Commun.* **122**(1-2), 49–52 (2002).

[58] Santos, A. M. d., Cheetham, A. K., Atou, T., Syono, Y., Yamaguchi, Y., Ohoyama, K., Chiba, H. and Rao, C. N. R. Orbital ordering as the determinant for ferromagnetism in biferroic $BiMnO_3$, *Phys. Rev. B* **66**(6), 644251–644254 (2002).

[59] Kimura, T., Kawamoto, S., Yamada, I., Azuma, M., Takano, M. and Tokura, Y. Magnetocapacitance effect in multiferroic $BiMnO_3$, *Phys. Rev. B* **67**(18), 1804011–1804014 (2003).

[60] Sugawara, F., Iiida, S., Syono, Y. and Akimoto, S. New Magnetic Perovskites $BiMnO_3$ and $BiCrO_3$, *J. Phys. Soc. Japan.* **20**, 1529–1529 (1965).

[61] Rao, C., Cheetham, A. and Mahesh, R. Giant Magnetoresistance and Related Properties of Rare-Earth Manganates and Other Oxide Systems, *Chem. Mater.* **8**(10), 2421–2432 (1996).

[62] Sugawara, F., Iiida, S., Syono, Y. and Akimoto, S. Magnetic Properties and Crystal Distortions of $BiMnO_3$ and $BiCrO_3$, *J. Phys. Soc. Japan.* **25**(6), 1553–1558 (1968).

[63] Atou, T., Chiba, H., Ohoyama, K., Yamaguchi, Y. and Syono, Y. Structure determination of ferromagnetic perovskite $BiMnO_3$, *J. Solid State Chem.* **145**(2), 639–642 (1999).

[64] Chiba, H., Atou, T., Faqir, H., Kikuchi, M., Syono, Y., Murakami, Y. and Shindo, D. Synthesis and characterization of (Bi, AE)MnO_3 (AE = Ca, Sr) system, *Solid State Ionics* **108**(1-4), 193–199 (1998).

[65] Hill, N. A. and Rabe, K. M. First-principles investigation of ferromagnetism and ferroelectricity in bismuth manganite, *Phys. Rev. B* **59**(13), 8759–8769 (1999).

[66] Santos, A. M. d., Cheetham, A. K., Tian, W., Pan, X., Jia, Y., Murphy, N. J., Lettieri, J. and Schlom, D. G. Epitaxial growth and properties of metastable $BiMnO_3$ thin films, *Appl. Phys. Lett.* **84**(1), 91–93 (2004).

[67] Ohshima, E., Saya, Y., Nantoh, M. and Kawai, M. Synthesis and magnetic property of the perovskite $Bi_{1-x}Sr_xMnO_3$ thin film, *Solid State Commun.* **116**(2), 73–76 (2000).

[68] Chi, Z. H., Yang, H., Feng, S. M., Li, F. Y., Yu, R. C. and Jin, C. Q. Room-temperature ferroelectric polarization in multiferroic $BiMnO_3$, *J. Magn. Magn. Mater.* **310**(2, Suppl. Part 2), e358–e360 (2007).

[69] Montanari, E., Righi, L., Calestani, G., Migliori, A., Gilioli, E. and Bolzoni, F. Room temperature polymorphism in metastable $BiMnO_3$ prepared by high-pressure synthesis, *Chem. Mater.* **17**(7), 1765–1773 (2005).

[70] Montanari, E., Calestani, G., Migliori, A., Dapiaggi, M., Bolzoni, F., Cabassi, R. and Gilioli, E. High-temperature polymorphism in metastable $BiMnO_3$, *Chem. Mater.* **17**(25), 6457–6467 (2005).

[71] Belik, A. A., Iikubo, S., Yokosawa, T., Kodama, K., Igawa, N., Shamoto, S., Azuma, M., Takano, M., Kimoto, K., Matsui, Y. and Takayama-Muromachi, E. Origin of the monoclinic-to-monoclinic phase transition and evidence for the centrosymmetric crystal structure of $BiMnO_3$, *JACS* **129**(4), 971–977 (2007).

[72] Baettig, P., Seshadri, R. and Spaldin, N. A. Anti-polarity in ideal $BiMnO_3$, *JACS* **129**(32), 9854–9855 (2007).

[73] Kodama, K., Iikubo, S., Shamoto, S., Belik, A. A. and Takayama-Muromachi, E. Local Crystal Structure of Multiferroic System $BiMnO_3$ by Atomic Pair Distribution Function Analysis, *J. Phys. Soc. Jpn.* **76**, 124605 (2007).

[74] Yokosawa, T., Belik, A. A., Asaka, T., Kimoto, K., Muromachi, E. T. and Matsui, Y. Crystal symmetry of $BiMnO_3$: Electron diffraction study, *Phys. Rev. B* **77**(2), 024111 (2008).

[75] Belik, A. A., Yokosawa, T., Kimoto, K., Matsui, Y. and Takayama-Muromachi, E. High-pressure synthesis and properties of solid solutions between $BiMnO_3$ and $BiScO_3$, *Chem. Mater.* **19**(7), 1679–1689 (2007).

[76] Skumryev, V., Ott, F., Coey, J. M. D., Anane, A., Renard, J. ., Pinsard-Gaudart, L. and Revcolevschi, A. Weak ferromagnetism in $LaMnO_3$, *Eur. Phys. J. B* **11**(3), 401–406 (1999).

[77] Scott, J. F. Data storage: Multiferroic memories, *Nat. Mater.* **6**(4), 256–257 (2007).

[78] Spaldin, N. A. and Fiebig, M. The renaissance of magnetoelectric multiferroics, *Science* **309**(5733), 391–392 (2005).

[79] Ederer, C. and Spaldin, N. A. A new route to magnetic ferroelectrics, *Nat. Mater.* **3**(12), 849–851 (2004).

[80] Serrao, C. R., Sundaresan, A. and Rao, C. N. R. Multiferroic nature of charge-ordered rare earth manganites, *J. Phys.: Condens. Matter* **19**(49) (2007).

[81] Mostovoy, M. Ferroelectricity in spiral magnets, *Phys. Rev. Lett.* **96**(6) (2006).

[82] Böttcher, R., Klimm, C., Michel, D., Semmelhack, H. C., Völkel, G., Gläsel, H. J. and Hartmann, E. Size effect in Mn^{2+}-doped $BaTiO_3$ nanopowders

observed by electron paramagnetic resonance, *Phys. Rev. B* **62**(3), 2085–2095 (2000).

[83] Zhong, W. L., Wang, Y. G., Zhang, P. L. and Qu, B. D. Phenomenological study of the size effect on phase transitions in ferroelectric particles, *Phys. Rev. B* **50**(2), 698–703 (1994).

[84] Sundaresan, A., Bhargavi, R., Rangarajan, N., Siddesh, U. and Rao, C. N. R. Ferromagnetism as a universal feature of nanoparticles of the otherwise nonmagnetic oxides, *Phys. Rev. B* **74**(16) (2006).

[85] Nuraje, N., Su, K., Haboosheh, A., Samson, J., Manning, E. P., Yang, N. I. and Matsui, H. Room temperature synthesis of ferroelectric barium titanate nanoparticles using peptide nanorings as templates, *Adv. Mater.* **18**(6), 807–811 (2006).

[86] Cho, W. S. Structural evolution and characterization of $BaTiO_3$ nanoparticles synthesized from polymeric precursor, *J. Phys. Chem. Solids* **59**(5), 659–666 (1998).

[87] Jana, A., Kundu, T. K., Pradhan, S. K. and Chakravorty, D. Dielectric behavior of Fe-ion-doped $BaTiO_3$ nanoparticles, *J. Appl. Phys.* **97**(4), 044311 (2005).

[88] Hautojarvi, P. and Corbel, C. Positron spectroscopy of defects in metals and semiconductors. in *Positron Spectroscopy of Solids,* (Dupasquier, A. and Mills Jr, A., eds), 491. IOS Press, Ohmsha, Amsterdam (1995).

[89] Rehberg, R. K. and Leipner, H. S. *Positron Annihilation in Semiconductors.* Springer, Verlag, Berlin, (1999).

[90] Sanyal, D., Banerjee, D. and De, U. Probing $(Bi_{0.92}Pb_{0.17})_2Sr_{1.91}Ca_{2.03}Cu_{3.06}O_{10+\delta}$ superconductors from 30 to 300 K by positron-lifetime measurements, *Phys.Rev.B* **58**(22), 15226 (1998).

[91] Kirkegaard, P., Pedersen, N. and Eldroup, M. Technical report, (1989).

[92] Lynn, K. and Goland, A. Observation of high momentum tails of positron-annihilation lineshapes, *Solid State Commun.* **18**(11-12), 1549–1552 (1976).

[93] Sanyal, D., Chakrabarti, M., Roy, T. K. and Chakrabarti, A. The origin of ferromagnetism and defect-magnetization correlation in nanocrystalline ZnO, *Phys.Lett.A* **371**(5-6), 482–485 (2007).

[94] Chakrabarti, M., Sarkar, A., Sanyal, D., Karwasz, G. and Zecca, A. Studies of coincidence Doppler broadening of the electron-positron annihilation radiation in the single crystalline $Bi_2Sr_2CaCu_2O_{8+\delta}$ superconductor, *Phys.Lett.A* **321**(5-6), 376–380 (2004).

[95] Dutta, S., Chakrabarti, M.and Chattopadhyay, S. J. D. and Sanyal, D.and Sarkar, A. Defect dynamics in annealed ZnO by positron annihilation spectroscopy, *J.Appl.Phys.* **98**(5), 053513–053515 (2005).

[96] Dutta, S., Chattopadhyay, S., Sarkar, A., Chakrabarti, M., Sanyal, D. and Jana, D. Role of defects in tailoring structural, electrical and optical properties of ZnO, *Prog.Mater Sci.* **In Press** (2008).

[97] Smith, M. B., Page, K., Siegrist, T., Redmond, P. L., Walter, E. C., Seshadri, R., Brus, L. E. and Steigerwald, M. L. Crystal structure and the paraelectric-to-ferroelectric phase transition of nanoscale $BaTiO_3$, *J. Am. Chem. Soc.* **130**(22), 6955–6963 (2008).

[98] Stoneham, A. *Theory of defects in solids.* Oxford, Clarendon, (1975).

[99] Stoneham, A. M., Gavartin, J., Shluger, A. L., Kimmel, A. V., Muoz Ramo, D., Rønnow, H. M., Aeppli, G. and Renner, C. Trapping, self-trapping and the polaron family, *J. Phys.: Condens. Matter* **19**, 255208 (2007).

[100] Guillén, J. O., Lany, S., Barabash, S. V. and Zunger, A. Nonstoichiometry as a source of magnetism in otherwise nonmagnetic oxides: Magnetically interacting cation vacancies and their percolation, *Phys. Rev. B* **75**(18) (2007).

[101] Ahmad, G., Dickerson, M. B., Cai, Y., Jones, S. E., Ernst, E. M., Vernon, J. P., Haluska, M. S., Fang, Y., Wang, J., Subramanyam, G., Naik, R. R. and Sandhage, K. H. Rapid bioenabled formation of ferroelectric $BaTiO_3$ at room temperature from an aqueous salt solution at near neutral pH, *J. Am. Chem. Soc.* **130**(1), 4–5 (2008).

[102] Baroni, S., Gironcoli, S., Corso, A. and Giannozzi, P. PWSCF (plane-wave self-consistent field) codes.

[103] Perdew, J. P. and Zunger, A. Self-interaction correction to density-functional approximations for many-electron systems, *Phys. Rev. B* **23**(10), 5048–5079 (1981).

[104] Vanderbilt, D. Soft self-consistent pseudopotentials in a generalized eigenvalue formalism, *Phys. Rev. B* **41**(11), 7892–7895 (1990).

[105] Monkhorst, H. J. and Pack, J. D. Special points for Brillouin-zone integrations, *Phys. Rev. B* **13**(12), 5188–5192 (1976).

[106] Ghosez, P., Gonze, X., Lambin, P. and Michenaud, J. P. Born effective charges of barium titanate: Band-by-band decomposition and sensitivity to structural features, *Phys. Rev. B* **51**(10), 6765–6768 (1995).

[107] Ghosh, V. J., Nielsen, B. and Friessnegg, T. Identifying open-volume defects in doped and undoped perovskite-type $LaCoO_3$, $PbTiO_3$, and $BaTiO_3$, *Phys. Rev. B* **61**(1), 207–212 (2000).

[108] Sanyal, D.and Roy, T. K., Chakrabarti, M., Dechoudhury, S., Bhowmick, D. and Chakrabarti, A. Defect studies in annealed ZnO by positron annihilation spectroscopy, *J.Phys.: Condens.Matter* **20**(4), 045217 (2008).

[109] Sundaresan, A. and Rao, C. N. R. Ferromagnetism as a universal feature of inorganic nanoparticles, *Nano Today* **4**(1), 96 (2009).

[110] Mangalam, R. V. K., Ray, N., Waghmare, U. V., Sundaresan, A. and Rao, C. N. R. Multiferroic Properties of Nanocrystalline $BaTiO_3$, *Solid State Commun.* **149**(1), 1–5 (2009).

[111] Raveau, B. The perovskite history: More than 60 years of research from the discovery of ferroelectricity to colossal magnetoresistance via high T_C superconductivity, *Prog. Solid State Chem.* **35**(2-4 SPEC. ISS.), 171–173 (2007).

[112] Cava, R. J., Batlogg, B., Krajewski, J. J., Farrow, R., Rupp, L. W., White, A. E., Short, K., Peck, W. F. and Kometani, T. Superconductivity near 30 K without copper: The $Ba_{0.6}K_{0.4}BiO_3$ perovskite, *Nature* **332**(6167), 814–816 (1988).

[113] Hinks, D. G., Dabrowski, B., Jorgensen, J. D., Mitchell, A. W., Richards, D. R., Pei, S. and Shi, D. Synthesis, structure and superconductivity in the $Ba_{1-x}K_xBiO_{3-y}$ system, *Nature* **333**(6176), 836–838 (1988).

[114] Mattheiss, L. F., Gyorgy, E. M. and Johnson Jr., D. W. Superconductivity above 20 K in the Ba-K-Bi-O system, *Phys. Rev. B* **37**(7), 3745–3746 (1988).

[115] Sleight, A. W., Gillson, J. L. and Bierstedt, P. E. High-temperature superconductivity in the $BaPb_{1-x}Bi_xO_3$ system., *Solid State Commun.* **17**(1), 27–28 (1975).

[116] Cox, D. E. and Sleight, A. W. Mixed-valent $Ba_2Bi^{3+}Bi^{5+}O_6$: structure and properties vs temperature, *Acta Crystallogr. B* **35**, 1–10 (1979).

[117] Hashimoto, T. Determination of the crystal system and space group of $BaBiO_3$ by convergent-beam electron diffraction and x-ray diffraction using synchrotron radiation, *Phys. Rev. B* **64**(22), 224114 (2001).

[118] Watson, G. W. and Parker, S. C. Origin of the Lone Pair of α-PbO from Density Functional Theory Calculations, *J. Phys. Chem. B* **103**, 1258–1262 (1999).

[119] Payne, D. J., Egdell, R. G., Walsh, A., Watson, G. W., Guo, J., Glans, P. A., Learmonth, T. and Smith, K. E. Electronic origins of structural distortions in post-transition metal oxides: experimental and theoretical evidence for a revision of the lone pair model, *Phys. Rev. Lett.* **96**, 157403 (2006).

[120] Mangalam, R. V. K., Bhat, S. V., Iyo, A., Tanaka, Y., Sundaresan, A. and Rao, C. N. R. Dielectric properties, thermal decomposition and related aspects of $BiAlO_3$, *Solid State Commun.* **18**(19), 2191–2193 (2008).

[121] Shannon, R. D. Revised effective ionic radii and systematic studies of interatomic distances in halides and chalcogenides, *Acta Crystallogr.* **32**, 751–767 (1976).

[122] Fu, W. T. Neutron powder diffraction study on $BaBi_{0.5}Sb_{0.5}O_3$, *Solid State Commun.* **116**(8), 461–464 (2000).

[123] Kennedy, B. J., Howard, C. J., Knight, K. S., Zhang, Z. and Zhou, Q. Structures and phase transitions in the ordered double perovskites $Ba_2Bi^{III}Bi^{v}O_6$ and $Ba_2Bi^{III}Sb^{v}O_6$, *Acta Crystallogr. B* **62**(4), 537–546 (2006).

[124] Larson, A. C. and Von Dreele, R. B. *General structure analysis system (GSAS)*, (2000).

[125] Toby, B. H. EXPGUI, a graphical user interface for GSAS, *J. Appl. Crystallogr.* **34**(2), 210–213 (2001).

[126] Lufaso, M. W., MacQuart, R. B., Lee, Y., Vogt, T. and Zur Loye, H. C. Pressure-induced phase transition and octahedral tilt system change of Ba_2BiSbO_6, *J. Solid State Chem.* **179**(3), 917–922 (2006).

[127] Mangalam, R. V. K., Suard, E. and Sundaresan, A. Crystal structure and dielectric properties of ordered perovskites Ba_2BiSbO_6 and $BaSrBiSbO_6$, *Physica B* **404**, 154157 (2009).

[128] Haemers, T. A. M. and Ijdo, D. J. W. Structure determination of $SrBi_2O_4$, *Mater. Res. Bull.* **26**(10), 989–993 (1991).

[129] Davies, P. K., Wu, H., Borisevich, A. Y., Molodetsky, I. E. and Farber, L. Crystal chemistry of complex perovskites: New cation-ordered dielectric oxides, *Annu. Rev. Mater. Sci.* **38**, 369–401 (2008).

[130] Carvajal, J. R. FULLPROF: A Program for Rietveld Refinement and Pattern Matching Analysis. in *Abstracts of the Satellite Meeting on Powder Diffraction of the XV Congress of the IUCr*, 127 (, Toulouse, France, 1990).

[131] Mao, H. and Bell, P. *Year Book-Carnegie Institution of Washington*. Number 77. Washington D.C.:Carnegie Institution of Washington, (1978).

[132] Mao, H., Xu, J. and Bell, P. Calibration of the Ruby Pressure Gauge to 800 kbar Under Quasi-Hydrostatic Conditions, *J.Geophys.Res. [Solid Earth Planets]* **91**(B5), 4673–4676 (1986).

[133] Desgreniers, S. and Lagarec, K. XRDA: a program for energy-dispersive X-ray diffraction analysis on a PC, *J.Appl.Crystallogr.* **27**, 432–434 (1994).

[134] Desgreniers, S. and Lagarec, K. XRDA3.1 - a program for X-ray diffraction analysis on a PC, *J.Appl.Crystallogr.* **31**, 109–110 (1998).

[135] Scott, J. F. Ferroelectrics go bananas, *J. Phys.: Condens. Matter* **20**, 021001 (2008).

[136] Lines, M. E. and Glass, A. M. *Principles and Applications of Ferroelectrics and Related Materials*. Oxford, Clarendon, (1977).

[137] Dawber, M., Rabe, K. M. and Scott, J. F. Physics of thin-film ferroelectric oxides, *Rev.Mod.Phys.* **77**(4), 1083 (2005).

[138] Mangalam, R. V. K., Mandal, P., Suard, E. and Sundaresan, A. Ferroelectricity in ordered perovskite $BaBi^{3+}_{0.5}(Bi^{5+}_{0.2}Nb^{5+}_{0.3})O_3$ with Bi^{3+}:$6s^2$ lone pair at the B-site, *Chem. Mater.* **19**(17), 4114–4116 (2007).

[139] von Helmolt, R., Wecker, J., Holzapfel, B., Schultz, L. and Samwer, K. Giant negative magnetoresistance in perovskitelike $La_{2/3}Ba_{1/3}MnO_x$ ferromagnetic films, *Phys. Rev. Lett.* **71**(14), 2331–2333 (1993).

[140] Jin, S., McCormack, M., Tiefel, T. H. and Ramesh, R. Colossal magnetoresistance in La-Ca-Mn-O ferromagnetic thin films (invited), *J. Appl. Phys.: The 6th joint magnetism and magnetic materials (MMM)-intermag conference* **76**(10), 6929–6933 (1994).

[141] Jonker, G. H. and van Santen, J. H., t. . F. j. . P. v. . . n. . . p. . . y. . . .

[142] Zener, C. Interaction between the d-shells in the transition metals. II. Ferromagnetic compounds of manganese with Perovskite structure, *Phys. Rev.* **82**(3), 403–405 (1951).

[143] Anderson, P. W. and Hasegawa, H. Considerations on double exchange, *Phys. Rev.* **100**(2), 675–681 (1955).

[144] Gennes, P. G. d. Effects of Double Exchange in Magnetic Crystals, *Phys. Rev.* **118**, 141–154 (1960).

[145] Papavassiliou, G., Fardis, M., Belesi, M., Maris, T. G., Kallias, G., Pissas, M., Niarchos, D., Dimitropoulos, C. and Dolinsek, J. ^{55}Mn NMR Investigation of Electronic Phase Separation in $La_{1-x}Ca_xMnO_3$ for $0.2 \leq x \leq 0.5$, *Phys. Rev. Lett.* **84**(4), 761–764 (2000).

[146] Asamitsu, A., Moritomo, Y., Tomioka, Y., Arima, T. and Tokura, Y. A structural phase transition induced by an external magnetic field, *Nature* **373**(6513), 407–409 (1995).

[147] Ramirez, A. P. Colossal magnetoresistance, *J. Phys.: Condens. Matter* **9**(39), 8171–8199 (1997).

[148] Sundaresan, A., Caignaert, V., Maignan, A., Raveau, B. and Suard, E. Anomalous magnetic ordering of Ce and Kondo-like effect in the double-exchange ferromagnet $(Pr_{0.1}Ce_{0.4}Sr_{0.5})MnO_3$, *Phys. Rev. B* **60**(1), 533–537 (1999).

[149] Sundaresan, A., Tholence, J. L., Maignan, A., Raveau, B., Suard, E. and Bordet, P. Kondo-like effect in the double exchange ferromagnet $La_{0.5-x}Ce_xSr_{0.5}MnO_3$, *J. Magn. Magn. Mater.* **226-230**, 777 (2001).

[150] Zeng, Z., Greenblatt, M. and Croft, M. Charge ordering and magnetoresistance of $Ca_{1-x}Ce_xMnO_3$, *Phys. Rev. B* **63**(22), 2244101–22441010 (2001).

[151] Radaelli, P. G., Marezio, M., Hwang, H. Y. and Cheong, S. W. Structural phase diagram of Perovskite $A_{0.7}Á_{0.3}MnO_3$ (A = La, Pr; Á = Ca, Sr, Ba): A new Imma allotype, *J. Solid State Chem.* **122**(2), 444–447 (1996).

[152] Barnabe, A., Millange, F., Maignan, A., Hervieu, M., Raveau, B., Van Tendeloo, G. and Laffez, P. Barium-Based Manganites $Ln_{1-x}Ba_xMnO_3$ with Ln = Pr, La: Phase Transitions and Magnetoresistance Properties, *Chem. Mater.* **10**(1), 252–259 (1998).

[153] Martinez, L. M. R. and Attfield, J. P. Cation disorder and size effects in magnetoresistive manganese oxide perovskites, *Phys. Rev. B* **54**, R15622 (1996).

[154] Jonker, G. H. and van Santen, J. H. Magnetic compounds wtth perovskite structure III. ferromagnetic compounds of cobalt, *Physica (Amsterdam)* **19**, 120 (1953).

[155] Rao, C. N. R., Parkash, O., Bahadur, D., Ganguly, P. and Nagabhushana, S. Itinerant electron ferromagnetism in Sr^{2+}-, Ca^{2+}-, and Ba^{2+} -doped rare-earth orthocobaltites (Ln^{3+}_{1-x})$M^{2+}_x CoO_3$), *J. Solid State Chem.* **22**(3), 353–360 (1977).

[156] Mahendiran, R., Raychaudhuri, A. K., Chainani, A. and Sarma, D. D. The large magnetoresistance of $La_{1-x}Sr_xCoO_3$ at low temperatures, *J. Phys.: Condens. Matter* **7**(43) (1995).

[157] Bhide, V. G., Rajoria, D. S., Rao, G. R. and Rao, C. N. R. Mossbauer studies of the high-spin-low-spin equilibria and the localized-collective electron transition in $LaCoO_3$, *Phys. Rev. B* **6**(3), 1021–1032 (1972).

[158] Yamaguchi, S., Okimoto, Y., Taniguchi, H. and Tokura, Y. Spin-state transition and high-spin polarons in $LaCoO_3$, *Phys. Rev. B* **53**(6) (1996).

[159] Bezdicka, P., Wattiaux, A., Grenier, J. C., Pouchard, M. and Hagenmuller, P. Preparation and characterization of Fully stoichiometric $SrCoO_3$ by electrochemical oxidation, *Z. Anorg. Allg. Chem.* **619**(1), 7–12 (1993).

[160] Potze, R. H., Sawatzky, G. A. and Abbate, M. Possibility for an intermediate-spin ground state in the charge-transfer material $SrCoO_3$, *Phys. Rev. B* **51**(17), 11501–11506 (1995).

[161] Zhuang, M., Zhang, W., Hu, A. and Ming, N. Possible magnetic ground state in the perovskite $SrCoO_3$, *Phys. Rev. B* **57**(21), 13655–13659 (1998).

[162] Takeda, T., Yamaguchi, Y. and Watanabe, H. Magnetic structure of $SrCoO_{2.5}$., *J. Phys. Soc. Jpn.* **33**(4), 970–972 (1972).

[163] Watanabe, H. Magnetic properties of perovskites containing strontium I. strontium-rich ferrites and cobaltites, *J. Phys. Soc. Jpn.* **12**, 515–522 (1957).

[164] Taguchi, H., Shimada, M., Kanamaru, F., Koizumi, M. and Takeda, Y. Magnetic properties in the system $BaCo_{1-x}Mn_xO_3$ AND $SrCo_{1-x}Mn_xO_3$ ($0 \leq x \leq 1$)., *J. Solid State Chem.* **18**(3), 299–302 (1976).

[165] Istomin, S. Y., Drozhzhin, O. A., Svensson, G. and Antipov, E. V. Synthesis and characterization of $Sr_{1-x}Ln_xCoO_{3-\delta}$, (Ln = Y, Sm-Tm), $0.1 \leq x \leq 0.5$, *Solid State Sci.* **6**(6), 539–546 (2004).

[166] James, M., Cassidy, D., Goossens, D. J. and Withers, R. L. The phase diagram and tetragonal superstructures of the rare earth cobaltate phases $Ln_{1-x}Sr_xCoO_{3-\delta}$ (Ln = La^{3+}, Pr^{3+}, Nd^{3+}, Sm^{3+}, Gd^{3+}, Y^{3+}, Ho^{3+}, Dy^{3+}, Er^{3+}, Tm^{3+} and Yb^{3+}), *J. Solid State Chem.* **177**(6), 1886–1895 (2004).

[167] Maignan, A., Hébert, S., Caignaert, V., Pralong, V. and Pelloquin, D. $Sr_{2/3}Y_{1/3}CoO_{8/3+\delta}$: Transition from insulating antiferromagnet to metallic ferromagnet by control of the oxygen content, *J. Solid State Chem.* **178**(3), 868–873 (2005).

[168] Withers, R. L., James, M. and Goossens, D. J. Atomic ordering in the doped rare earth cobaltates $Ln_{0.33}Sr_{0.67}CoO_{3-\delta}$ (Ln = Y_{3+}, Ho_{3+} and Dy_{3+}), *J. Solid State Chem.* **174**(1), 198–208 (2003).

[169] Raveau, B., Pralong, V., Caignaert, V., Hervieu, M. and Maignan, A. Primordial role of cobalt valence in the magnetotransport properties of oxygen deficient perovskites $Sr_{1-x}Ln_xCoO_{3-\delta}$, *J. Phys.: Condens. Matter* **17**(46), 7371–7382 (2005).

[170] Nguyen, H. C. and Goodenough, J. B. Magnetic and transport properties of $CeVO_3$, *J. Solid State Chem.* **119**, 24–35 (1995).

[171] Onoda, M. and Yasumoto, M. Electronic states of perovskite-type $Ce_{1-x}Sr_xTiO_3$ and $CeTiO_{3+y/2}$ systems with a metal-insulator transition, *J. Phys.: Condens. Matter* **9**(26), 5623–5634 (1997).

[172] Christian, G. D. *Analytical Chemistry.* (1994).

[173] Maignan, A., Raveau, B., Hébert, S., Pralong, V., Caignaert, V. and Pelloquin, D. Re-entrant metallicity and magnetoresistance induced by Ce for Sr substitution in $SrCoO_{3-\delta}$, *J. Phys.: Condens. Matter* **18**(17), 4305–4314 (2006).

[174] Paraskevopoulos, M., Hemberger, J., Krimmel, A. and Loidl, A. Magnetic ordering and spin-state transition in $R_{0.67}Sr_{0.33}CoO_3$, *Phys. Rev. B* **63**(22), 224416 (2001).

[175] Hébert, S., Maignan, A., Caignaert, V., Pralong, V., Pelloquin, D. and Raveau, B. Ferromagnetism and metallicity in the modulated $Sr_{1-x}Th_xCoO_{3-\delta}$ oxygen deficient perovskites with x$\sim$0.1, *Solid State Commun.* **134**(12), 815–820 (2005).

[176] Tajima, S., Masaki, A., Uchida, S., Matsuura, T., Fueki, K. and Sugai, S. Infrared reflectivioty and electronic states in perovskite-type oxides $La_{1-x}Sr_xFeO_3$ AND $La_{1-x}Sr_xCoO_3$., *J. Phys. C: Solid State Phys.* **20**(23), 3469–3484 (1987).

[177] Sudheendra, L., Motin Seikh, M., Raju, A. R. and Narayana, C. An infrared spectroscopic study of the low-spin to intermediate-spin state ($^1A_1$-$^3T_1$) transition in rare earth cobaltates, $LnCoO_3$ (Ln=La, Pr and Nd), *Chem. Phys. Lett.* **340**(3-4), 275–281 (2001).

[178] Iliev, M. N., Litvinchuk, A. P., Lee, H., Chen, C. L., Dezaneti, M. L., Chu, C. W., Ivanov, V. G., Abrashev, M. V. and Popov, V. N. Raman spectroscopy of $SrRuO_3$ near the paramagnetic-to-ferromagnetic phase transition, *Phys. Rev. B* **59**(1), 364–368 (1999).

[179] Kim, K. H., Gu, J. Y., Choi, H. S., Park, G. W. and Noh, T. W. Frequency shifts of the internal phonon modes in $La_{0.7}Ca_{0.3}MnO_3$, *Phys. Rev. Lett.* **77**(9), 1877–1880 (1996).

[180] Tiwari, A. and Rajeev, K. P. Low-temperature electrical transport in $La_{0.7}A_{0.3}MnO_3$, (A: Ca, Sr, Ba), *Solid State Commun.* **111**(1), 33–37 (1999).

[181] Rana, D. S., Markna, J. H., Parmar, R. N., Kuberkar, D. G., Raychaudhuri, P., John, J. and Malik, S. K. Low-temperature transport anomaly in the magnetoresistive compound $(La_{0.5}Pr_{0.2})Ba_{0.3}MnO_3$, *Phys. Rev. B* **71**(21), 212404 (2005).

[182] Herranz, G., Martínez, B., Fontcuberta, J., Sánchez, F., Ferrater, C., García-Cuenca, M. V. and Varela, M. Enhanced electron-electron correlations in nanometric $SrRuO_3$ epitaxial films, *Phys. Rev. B* **67**(17), 1744231–1744238 (2003).

[183] Woodfield, B. F., Wilson, M. L. and Byers, J. M. Low-temperature specific heat of $La_{1-x}Sr_xMnO_{3+\delta}$, *Phys. Rev. Lett.* **78**(16), 3201–3204 (1997).

[184] Gordon, J. E., Fisher, R. A., Jia, Y. X., Phillips, N. E., Reklis, S. F., Wright, D. A. and Zettl, A. Specific heat of $Nd_{0.67}Sr_{0.33}MnO_3$, *Phys. Rev. B* **59**(1), 127–130 (1999).

[185] Longo, J. M., Raccah, P. M. and Goodenough, J. B. Magnetic properties of $SrRuO_3$ and $CaRuO_3$, *J. Appl. Phys.* **39**(2), 1327–1328 (1968).

[186] Maeno, Y., Hashimoto, H., Yoshida, K., Nishizaki, S., Fujita, T., Bednorzt, J. G. and Lichtenberg, F. Superconductivity in a layered perovskite without copper, *Nature* **372**(6506), 532–534 (1994).

[187] Bernhard, C., Tallon, J. L., Niedermayer, C., Blasius, T., Golnik, A., Brücher, E., Kremer, R. K., Noakes, D. R., Stronach, C. E. and Ansaldo, E. J. Coexistence of ferromagnetism and superconductivity in the hybrid ruthenate-cuprate compound $RuSr_2GdCu_2O_8$ studied by muon spin rotation and dc magnetization, *Phys. Rev. B* **59**(21), 14099–14107 (1999).

[188] Cao, G., McCall, S., Shepard, M., Crow, J. E. and Guertin, R. P. Thermal, magnetic, and transport properties of single-crystal $Sr_{1-x}Ca_xRuO_3$ ($0 \leq x \leq 1.0$), *Phys. Rev. B* **56**(1), 321–329 (1997).

[189] Pi, L., Maignan, A., Retoux, R. and Raveau, B. Substitution at the Ru site in the itinerant ferromagnet $SrRuO_3$, *J. Phys.: Condens. Matter* **14**(31), 7391–7398 (2002).

[190] Park, J. C., Kim, D., Lee, C. S. and Byeon, S. H. The variation of structure and transporting property in $SrRu_{1-x}Fe_xO_3$, *Bull. Korean Chem. Soc.* **24**(5), 650–652 (2003).

[191] Cao, G., Chikara, S., Lin, X. N., Elhami, E., Durairaj, V. and Schlottmann, P. Itinerant ferromagnetism to insulating antiferromagnetism: A magnetic and transport study of single crystal $SrRu_{1-x}Mn_xO_3$ ($0 \leq x \leq 0.60$), *Phys. Rev. B* **71**(3), 035104 (2005).

[192] Durairaj, V., Chikara, S., Lin, X. N., Douglass, A., Cao, G., Schlottmann, P., Choi, E. S. and Guertin, R. P. Highly anisotropic magnetism in Cr-doped perovskite ruthenates, *Phys. Rev. B* **73**(21), 214414 (2006).

[193] Wu, M. K., Chen, D. Y., Chien, F. Z., Sheen, S. R., Ling, D. C., Tai, C. Y., Tseng, G. Y., Chen, D. H. and Zhang, F. C. Anomalous magnetic and superconducting properties in a Ru-based double perovskite, *Z. Phys. B: Condens. Matter* **102**(1), 37–41 (1997).

[194] Felner, I., Nomura, K. and Nowik, I. Mössbauer and magnetic studies of bulk and fine-powder $SrRuO_3$ and Sr-Cu-Ru-O_3 systems, *Phys. Rev. B* **73**(6), 064401 (2006).

[195] Dabrowski, B., Chmaissem, O., Klamut, P. W., Kolesnik, S., Maxwell, M., Mais, J., Ito, Y., Armstrong, B. D., Jorgensen, J. D. and Short, S. Reduced ferromagnetic transition temperatures in $SrRu_{1-\nu}O_3$ perovskites from Ru-site vacancies, *Phys. Rev. B* **70**(1), 014423 (2004).

[196] Klamut, P. W., Dabrowski, B., Kolesnik, S., Maxwell, M. and Mais, J. Superconductivity in $Ru_{1-x}Sr_2GdCu_{2+x}O_{8-y}$ compounds, *Phys. Rev. B* **63**(22), 224512 (2001).

[197] Shikano, M., Huang, T. K., Inaguma, Y., Itoh, M. and Nakamura, T. Pressure dependence of the magnetic transition temperature for ferromagnetic $SrRuO_3$, *Solid State Commun.* **90**(2), 115–119 (1994).

[198] Kennedy, B. J. and Hunter, B. A. High-temperature phases of $SrRuO_3$, *Phys. Rev. B* **58**(2), 653–658 (1998).

[199] Bradarić, I. M., Felner, I. and Gospodinov, M. Metal-to-insulator transition and magnetic ordering in $CaRu_{1-x}Cu_xO_3$, *Phys. Rev. B* **65**(2), 024421 (2001).

[200] Moreo, A., Yunoki, S. and Dagotto, E. Phase separation scenario for manganese oxides and related materials, *Science* **283**(5410), 2034–2040 (1999).

[201] Dagotto, E., Hotta, T. and Moreo, A. Colossal magnetoresistant materials: The key role of phase separation, *Phys. Rep.* **344**(1-3), 1–153 (2001).

[202] Cardoso, C. A., Araujo-Moreira, F. M., Awana, V. P. S., Takayama-Muromachi, E., de Lima, O. F., Yamauchi, H. and Karppinen, M. Spin glass behavior in $RuSr_2Gd_{1.5}Ce_{0.5}Cu_2O_{10-\delta}$, *Phys. Rev. B* **67**(2), 020407 (2003).

[203] Mydosh, J. A. *Spin Glasses: An Experimental Introduction.* Taylor and Francis, London, (1993).

[204] Allen, P. B., Berger, H., Chauvet, O., Forro, L., Jarlborg, T., Junod, A., Revaz, B. and Santi, G. Transport properties, thermodynamic properties, and electronic structure of $SrRuO_3$, *Phys. Rev. B* **53**(8), 4393–4398 (1996).

[205] Yoshii, K. and Abe, H. Doping effects of Ru in $L_{0.5}Sr_{0.5}CoO_3$(L=La, Pr, Nd, Sm, and Eu), *Phys. Rev. B* **67**(9), 094408 (2003).

[206] Hammer, D., Wu, J. and Leighton, C. Metal-insulator transition, giant negative magnetoresistance, and ferromagnetism in $LaCo_{1-y}Ni_yO_3$, *Phys. Rev. B* **69**(13), 134407 (2004).

[207] Mamchik, A. and Chen, I.-W. Magnetic impurities in conducting oxides. I. $(Sr_{1-x}La_x)$ $(Ru_{1-x}Fe_x)O_3$ system, *Phys. Rev. B* **70**(10), 104409 (2004).